TECHNISCHE UNIVERSITÄT MÜNCHEN

Walter Schottky Institut
Zentralinstitut für Physikalische Grundlagen der Halbleiterelektronik
Fakultät für Physik

Spatially resolved spectroscopy on semiconductor nanostructures

Johanna Rössler

Vollständiger Abdruck der von der Fakultät für Physik der Technischen Universität München zur Erlangung des akademischen Grades eines

Doktors der Naturwissenschaften
genehmigten Dissertation.

Vorsitzender: Univ.-Prof. Dr. P. Vogl
Prüfer der Dissertation:
1. Univ.-Prof. Dr. G. Abstreiter
2. apl. Prof. Dr. M. S. Brandt
3. Prof. Dr. A. Fontcuberta i Morral,
   École Polytechnique Fédérale de Lausanne / Schweiz

Die Dissertation wurde am 13.01.2009 bei der Technischen Universität München eingereicht und durch die Fakultät für Physik am 20.02.2009 angenommen.

Contents

Chapter 1

Introduction

Semiconductor nanostructures are an active field of research, fueled by a growing electronic industry as well as promising future application areas like Quantum Information Technology. To that end, engineers and researchers strive towards ever smaller devices and increased control over quantum mechanical single particle states. While new systems and technologies are emerging constantly, two main approaches towards nanostructuring are in general distinguished. The first approach is called *top-down*. Here, a large scale material is the starting point. The nanostructuring typically is achieved by lithography and etching. While this technology offers a high level of control, the quality of the surfaces is limited because of the implantation of surface defects. With further downscaling, these defects eventually overcome the properties of the nanostructure. The second approach is termed *bottom-up*. It exploits the physical, chemical and biological principles of self-assembly. Even though the general trend of this nanostructuring can be guided by external conditions, the self-assembly process remains of statistical nature. In applications, *bottom-up* structured nanodevices are therefore characterized by an inherent randomness. In principle, high crystal quality and perfect crystal facets are possible even at very small sizes. An example of very well controllable self-assembly is the Molecular Beam Epitaxy (MBE) technique, where deposition of material with monolayer accuracy is possible.

In this thesis, two different concepts of nanostucturing are discussed: the self-assembled growth of nanowires and Cleaved Edge Overgrowth (CEO).

The semiconductor nanowires show all the characteristic properties of the *bottom-up* technique. In particular, the large amount of nanowires that are fabricated in one growth run and thus under identical growth conditions allows a systematic study of their properties dependent on the growth conditions. To that end, the nanowires are characterized by Transmission Electron Microscopy (TEM) and Raman spectroscopy. To be able to estimate the amount of randomness still involved in the self-assembled growth, it is of particular importance to characterize ensembles as well as single nanowires.

The CEO technique combines advantages of both the *top-down* and *bottom-up* approach. It is based on the property of the GaAs crystal to cleave atomically flat over macroscopic distance perpendicular to the [110] growth direction. By consecutive MBE growth and cleavage steps, crossings of perpendicular Quantum Wells are fabricated. In a *top-down* like manner, the nanostructuring is performed with MBE precision in all three spatial directions. Due to the atomically smooth cleavage, no additional surface damage is inflicted.

The combining element between these different aspects of semiconductor nanofabrication is the characterization by similar optical spectroscopy techniques. They comprise the main part of this work.

The thesis is structured as follows:

Chapter 2 gives a brief introduction to the theory of Raman scattering. Furthermore, the beam line set up for Raman spectroscopy of single nanowires is explained.

Chapter 3 introduces Ga assisted growth of GaAs nanowires by MBE. In TEM it is found that, dependent on the As_4 beam equivalent pressure (BEP) during growth, the nanowires have either pure zinc blende or a mixture of zinc blende and wurtzite structure. Three different regimes of BEP are examined with Raman spectroscopy. All regimes show good growth morphology, with phonon mode energies and Raman lineshapes being essentially those of the related bulk material. This corresponds well to the low defect density found in TEM analysis.

For ensembles of nanowires composed by a mixture of wurtzite and zinc blende structure, additional Raman modes are observed. They are located approximately 11 cm^{-1} to lower wavenumber than the TO phonon mode. This is in agreement with the theoretical expected spectral position of Raman modes in wurtzite GaAs.

In spatially resolved mapping scans of single GaAs nanowires, the additional Raman modes are observed to be localized in the end regions of the nanowire, where TEM analysis shows particular concentrations of wurtzite phase. It is therefore concluded that these modes indeed originate from wurtzite GaAs.

An additional observation of interest is the enhancement of the Raman signal of individual GaAs nanowires as compared to GaAs bulk material. This is probably due to an antenna-like resonance effect of the nanowires with the electromagnetic radiation of the exciting laser field.

Furthermore, we find that when the samples are deliberately heated by applying large laser power densities, irreversible structural change can be induced, leading to additional Raman features as well as a linewidth narrowing of the phonon modes. In accordance with literature, the additional features are attributed to annealing-induced oxidation of As. The linewidth narrowing is linked to annealing of defects within the nanowires.

Chapter 4 reports on Ga assisted growth of Si nanowires by Chemical Vapor Deposition. The crystal lattice of the Ga catalyzed nanowires contains a large amount of twins and stacking faults along several crystallographic directions, that further increases with decreasing growth temperature. While in TEM analysis the zinc blende structure is found to be the main crystallographic order all along the nanowires, in some regions nanocrystallites and nanotwinned arrays can be identified. These features coincide with the observation of an additional feature in the Raman spectrum.

Chapter 5 serves as an introduction to the second part of the thesis, which is concerned with the fabrication of CEO nanostructures and their examination by Photoluminescence (PL) spectroscopy. The basics of PL in low-dimensional semiconductors are explained, followed by sketches of the PL setups used for the measurements in the following chapter.

Chapter 6 first presents a refined growth concept for 2fold CEO nanostructures. Then several CEO samples are characterized by 1D and 2D mapping scans, power-dependent measurements as well as pulsed excitation. Based on spatial information as well as on spectral position, the excitonic ground state of the 2fold CEO QDs can reproducibly be identified. Its localization energy is with about 20 meV unexpectedly large for 2fold CEO QDs. Finally the possibility to electrically tune the CEO QD structures is examined.

Chapter 7 summarizes the main results and gives perspectives for future work in the two nanosystems discussed.

Chapter 2

Theoretical and experimental basics of Raman spectroscopy

In this chapter, the theoretical basis of Raman spectroscopy is briefly introduced, followed by a description of the setup constructed for the measurements of chapters 3 and 4.

Raman scattering is inelastic light scattering that leads to the creation or annihilation of elementary excitations in the probed medium. These excitations can be phonons as well as plasmons or other excitations. Creation processes are termed Stokes-scattering, annihilation processes anti-Stokes scattering. Depending on the number of elementary excitations involved, the scattering process is referred to as being of first, second or higher order.

2.1 The Raman tensor

The following discussion is restricted to Raman scattering in first order by the creation of a single phononic excitation. Raman scattering, or the photon-phonon interaction, is usually explained by the inelastic scattering between a virtual electron-hole pair excited by the photons and the lattice vibrations (phonons). Momentum $\vec{k}$ and polarization $\vec{\epsilon}$ have to be conserved for every step of the process. Since the light typically used for Raman scattering experiments has a wave vector of the order of 10^5 cm^{-1} (wave vector = 2 $\pi\times$ refractive index /wavelength) conservation of wave vector in backscattering geometry requires that the phonon involved must also have a wave vector of the order of 10^5 cm^{-1}. This is small compared to the width of the Brillouin zone (10^8 cm^{-1}) and the Raman phonons are thus close to the zone center. The scattering process is illustrated in figure 2.1. The electron-photon interaction leads to the creation of a virtual electron-hole pair (exciton). This exciton interacts with the lattice and emits a phonon. Then the exciton recombines and a scattered photon with reduced energy is emitted.

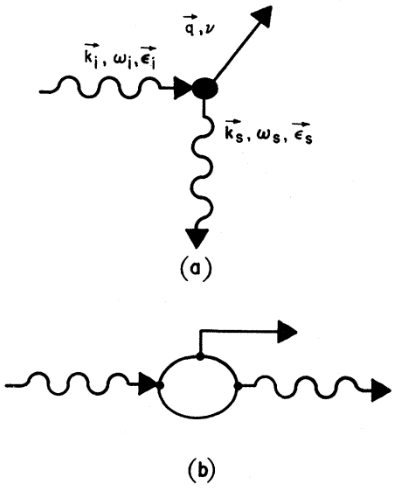

Figure 2.1: Raman scattering process. (a) Single scattering of a photon from the initial state $\vec{k_i}, \omega_i, \vec{\epsilon_i}$ to the final (scattered) state $\vec{k_s}, \omega_s, \vec{\epsilon_s}$ inside the crystal with the creation of a phonon of type ν with wave vector $\vec{q} = \vec{k_i} - \vec{k_s}$. (b) Microscopic diagram of one of six possible orderings of the interactions in Eq. (4) which contribute to (a). This diagram is the possibility described in the text. Adapted from [2].

The scattering amplitude is described by the Raman tensor **R**. The Raman tensor is derived from time dependent scattering theory in third order [1, 2] using the above described model. Only the expression for the one Feynman diagram shown in figure 2.1 is given. The total Raman tensor for Stokes scattering in first order is composed of six of these terms that can be deduced from permutations of the Feynman diagram due to invariance in time reversal for all three scattering steps.

$$\mathbf{R} = \frac{\mathbf{1}}{\mathbf{V}} \sum_{\mathbf{a},\mathbf{b}} \frac{\langle \mathbf{0}' | \mathbf{H}_{\mathbf{ER}} | \beta \rangle \langle \beta | \mathbf{H}_{\mathbf{EL}} | \alpha \rangle \langle \alpha | \mathbf{H}_{\mathbf{ER}} | \mathbf{0} \rangle}{(\omega_{\mathbf{i}} - \omega_\alpha)(\omega_{\mathbf{i}} - \omega_\beta - \omega_{\mathbf{0}})} \tag{2.1}$$

with

$$\begin{aligned}|0\rangle &= |n_i, 0; n_0; 0\rangle \\ |\alpha\rangle &= |n_i - 1, 0; n_0; a\rangle \\ |\beta\rangle &= |n_i - 1, 0; n_0 + 1; b\rangle \\ |0'\rangle &= |n_i - 1, 1; n_0 + 1; 0\rangle\end{aligned}$$

meaning (from left to right): number of impinging photons, number of scattered photons, number of phonons, electronic state. V is the crystal volume. The summation over a and b runs over complete sets of intermediate states of electron-hole pairs.

In equation 2.1 H$_{EL}$ describes the interaction of the electronic states with the lattice, H$_{ER}$ the interaction of the electronic states with the radiation field. In a polar lattice H$_{EL}$ comprises the short range deformation potential and the long range Fröhlich interaction. The deformation potential interaction originates from the perturbation of the periodic lattice potential by the phonon. The distortion of the lattice leads to a shift in the electronic levels. It enables dipole allowed scattering and is also possible for k→0. In homo polar crystals this is the only interaction process. In a polar crystal the LO phonons are in addition able to couple to the electronic states via their electric potential. This Fröhlich interaction is proportional to k^2 and therefore vanishes for k→0.

A further property of equation 2.1 are the strong resonance effects predicted if excitation energy or scattered energy coincide with real excitonic states. This can be exploited to not only probe the structural, but also the electronic properties of the material with Raman scattering.

2.2 Lineshape

The lineshape of the Raman signal is determined by phonons scattering with electrons, defects and other phonons. According to [1] this leads to the following differential scattering efficiency for photons being scattered into the frequency interval $[\omega_s, \omega_s + d\omega_s]$

$$S(\omega_s) = \frac{S}{\pi} \frac{\Gamma}{(\omega_i - \omega_0 - \omega_s - \Delta)^2 + \Gamma^2} \tag{2.2}$$

with S being the integral scattering efficiency over all scattering frequencies, ω_i the frequency of the incident photon, ω_0 the frequency of the Raman phonon and Γ and Δ being two constants describing the anharmonic terms in the Raman tensor that are mainly due to damping effects caused by the lifetime of the phonons [1]. Equation 2.2 describes a Lorentzian distribution with its maximum at $\omega_i - \omega_0 - \Delta$ with a FWHM of 2Γ. The absolute values of both Δ and Γ increase with the phonon populations. In most semiconductors, the majority of two-phonon states have an energy which is larger than the energy of the Raman phonon. With increasing temperature, the Raman line is therefore expected to broaden and shift to higher frequencies. In general, the difference in wavenumber between incident and backscattered photons is the measurement quantity given. This so-called Raman shift is therefore expected to decrease with increasing temperature.

2.3 Symmetry selection rules

The selection rules for Raman scattering are determined by the crystal symmetry. They are developed from scattering matrices deduced from the general Raman tensor describe dipole allowed (wavevector-independent) Raman scattering in first order. The general procedure is described in [3]. Table 2.1 lists the selection rules for zinc blende GaAs in backscattering geometry.

2.4 Micro-Raman setup

Fig. 2.2 depicts a schematic drawing of the beam line set up to enable spatially resolved Raman measurements on single nanowires.

2.4.1 Reduction of degrees of freedom

Optical fibers have helped to simplify optical spectroscopy experiments. The main advantage of optical fibers is that everyday adjustment is only necessary at incoupling and outcoupling of the fibers, and the efficiency of the alignment is quickly

(a) [001]	TO phonon	LO phonon
$z(x,x)\bar{z}$	0	0
$z(y,x)\bar{z}$	0	d^2_{LO}
$z(x',x')\bar{z}$	0	d^2_{LO}
$z(y',x')\bar{z}$	0	0
(b) [110]	TO phonon	LO phonon
$y'(x',x')\bar{y'}$	0	0
$y'(z,x')\bar{y'}$	d^2_{TO}	0
$y'(z,z)\bar{y'}$	d^2_{TO}	0
(c) [111]	TO phonon	LO phonon
$z''(x',x')\bar{z}''$	$2/3\ d^2_{TO}$	$1/3\ d^2_{LO}$
$z''(y'',x')\bar{z}''$	$2/3\ d^2_{TO}$	0

Table 2.1: Selection rules for Raman scattering in a bulk crystal of cubic symmetry. Conventional notation is used to describe the scattering geometry. The outer terms in the left column refer to the excitation and collection direction of the light. The inner bracket stands for excitation and detection polarization. d_{TO} and d_{LO} denote the non-zero Raman tensor elements for the TO and LO phonons, respectively. Three different illumination geometries are tabulated. Coordinate system (a) describes light impinging on the [001] surface, the nomenclature is x = [100], y = [010], z = [001]. Reversed direction is indicated by a bar. Coordinate system (b) describes light impinging on the [110] surface, the nomenclature being $x' = [1\bar{1}0]$, $y' = [110]$, $z' = z = [001]$. Coordinate system (c) describes light impinging on the [111] surface, the nomenclature being $x'' = [1\bar{1}0]$, $y'' = [11\bar{2}]$, $z'' = [111]$. Adapted from [4].

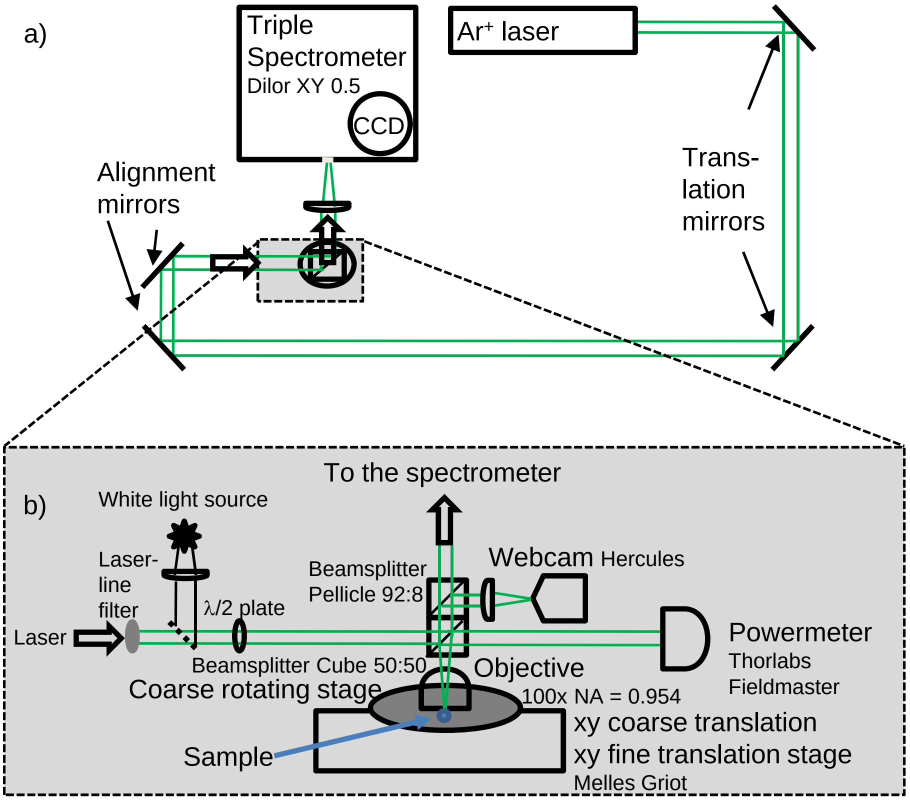

Figure 2.2: a) Overview of Raman setup beam line. Light emitted by the Ar$^+$laser (top right) is guided via translation mirrors to a set of two alignment mirrors. These two closely-spaced mirrors adjust the beam to go straight and centered onto the sample. The Raman signal backscattered by the sample is focused on the entrance slit of the triple spectrometer (top left), where the light is dispersed and detected with a CCD camera. b) Zoom-in on sample area. The laser light is filtered by a laser band pass filter (left). After that, a white light source can be coupled into the beam path via a semi-transparent mirror. A $\lambda/2$ wave plate allows to rotate the excitation polarization. After passing the 50:50 beamsplitter cube, half the light is deflected by 90° to go down through the objective (100 x; NA = 0.95), the other half is used for continuous power measurement (Thorlabs Fieldmaster). The sample is positioned on a coarse rotating stage, which is mounted on an xy coarse translation stage with a piezo-controlled computerized fine translation option. The emitted backscattered Raman signal is collected by the objective. 50% of the signal are deflected by the beamsplitter cube and another 8% are branched off by the 92:8 beamsplitter pellicle to image the sample geometry onto a Web cam (Hercules Classic Silver).

judged by the incoupled power. The guideline for the new design of the Raman setup is to reduce the degrees of freedom for alignment in a free-space setup as much as in a fiber-based setup and thus reach similar reproducibility and simplicity in alignment and maintenance.

To that end, a cage-system is used to interconnect most of the free-space optical elements. All the optical elements shown in part (b) in figure 2.2 are thus prealigned. The only alignment procedures necessary are, similar to fiber-based setups, the straight incoupling of the excitation light and the straight outcoupling of the Raman signal towards the spectrometer. With the help of the permanently fixed Web cam (middle right of part(b) in figure 2.2), the straightness of the incoupling can be well controlled with the two alignment mirrors (bottom left of part (a) in figure 2.2) in front of the cage-assembly by parallel shifting of the beam to get a centered excitation spot with concentric Airy patterns. The outcoupling is optimized by maximizing the signal of a bulk Si reference sample.

Raman selection rules that can be derived from the crystal symmetry can help identifying Raman signals (see section 2.3). For this purpose, a $\lambda/2$ plate is mounted in the cage-system (middle of part (b) in figure 2.2), so that measurements can be done for different excitation polarizations as schematically shown in figure 2.3. In Raman terminology, the two configurations sketched are: x(z,n.s.)$\bar{x}$ and x(y,n.s.)$\bar{x}$. The outer terms describe the excitation and collection direction of the light. The inner bracket stands for excitation and detection polarization. Z is per definition the crystal growth direction. In the measurements described here, the detection polarization is not specified.

2.4.2 Real-time imaging of single nanowires

In order to find a specific nanowire, a high magnification real-time imaging of the sample surface is necessary. This is achieved by coupling white light via a semi-transparent mirror into the excitation beam path (middle left of part B in figure 2.2). Due to the dispersion of the white light, a larger area of the sample (30x30 μm^2) is illuminated and imaged onto the Web cam together with the laser excitation spot. The microscope consisting of Web cam, focusing lens and objective magnifies by a factor of 10^4. If the nanowires are spread out on the sample in a sufficiently

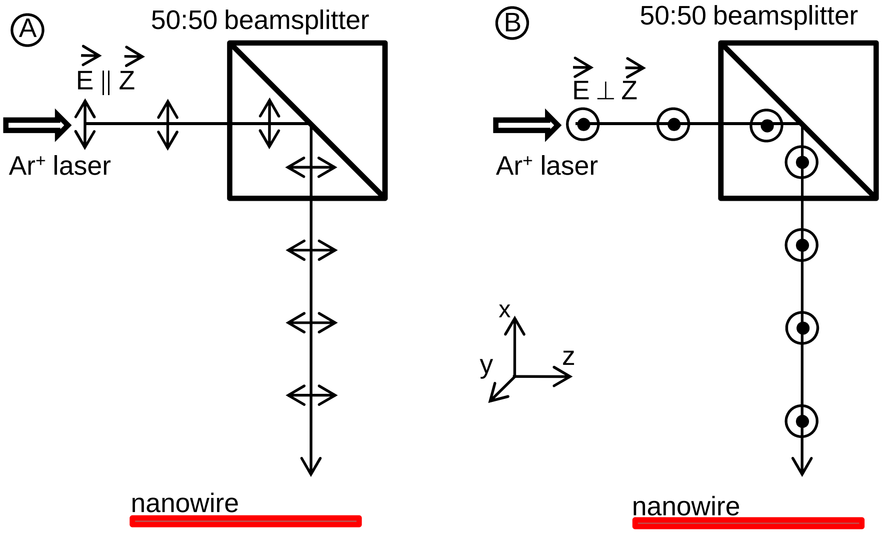

Figure 2.3: Two different configurations of excitation polarization. In configuration A, the electric field vector is parallel to the growth direction of the nanowire. In configuration B, the electric field vector is perpendicular to the growth direction of the nanowire. In the measurements described here, the polarization direction of the detection is not specified.

dilute manner, single nanowires can be clearly distinguished. The host substrate is structured by lithographically defined symbols, letters and numbers which serve as markers to identify individual nanowires. This can be observed in figure 2.4, where a typical Web cam image is shown. The dark crosses correspond to the markers on the substrate, while the long shadows correspond to the nanowires. Two nanowires (dark lines) are highlighted by white dashed lines. With their specific marker position, they can be reliably found again during another measuring session, or even for other characterization methods such as Photoluminescence or Atomic Force Microscopy.

2.4.3 Spectral and spatial resolution

The spatial resolution of the setup is limited by the beam waist of the exciting laser spot. The investigated nanowires range in width from 30 to 100 nm and in length from 0.5 to 10 μm [5, 6]. Scanning across the slim direction of the nanowires is used to determine the spatial resolution of the setup. Figure 2.5 shows a spatial scan across a single nanowire. The Gaussian fit yields a focal diameter of $\approx$ 640 nm. By quadratically subtracting the wire width of $\approx$ 30 nm, the FWHM of the laser can be approximated to be $\approx$ 640 nm.

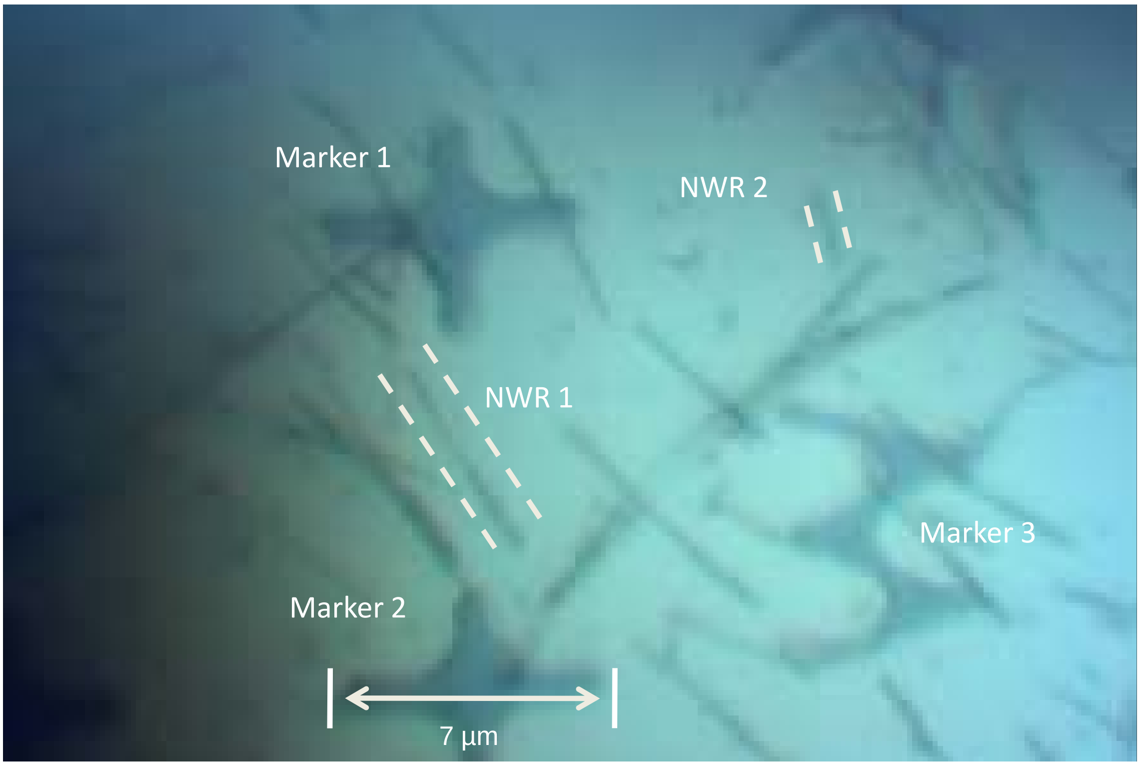

Figure 2.4: Web cam image of InGaAs nanowires spread out on a patterned substrate. 3 markers are shown (dark geometric structures). The diameter of the markers is 7 μm. Single nanowires appear as dark lines in the Web cam image. Two single nanowires are highlighted by dashed lines besides them. Nanowire 1 is about twice as long as nanowire 2. Both can be identified by their specific position with respect to the markers.

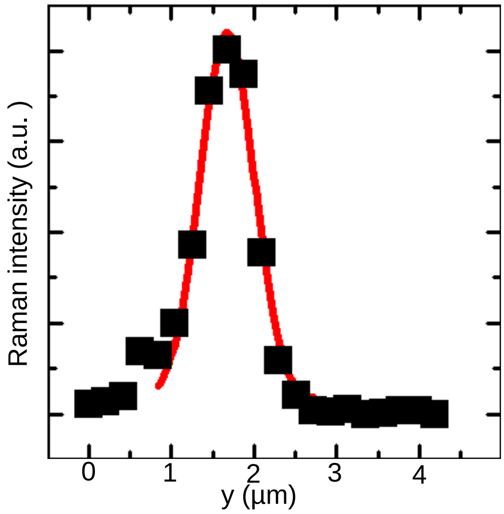

Figure 2.5: Spatial scan across the short direction of a single GaAs nanowire (step size 200 nm). The red curve is a Gaussian fit to the data, whose FWHM is a good approximation to the FWHM of the laser spot.

In Raman spectroscopy the excitation and detection signal are similar in wavelength. In GaAs the TO phonon mode has an energy shift of $\approx$ 270 wavenumbers, which corresponds to ΔE $\approx$ 34 meV, see figure 2.6. In this graph, elastically scattered laser light with $\lambda = 514.5$ nm corresponds to wavenumber 0.

At the same time, Raman spectroscopy requires high excitation powers. Efficient stray light rejection is thus mandatory for Raman spectrometers. Two out of the three spectrometer stages of the Raman spectrometer are therefore used exclusively for stray light rejection (so-called "subtractive mode"). Compared to the also available "additive mode", where all three gratings are used for dispersing the light, the spectral resolution is reduced. On the basis of a spectrum taken from the Ar^+ laser line, the spectral resolution is determined to be 1.15 cm^{-1} (FWHM of a Gaussian fitted to the laser line, as shown in figure 2.7). Further setup parameters that are relevant for the spectral resolution are: focal length of each spectrometer stage: 0.5 m, groove density of the gratings: 1800 grooves/mm, CCD pixel size: 26 μm, slit width: 200 μm.

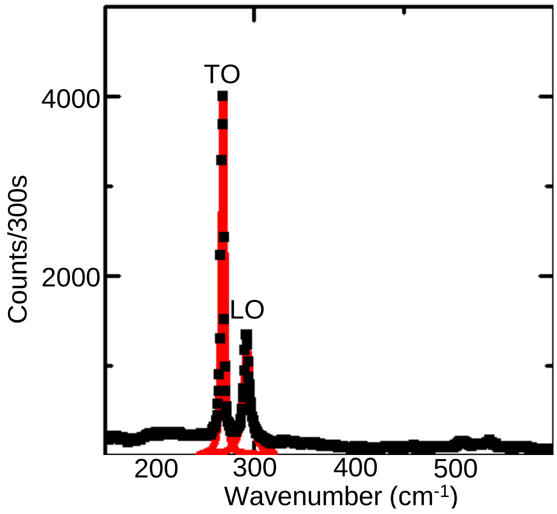

Figure 2.6: GaAs Raman spectrum obtained in backscattering geometry of a (111)B bulk GaAs wafer. Excitation power is 0.6 mW, integration time 300 s. The best fit is achieved if a Lorentzian peak shape is assumed (red curves). The FWHM of the TO phonon mode is 3.3 cm^{-1}.

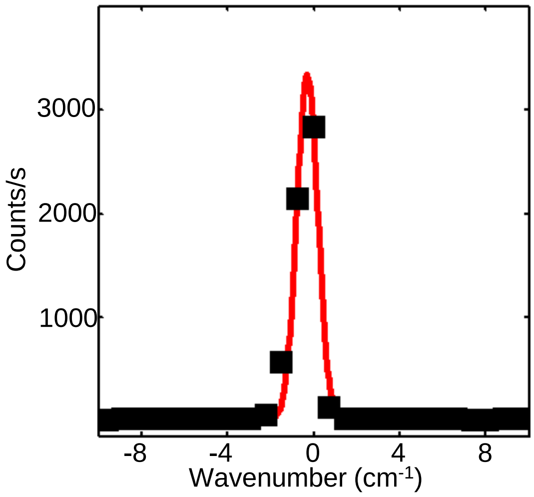

Figure 2.7: 514.5 nm Ar$^+$ laser line measured in subtractive mode with a spectrometer entrance slit width of 200 μm. The power is below 10 nW, the sensitivity of the power meter. The red curve is a Gaussian fit to the data, yielding a FWHM of 1.15 cm^{-1}. Since the laser line width is much narrower, the FWHM represents the resolution of the Raman detection unit.

Chapter 3

Raman spectroscopy of GaAs nanowires

The scope of this chapter is the characterization of Ga assisted grown GaAs semiconductor nanowires by Raman spectroscopy. The underlying motivation for the Ga assisted growth is the improvement of the optical and electronic properties of the nanowires by avoiding catalyzing materials such as Au that introduce deep level impurities into the semiconductor. This is a prerequisite towards device applications of semiconductor nanowires in optoelectronics. The nanowires are grown by Molecular Beam Epitaxy (MBE). They show good growth morphology, with Raman lineshapes and peak positions being essentially those of the related bulk material.

For single GaAs nanowires, an enhancement of the Raman signal is found as compared to GaAs bulk material. This is probably due to an antenna-like resonance effect of the nanowires with the electromagnetic radiation of the exciting laser field. When the samples are deliberately heated by applying large laser power densities, irreversible structural change can be observed that is attributed to annealing-induced oxidation of As.

Nanowires with pure zinc blende and a mixture of wurtzite and zinc blende structures are investigated. The crucial growth parameter to adjust the wurtzite content in the nanowire is the As_4 beam equivalent pressure (BEP). For nanowires composed of a mixture of wurtzite and zinc blende structure, additional Raman modes are observed that are attributed to wurtzite GaAs in accordance with theoretical calculations as well as Transmission Electron Microscopy (TEM) statistics. In certain regions of nanowires with the highest concentration of wurtzite phase, the wurtzite Raman signature can be of equal strength and comparable sharpness as the zinc blende Raman signal.

In spatially resolved mapping scans of single GaAs nanowires, the wurtzite Raman signature is observed to be localized in specific regions of the nanowire.

These findings might open up the road towards band-gap engineering within a single material system.

In this section Raman measurements of GaAs nanowires are correlated to growth parameters and TEM analysis.

The first subsection is an introduction to the growth of GaAs nanowires. Then the results of a TEM analysis are presented. The Raman analysis is started with measurements on ensembles of GaAs nanowires, followed by spatially resolved single nanowire mapping scans. The findings are statistically analyzed. Finally, the results are summarized and discussed.

3.1 Growth of GaAs nanowires

MBE offers the highest standards in terms of material purity and deposition accuracy of semiconductor growth today.

The growth of nanowires generally involves the use of metal droplets - usually gold - to catalyze the decomposition and gathering of the growth precursors. At the Walter Schottky Institute, it has recently been shown that Ga can be used to synthesize GaAs nanowires without the use of gold. This is achieved by growing under gallium rich conditions. A key issue is the use of a SiO_2 covered substrate to ensure the formation of gallium droplets.

The As_4 molecules provided by the MBE effusion cells impinge on the Ga droplet, decompose into As atoms and diffuse through the droplet following the As gradient. At the interface with the substrate (or nanowire), the As atoms alloy with the Ga atoms and form GaAs [5]. Continuous diffusion of gallium to the droplets and continuous impingement of As_4 on the droplets leads to a continuous growth rate, which is controlled by the As_4 BEP.

In the following, three GaAs nanowire growth modes with different As BEPs are examined.

The growth of the GaAs nanowires is performed by A. Fontcuberta i Morral at the Walter Schottky Institute.

3.2 TEM analysis of GaAs nanowires

The crystal structure of a GaAs bulk crystal is zinc blende. However, GaAs nanowires can also grow with pure wurtzite structure or a mixture of wurtzite and zinc blende [7, 8, 9, 10]. The physical reason for this behavior is believed to be the large surface-to-volume ratio in nanowires, which, dependent on growth conditions, size and length of the nanowires, leads to energetically favorable conditions for either wurtzite or zinc blende structure [11].

Transmission Electron Microscopy (TEM) and High Resolution Transmission Electron Microscopy (HRTEM) studies show that the crystal structure of Ga catalyzed GaAs nanowires varies as a function of As_4 BEP. The analysis is performed in the Group of Advanced Electron Nanoscopy in the Serveis Cientificotecnics of the Universitat de Barcelona, headed by J. Arbiol. Table 3.1 gives an introduction to the growth nomenclature used as well as a short summary of the TEM and HRTEM observations.

Sample	$P_{BEP}^{As_4}$(mbar)	TEM/ HRTEM observations	Nomenclature
02-18-08.1	3.6×10^{-6}	no pure wurtzite segments	high beam flux (HBF)
02-18-08.2	8.0×10^{-7}	short wurtzite segments at end of nanowire	low beam flux (LBF)
02-18-08.1	3.2×10^{-7}	longer wurtzite segments at end of nanowire	ultra low beam flux (ULBF)

Table 3.1: Growth conditions linked to TEM and HRTEM observations for the three different growth conditions examined. Lower As_4 beam flux results in larger wurtzite segments at the end of the nanowires. Growth temperature was 630 °C. Numerical values taken from [12].

A schematic drawing of zinc blende and wurtzite crystal structure is shown in figure 3.1, viewed along the [111] crystal direction. The zinc blende lattice has cubic symmetry, while wurtzite has hexagonal symmetry. This difference becomes apparent in the difference of stacking order of the {111} planes. The stacking sequence of the zinc blende structure is ABCABCABC (part (a) of figure 3.1). The stacking sequence of the wurtzite structure is ABABAB (part (b) of figure 3.1). The different stacking sequences can indeed be retraced in the HRTEM images discussed in the following subsection, since this high resolution technique makes individual atomic layers visible.

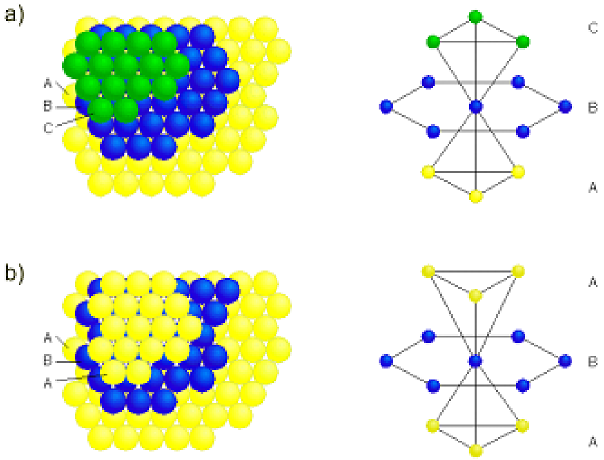

Figure 3.1: Stacking sequence of layers along the [111] direction for (a) zinc blende and (b) wurtzite crystal structure.

If two zinc blende regions have inverted stacking order, e.g. ABCABCBACBAC, this corresponds to a rotation of the crystal of 60° around the $[1\bar{1}1]$ axis or, equivalently, to the insertion of one monolayer of wurtzite. A detailed description of an analysis of such defects called twins as well a a model on how these twin planes form is developed in [16]. There the nanowires are described as connected segments of twinned octahedra. The twin defect occurs when one octahedron is rotated 60 ° with respect to its neighbors.

The Raman TO phonon mode of wurtzite GaAs is expected in the wavenumber region of the zinc blende TO phonon mode at the L point, since the Brillouin zone of GaAs wurtzite is half the size of the Brillouin zone of GaAs zinc blende [13].

3.2.1 HBF growth mode

Figure 3.2 shows a TEM picture of a nanowire grown in HBF growth mode. The total wire length is about 6 μm. The lower end of the nanowire corresponds to the end of the growth. As shown in the HRTEM image (a), apart from a short zinc blende segment, the wire starts with a wurtzite domain. As the growth proceeds (in the figure from top to bottom), the wurtzite domains are more often interrupted by zinc blende segments, till the volume is about equally distributed among wurtzite and zinc blende segments (image (c)). Further along, zinc blende becomes the dominant phase, only interrupted by occasional twin defects. These defects seem to correspond to the defects described in [16], since in image (f), light and dark phases as well as a slight micro faceting following the alternating [110] and [011] zinc blende facets are visible.

In summary, a typical HBF nanowire exhibits zinc blende structure of very good crystal quality with only occasional twinning sequences. Only the first 3% of the overall nanowire length contain larger segments of wurtzite.

3.2.2 LBF growth mode

Figure 3.3 shows a TEM analysis of a typical nanowire grown at medium arsenic beam flux. Contrary to the HBF nanowire in figure 3.3, here the Ga catalyst seed remains visible after growth. The seed is found to be amorphous (image (f)).

The length of the nanowire in the overview TEM image only slightly exceeds 1μm. As in figure 3.2, the earliest grown parts of the nanowire start at the top left corner of the figure. Image (a) shows a start of growth with a short zinc blende segment and an extended wurtzite domain, very similar to image (a) in figure 3.3. The wurtzite segments are longer than those seen in the HBF sample, with extensions up to 35 nm. As growth proceeds, the wurtzite segments become shorter (image (b)), until a close stacking of layers of wurtzite and zinc blende is reached (image (c)). The following region of the wire consists of pure zinc blende with very low defect density, showing good crystal quality (images (d),(e)). Very instructive is image (f) which shows the seed/nanowire interface. Just underneath the Ga droplet, a section containing thin wurtzite segments and a high twin density is found. At the end of each growth run, the sample holder is rotated away from the beam flux, thus reducing the As_4 pressure

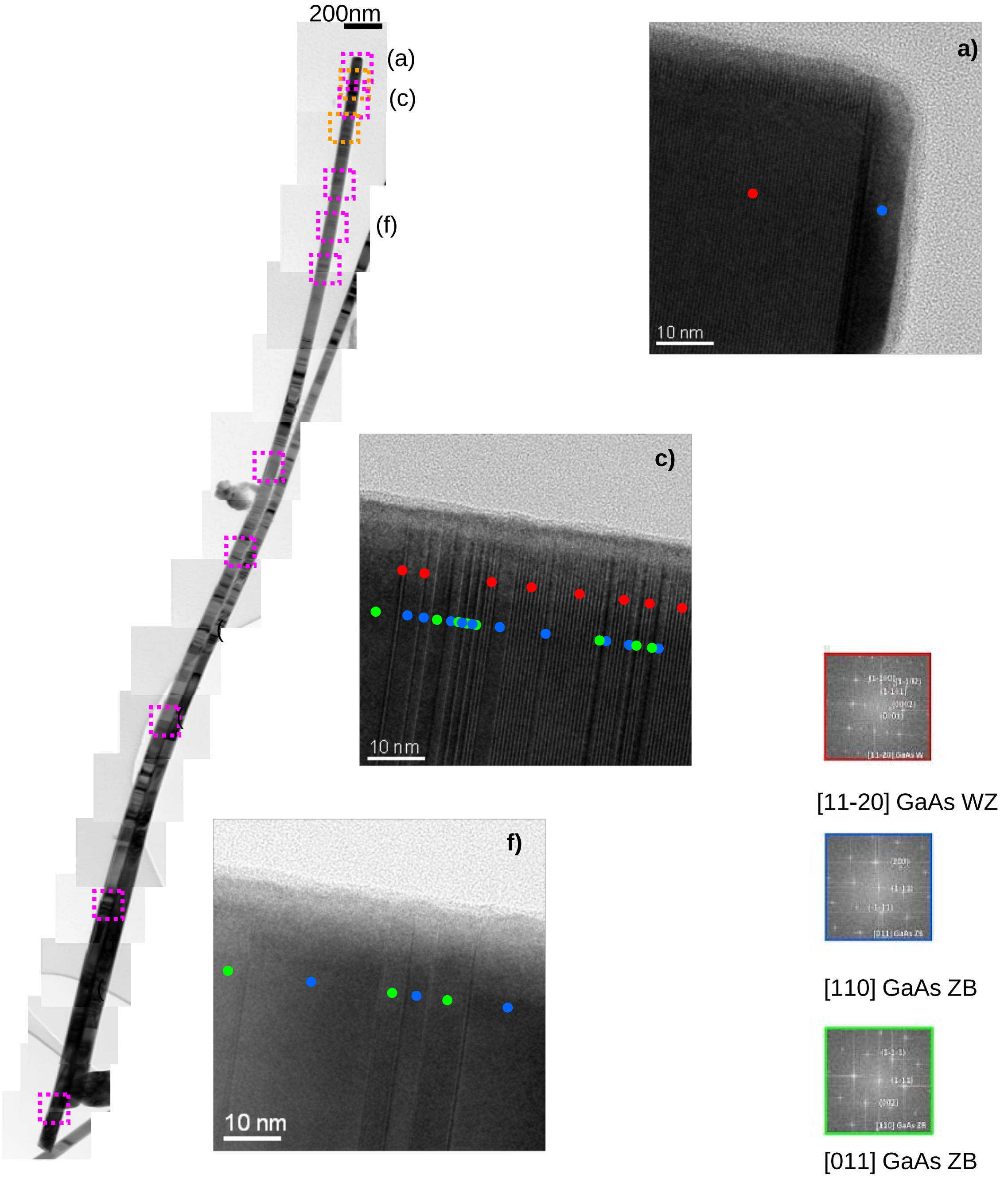

Figure 3.2: High-resolution TEM analysis performed on an HBF nanowire. From the many HRTEM zoom-ins indicated by dashed purple squares in the TEM overview image of the entire nanowire, exemplarily the images (a), (c) and (f) are shown (description in the text). Red dots mark wurtzite structure, blue dots mark [110] zinc blende structure, green dots [011] zinc blende structure. The characteristic FFT spectra of these crystal structures are shown in the same color code (right side).

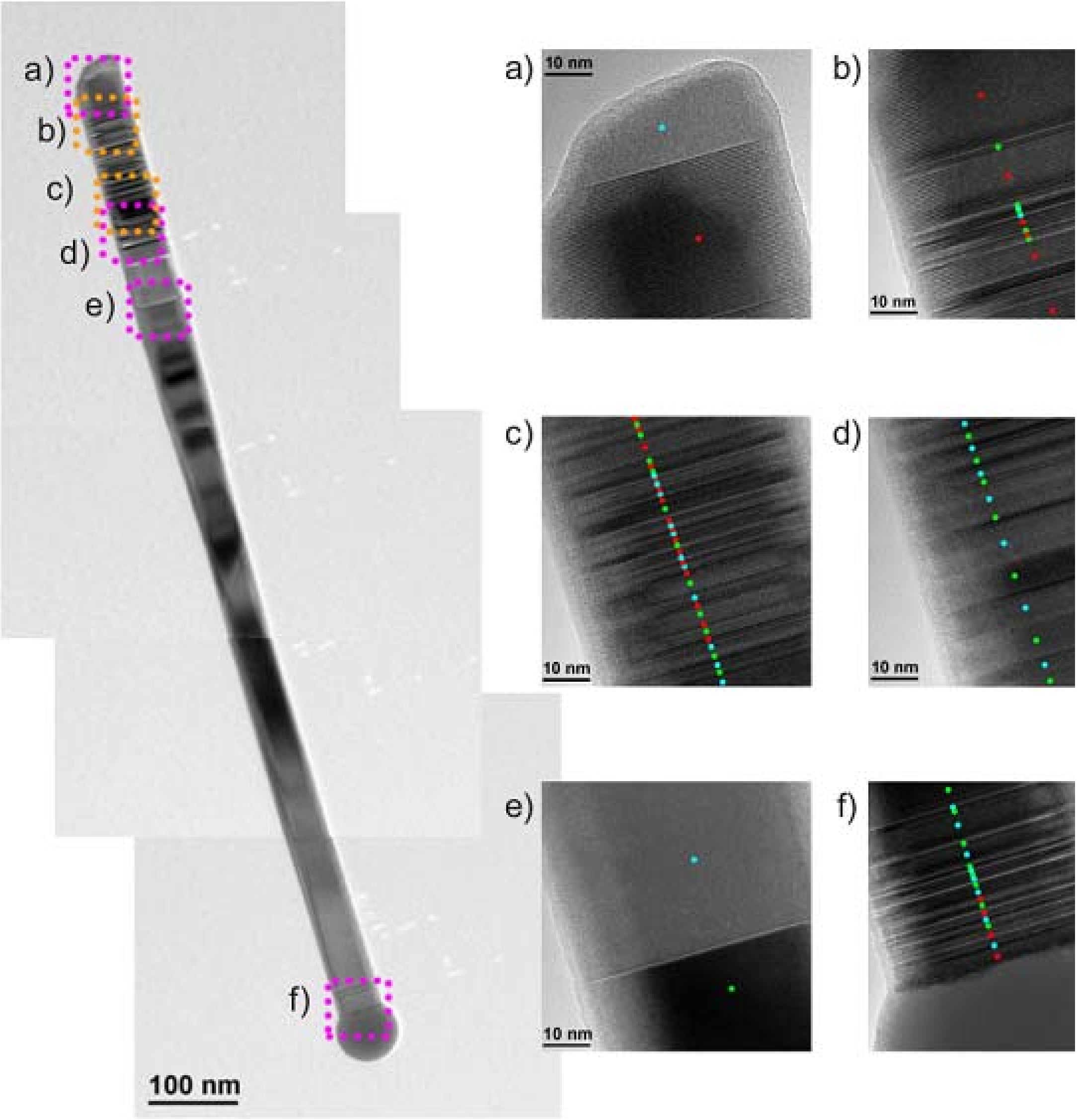

Figure 3.3: Overview TEM and zoomed-in HRTEM measurements with corresponding FFT analysis of a representative LBF nanowire. Red dots mark wurtzite structure, blue and green dots zinc blende structure.

even further before the growth comes to a halt. The finding of increased wurtzite and twin defect density in this region further underpins the strong influence of the arsenic BEP on the crystal phases of the GaAs nanowires. The fact that this is not seen in the HBF samples is probably correlated with the complete disappearance of the Ga seed: since the Ga seed seems to have been totally consumed by the HBF nanowire at the end of the growth, the growth might have come to a hold even before the wafer was actually moved out of the beam flux.

In summary a typical LBF nanowire differs from a typical HBF nanowire in that the percentage of nanowire volume containing larger segments of wurtzite increases from 3% to up to 30%. It should be noted, however, that the nanowires in this growth mode are on average significantly longer than it appears in TEM. This could be explained by a frequent breaking of the nanowires during the transfer and preparation processes necessary for TEM. While image (f) of figure 3.3 clearly shows the end of growth, the part shown in image (a) might actually not be the true start of the growth, but rather represent an intermediate section where the wire broke during transfer. In this context, it seems difficult to estimate the exact relation of wurtzite to zinc blende phase from these measurements.

3.2.3 ULBF growth mode

As expected, the largest wurtzite domains are present in ULBF nanowires. In figure 3.4 a TEM measurement of a ULBF nanowire showing single crystalline wurtzite domains with extensions of more than 60 nm is presented. Similar to the other nanowire growth modes, the transition of mainly zinc blende to mainly wurtzite segmented nanowire is manifested by a region of closely packed stacking faults. When the whole wire length is considered, over 1/3 of the total volume has wurtzite crystal structure. The rest of the wire exhibits zinc blende structure.

To summarize, with decreasing As_4 BEP a clear trend towards wider segments of wurtzite structure is seen in TEM analysis. Likewise the total amount of wurtzite found in the nanowires increases with decreasing BEP. In all three nanowire growth modes, the nanowires exhibit good crystal quality.

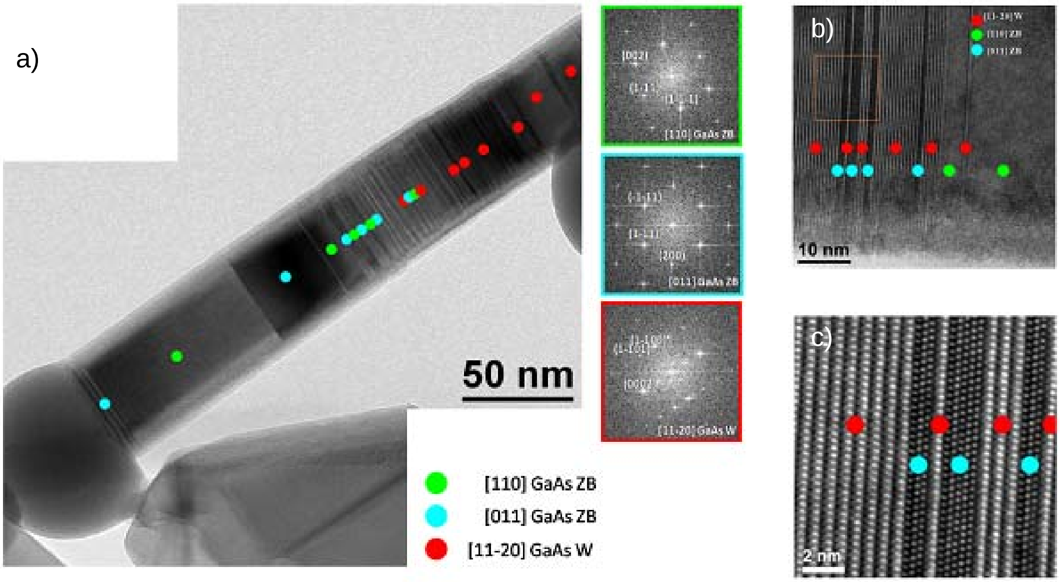

Figure 3.4: Image (a) shows a TEM measurement of a section of the end of a ULBF nanowire. The seed is clearly visible. Red, green and blue dots indicate crystal structure of wurtzite and two directions of zinc blende, respectively, as also shown in identical color code in the FFT pictures. Image (b) is a HRTEM measurement of the same wire. The area in the orange square of image (b) is further magnified in image (c). Individual atoms are now visible.

3.3 Raman measurements of GaAs nanowire bundles

Non-resonant Raman scattering is a very weak phenomenon, as only about 1 in every 10 million photons undergoes this inelastic process [1]. This is the reason why Raman measurements on nanostructures are usually realized on ensembles. Provided that the sample is homogeneous, this gives already valuable information on the sample structure. In the case of nanowires, the term bundle is used to describe ensembles. In order to separate the nanowire Raman signal from that of the substrate wafer, the GaAs nanowires are transferred to a Si host substrate. This is done by bringing the substrates into mechanical contact and carefully sliding them against each other. In this way, also the density of the nanowires on the host substrate can be controlled. If a patterned host substrate is used, single nanowires can be identified by the help of markers and reliably located again for subsequent examination.

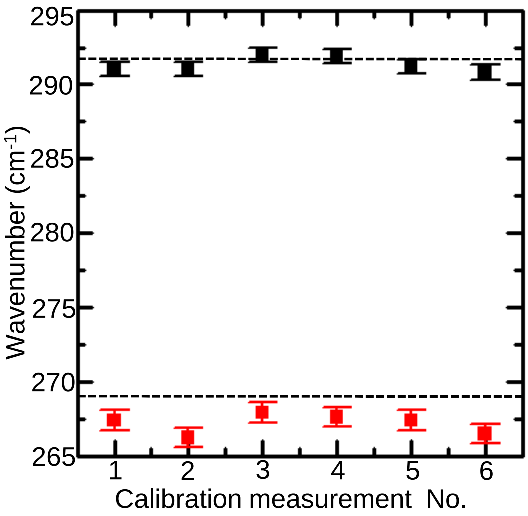

Figure 3.5: Measurement accuracy of the Raman setup. A GaAs (111)B reference sample is measured under identical conditions during the measurement period the data for this chapter is taken in. The spectra are calibrated according to the 520.7 cm^{-1} line of the Si reference sample which is measured immediately prior to each GaAs (111)B reference measurement. Red squares indicate the central wavenumber of the TO phonon mode, black squares the central wavenumber of the LO phonon mode. The standard deviation is plotted as error bars. Black dotted lines mark the literature values for TO and LO Raman phonon modes at 300°K [15].

All nanowire spectra are calibrated by measurements on a GaAs reference sample that are performed prior to each measurement series.

To estimate the longterm stability of the setup, six gauge measurements of the GaAs (111)B reference sample are performed during the measurement period of the data taking. To that end a standardized intrinsic Si reference sample is measured and the deviation of the Si Raman line to the literature value of 520.7 cm^{-1} is determined. Subsequently the GaAs (111)B reference is measured and corrected with the Si deviation value. A Lorentzian fit determines the centers of TO and LO phonon modes. These values are plotted in figure 3.5. Excitation power used for all measurements is always $\approx$ 0.5 mW. Red squares indicate the Si-corrected positions of the TO phonon lines, black squares the corrected positions of the LO phonon lines. Dotted lines show the literature value expected for a sample temperature of 300°K of 269 cm^{-1} and 292 cm^{-1}, respectively [15]. Especially the TO value is shifted to lower wavenumbers as compared to the literature value. Its average value is 267.2 cm^{-1} with a standard deviation of 0.67 cm^{-1}. The average LO value is 291.3 cm^{-1} with a standard deviation of 0.5 cm^{-1}.

First, the Raman spectra of nanowire bundles of all three growth modes are compared to the GaAs reference. Then a power-induced structural change is discussed.

3.3.1 Overview for all three growth modes

Figure 3.6 shows a spectrum of the bulk GaAs (111)B reference (graph (a)) and a representative measurement of a nanowire bundle for each GaAs nanowire growth mode (graphs (b) to (d)) in the spectral range between 250 and 300 cm^{-1}. Each plot is the average of five traces taken at a constant position for the integration time given in the figure. For the interpretation of the spectra, the averaged measurements are decomposed into 3 or 4 Lorentzians. Excitation power used is (a) 0.5 mW, (b) 0.26 mW, (c) 0.5 mW and (d) 0.6 mW. All spectra show a significant background of up to 0.4 counts/s. This background is attributed partly to dark counts in the electronics of the detection unit, partly to impurity scattering in the semiconductor as well as scattering in air. The background is excluded in the fitting procedure.

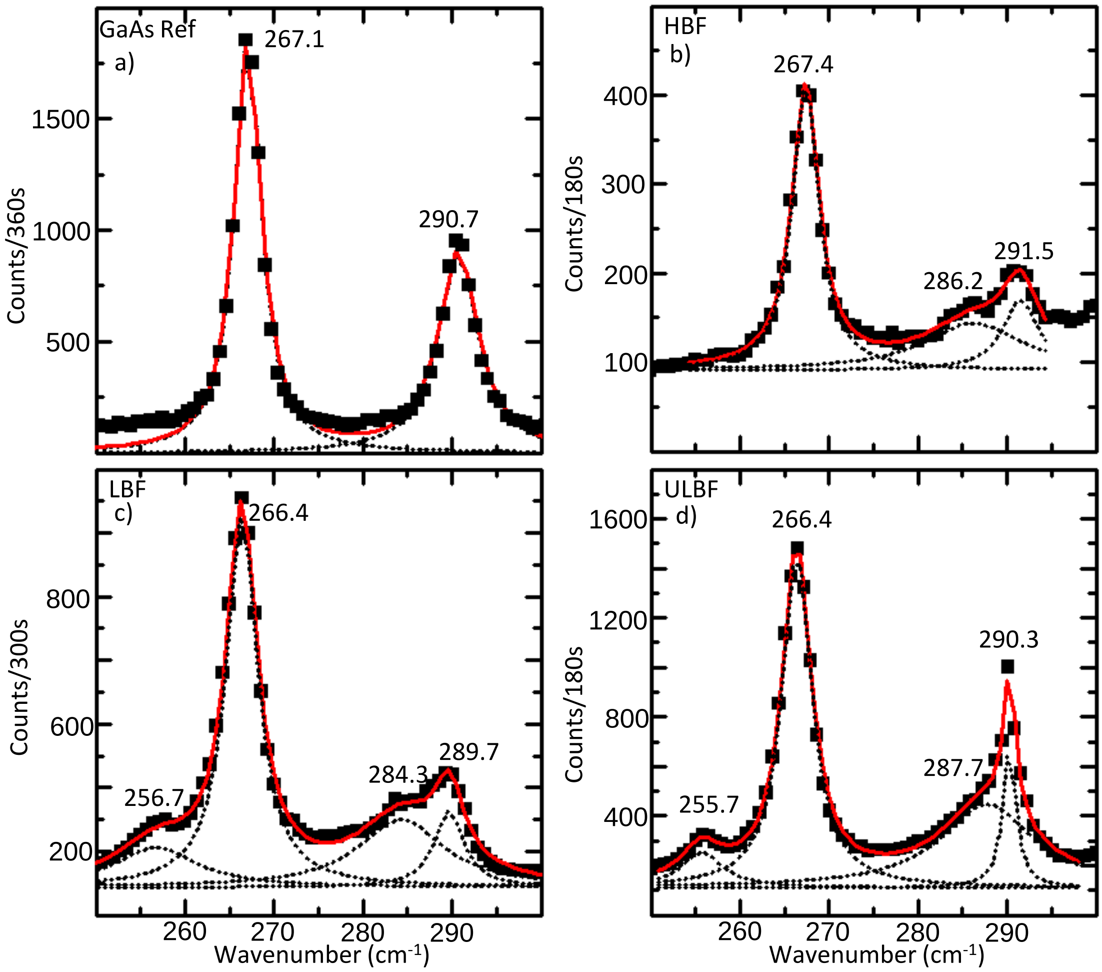

Figure 3.6: Raman spectrum of (a) the bulk GaAs reference sample and of (b) HBF, (c) LBF and (d) ULBF nanowire bundles. The data points are shown as scatter plots (black squares), the red solid line is the sum of the individual Lorentzians (individual peak fits: black short-dotted lines). Excitation power used is (a) 0.5 mW, (b) 0.26 mW, (c) 0.5 mW and (d) 0.6 mW.

HBF bundles

The best fit to the Raman signal of the HBF bundles (graph (b) in figure 3.6) gives the decomposition into three Lorentzians. Apart from the LO and TO phonon modes, a third feature close to the lower wavenumber side of the LO phonon mode is visible at $\approx 286\ \mathrm{cm}^{-1}$. This resonance is attributed to surface phonons (SO phonon mode) in accordance with [22]. The center values of TO and LO phonon modes of the HBF Raman signal lie within 0.3 σ of the average center values of the TO and even within 0.2 σ of the average center values of the LO phonon modes in the GaAs reference (see figure 3.5).

It can therefore be concluded that apart from the surface phonon and the appearance of the LO phonon mode in a scattering geometry where it would be in principle forbidden from the Raman selection rules (see chapter 2), the Raman signature of HBF nanowires corresponds to the Raman signature of bulk GaAs.

LBF bundles

In addition to the TO, the LO and the surface phonon signature, the spectrum of the LBF bundles (graph (c)) shows an additional resonance at $256.7\ \mathrm{cm}^{-1}$. Because of its spectral position, this feature is dubbed below-TO (BTO) in the following discussion.

The TO and LO phonon modes of the LBF Raman signals lie 1.2 σ and 3.4 σ below the average value of the GaAs reference.

ULBF bundles

The BTO peak is also found in the spectrum of the ULBF bundles (graph (d)). Compared to the BTO peak present in the LBF bundles, it is shifted by 1 unit in wavenumber to lower wavenumbers. The TO phonon mode lies 1.2 σ below the TO value of the GaAs reference, the LO phonon mode 2.2 σ below the LO value of the GAs reference.

The spectral position $\approx 10\ \mathrm{cm}^{-1}$ to lower wavenumber as compared to the TO phonon mode as well as its exclusive appearance in the LBF and the ULBF bundles hint at a wurtzite origin of the BTO peak. As will be shown in the measurements on single wires, the shift in the peak positions assigned to the TO and LO modes varies along the wire. A possible explanation is that this is a signature of stress of the zinc blende phase in proximity of the wurtzite phase due to lattice mismatch.

3.3.2 Power series of ULBF nanowire bundles

To avoid heating is an important aspect of Raman spectroscopy of nanowires. Heating shifts and asymmetrically broadens the Raman lines. This effect is also known for bulk samples. Due to their special geometry and free disposal on the substrate, nanowires cannot dissipate the laser-induced heat as effectively as bulk material. Therefore measurements on each nanowire sample first start with a power series to determine how much laser power can be maximally applied before the TO and LO phonon modes start to shift.

Here we show an additional effect in which heating of the sample is correlated with the occurrence of structural change, as additional Raman signatures appear with increasing laser power.

Figure 3.7 shows a power series of ULBF nanowire bundles. The data is shown in black squares, the overall fit is shown as a red line. Black curves represent the individual peak fits. The power is increased from 0.5 mW to 3 mW. The TO and LO phonon modes show the well-known downshift and linewidth broadening of phonon modes with excitation power [17]. In addition, the high power treatment also leads to the appearance of two new Raman features: the already discussed BTO feature and a second feature with its center around 198 cm^{-1}. This feature is termed below-BTO (BBTO) in the following.

Three power regimes can be distinguished: for the three lowest powers (top row in figure 3.7), no significant change is observed. As power is increased further (middle row in figure 3.7), the SO phonon mode becomes first more pronounced (best visible in graph (e)) before the increasing linewidth of the main Raman modes makes a distinction between LO and SO Raman features impossible (graph (f)). In the high power regime (bottom row, graphs (g) to (i)), the intensity of the Raman signal of the nanowires is increased such that the background cannot be clearly separated from the Raman features anymore. Most striking is the simultaneous appearance of two strong Raman features in the BTO and BBTO region. At highest power,

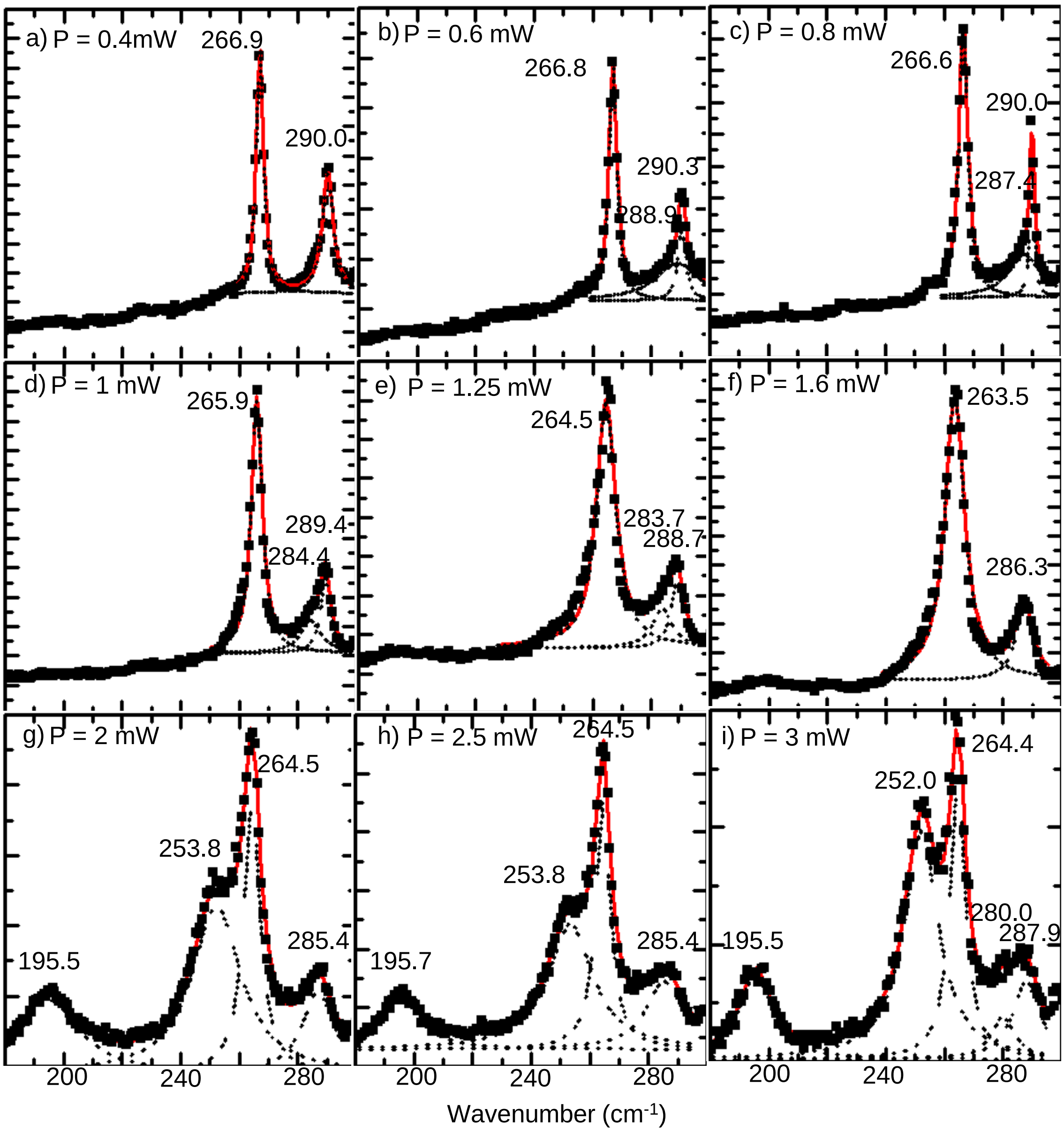

Figure 3.7: Power series on a ULBF nanowire bundle. Power is increased from 0.5 mW (top left) to 3 mW (bottom right) . Each graph shows an averaged spectrum (data points: black squares) for a specific power that is fitted with a Lorentzian multi peak fit. The red line shows the combined fit, the black dotted lines are individual peak fits. Integration time is decreased with increasing power, from 360 s in graph (a) down to 20 s in graph (i). With higher power, the Raman features become broader and shift to lower wavenumbers. Additional Raman features arise.

the BTO feature is almost as intense as the TO phonon mode. When comparing the TO and LO phonon modes of minimal and maximal power, a shift to lower wavenumbers of 2.5 cm^{-1} and 2.1 cm^{-1} is detected for the TO and the LO phonon mode, respectively.

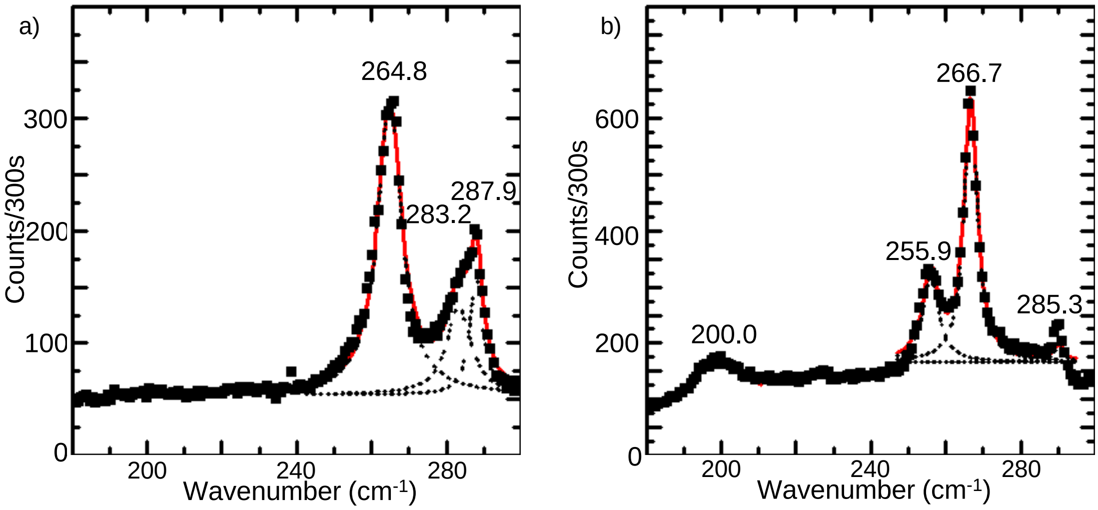

Figure 3.8: Before (graph a)) and after (graph b)) a power series on LBF nanowires. On each graph, a Lorentzian multi peak fit is performed on the average of five traces taken. The data is shown in black squares, the overall fit is shown as a red line. Black dotted curves represent the individual peak fits. In graph (b) the FWHM of the TO and LO phonon modes is clearly reduced, and BTO and BBTO Raman features are visible that cannot be discerned in graph (a). Power is 0.16 mW and integration time 300 s for both graphs.

Similar observations are made in a power series of a LBF nanowire bundle. Figure 3.8 shows two averaged spectra of the LBF nanowire bundle at the same excitation power (0.16 mW). In between the measurements displayed in graphs (a) and (b), the power is increased up to 3 mW to perform a power series similar to the data presented in figure 3.7 and decreased again without change of position. The Lorentzian fits (red line, single peak fits displayed as black dashed lines) show that the linewidth of the TO and LO phonon modes is reduced after the power treatment (FWHM = 4.4 cm^{-1} after annealing as compared to 7.8 cm^{-1} before annealing). Furthermore, graph (b) shows two additional Raman features in the BTO and BBTO region that are not present before the power treatment (graph (a)). This suggests that the power treatment has an irreversible annealing effect on the nanowire bundles.

In literature, Raman features in the BTO and BBTO wavenumber region have been linked to As segregates on the surface of annealed GaAs [18, 19]. In figure 3.9, adapted from [18], the same two additional Raman features are emerging as a function of annealing temperature as is the case for the ULBF nanowire bundle in the power series shown in figure 3.7. The features called E_g and A_{1g} correspond to the BBTO and BTO wavenumber region. Like in the case of the power series performed on GaAs nanowire bundles, both features start to appear simultaneously once a threshold annealing temperature is reached. It is therefore concluded that the BTO and BBTO peaks of GaAs nanowire bundles that appear after an annealing procedure also originate from As segregates on the surface of the GaAs nanowires. As is the case for the GaAs interfaces analyzed in [19], the GaAs nanowires also have a high surface to volume ratio. Furthermore, the experiments are performed in ambient conditions, providing the possibility for oxidation processes. The annealing effect is only observed in LBF and ULBF nanowire bundles, never in HBF. A similar effect is also seen in one heat treated single nanowire grown in ULBF growth mode (discussed in further detail in section 3.4). The growth conditions therefore also seem to play a role in the effects of the annealing process.

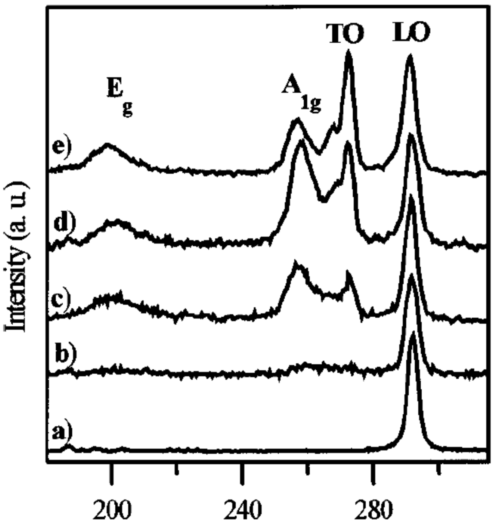

Figure 3.9: Raman spectra with 457.9 nm exciting light, as a function of annealing temperature at (a) unannealed, (b) 450, (c) 500, (d) 600, and (e) 650 °C for 30 min. Figure and caption adapted from figure 1 in [18].

For further clarification of the influence this annealing procedure has on the crystal quality of the nanowires a TEM analysis on annealed nanowires would be useful.

Since a narrowing of the TO and LO phonon modes is observed, an annealing of defect also takes place, resulting in a better structural quality of the nanowires. This could be developed towards an easy and effective technique for improving the structural quality of the nanowires. Dependent on whether the As segregation is welcome or undesired, a change from ambient to vacuum conditions could further enhance the control over the annealing procedure.

3.4 Raman analysis of single GaAs nanowires

The information that can be gained from measuring single nanowires is much more precise than the information gained from bundle measurements. With spatial resolved mapping scans, specific signals can be attributed to specific regions of the wires and may even be linked to certain stages in the growth procedure. Furthermore, polarization-dependent measurements are possible, since the orientation of a single nanowire with respect to the laser polarization is well-defined. The nanowire under examination is oriented with a rotating stage in such a way that its long direction points along one axis of the piezo stage. Probing positions are reproducible due to markers on the substrate that make it possible to identify individual nanowires. To obtain statistically relevant results, it is mandatory to measure several individual nanowires under the same measurement conditions.

This chapter describes and compares measurements on single nanowires of the HBF, LBF and ULBF growth regime. In each case five individual single nanowires are analyzed.

3.4.1 HBF nanowires

Line scan

Figure 3.10 shows a mapping scan along a single nanowire grown under HBF conditions (see table 3.1). Only the TO phonon mode is visible. We do not observe a LO Raman signal in agreement with Raman selection rules. When the polarization is turned from configuration A to configuration B, the signal disappears completely. A similar behavior is also observed in the other growth modes and follows from the selection rules: as can be inferred from table 2.1 in chapter 2, only one direction of incident polarization leads to excitation of a TO phonon when light impinges on surfaces of the $\{110\}$ surface family.

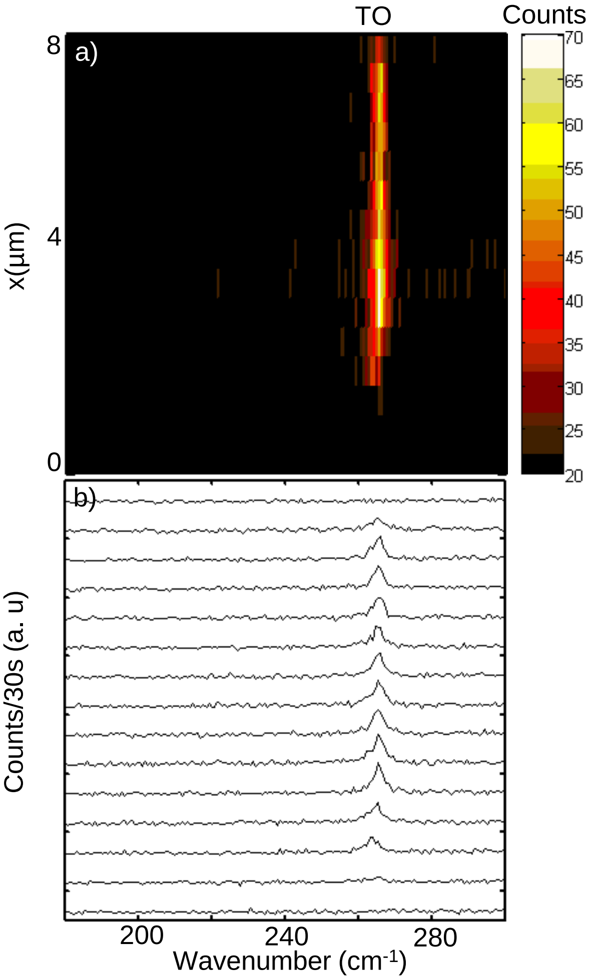

Figure 3.10: 1D scan along a single nanowire grown in HBF mode (HBF2). Step size is 0.5 μm, excitation power 0.35 mW, 30 s integration time per trace. (a): 2D color map (wavenumber vs. position) of a 1D scan along the nanowire in polarization configuration A. Color coded is the Raman intensity. The only signal visible is the TO phonon mode that extends over 6 μm. This is a typical length for a HBF nanowire. (b) Waterfall plot of the same data. Each trace is offset by 50 counts.

3.4.2 LBF nanowires

Line scan

Figure 3.11 shows a linescan along a single nanowire grown under LBF conditions. The total scan length is 7 μm with the nanowire being ≈ 5 μm in length. Step size is 100 nm. Only polarization configuration B is shown, in polarization configuration A, likewise to the ULBF scan shown in figure 3.12, the BTO peak disappears while the TO phonon mode is considerably weakened.

Keeping the TEM data in mind, the lower end of the scan (at x ≈ 1 μm) is most likely equivalent to the segment just below the Ga seed, since this segment shows in TEM analysis a particularly richness of twin defects (see figure 3.3, image (f)). Irregularities in the lattice can lead to a relaxation of the Raman selection rules that suppress the LO phonon mode in the scattering configuration used. The main part of the wire is zinc blende structure with very little twins. Thus the selection rules are intact here and only the TO zinc blende Raman signal is observed. Towards the end of the scan at x ≈ 6 μm, a BTO peak appears, while the intensity of the TO phonon mode is reduced. This region is attributed to the early stage of growth, were the nanowire starts with a large segment of pure wurtzite. The detailed spatial information gained from the line scan further supports the interpretation that a solitary BTO Raman feature originates from wurtzite GaAs.

3.4.3 ULBF nanowires

Line scan

Figure 3.12 shows a representative data set for a single nanowire grown under ULBF growth conditions (ULBF2). For each polarization direction, a 1D linescan with a step size of 200 nm is performed along the long direction of the wire. Data are presented as 2D color maps (upper graphs) as well as in the form of waterfall plots (lower graphs). From the presence of the LO phonon mode, the growth morphology of ULBF nanowires can be assumed to lead to the relaxation of selection rules due to frequent interruptions of crystal symmetry e.g. by twins or wurtzite intervals.

When the polarization is turned from configuration A to configuration B a third peak becomes visible ≈ 11 cm^{-1} below the TO phonon mode in the BTO region of

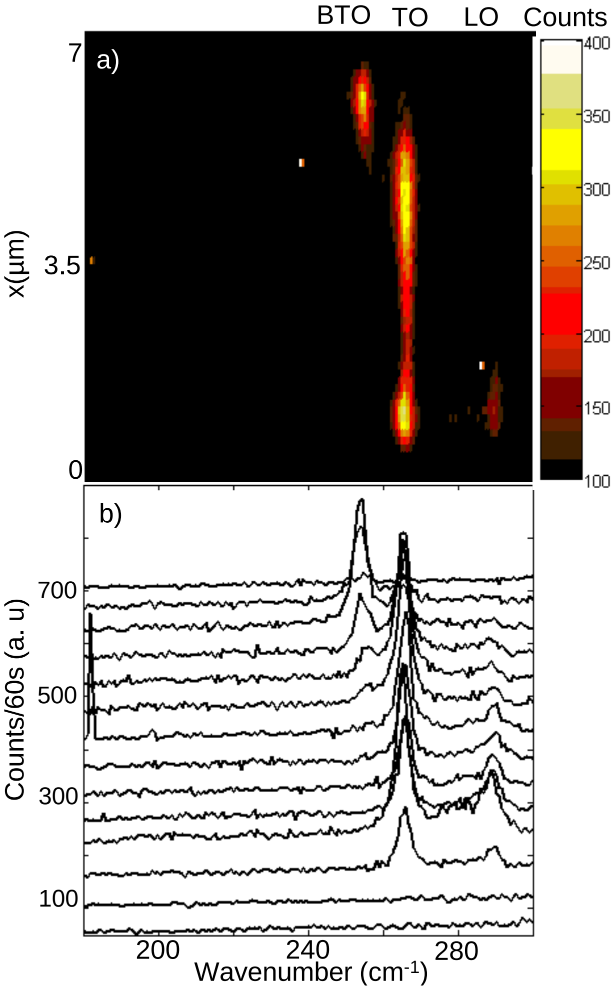

Figure 3.11: Linescan on a single LBF nanowire (LBF3). Graph (a) shows a color plot, graph (b) a waterfall representation of the same data set (every fifth trace shown). Scan step size is 100 nm. Power used 0.3 mW, polarization configuration B. Each trace is integrated for 60 s. The solitary BTO as well as the LO phonon mode are only visible in a ≈ 1 μm long section.

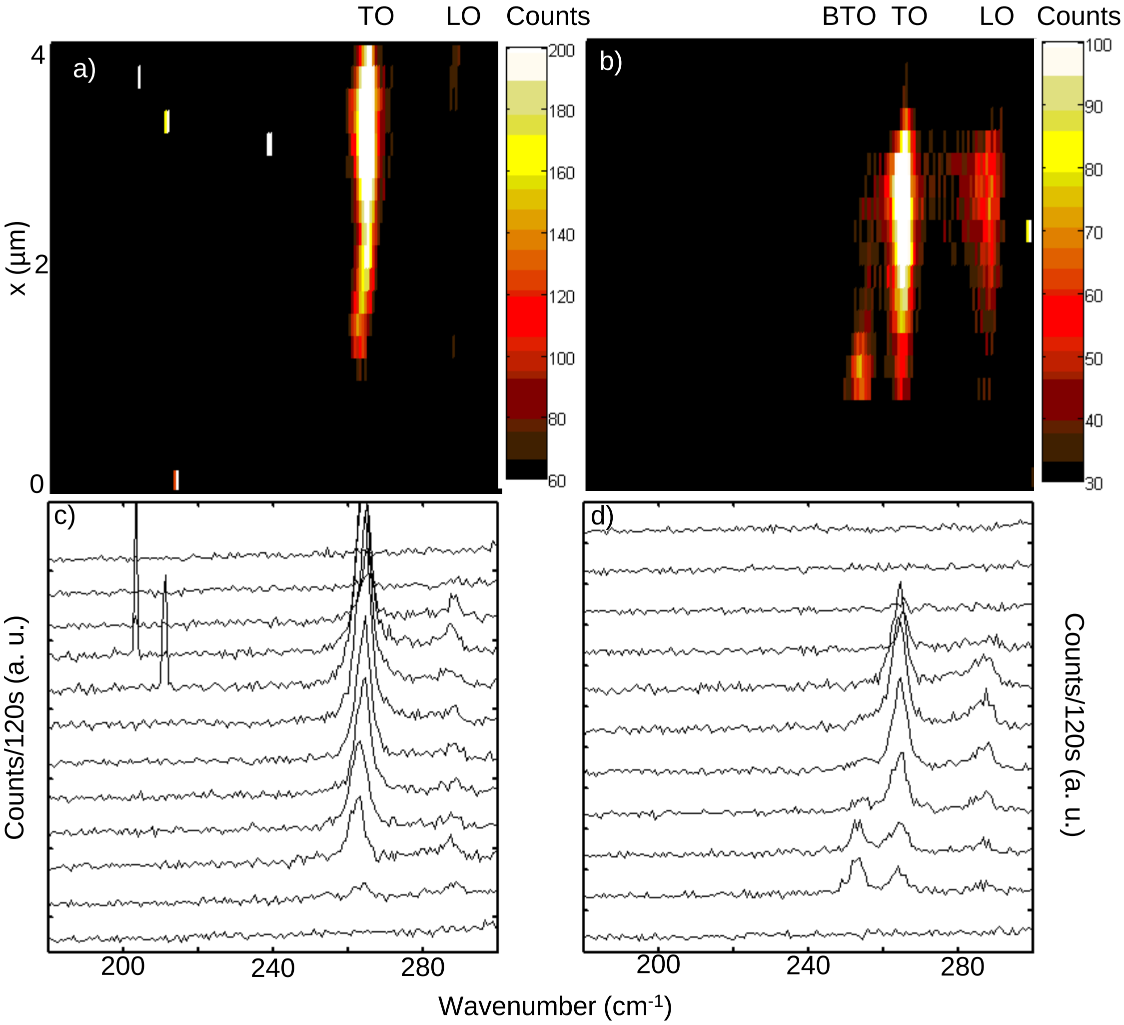

Figure 3.12: Representative data set taken for a single nanowire in the ULBF growth mode (ULBF2). (a): 2D color map (wavenumber vs. position) of a 1D scan along the nanowire in polarization configuration A (parallel polarization). (b): same plot for polarization configuration B (transverse polarization). Step width is 200 nm, power is 0.36 mW. Each trace is integrated for 120 s. The scanning region is not identical: the scan shown in graph (a) is shifted ≈ 1 μm to higher x as compared to the scan shown in graph (b). (c) Waterfall plot for parallel polarization , (d): waterfall plot for transverse polarization. Only every second trace is shown for clarity. In transverse polarization, an additional signal appears at wavenumbers in the BTO region below 260 cm^{-1} which is not visible in parallel polarization.

the spectrum. It is detected exclusively in an about 600 nm long section at one end of the nanowire and has a suppressing effect on the TO phonon mode intensity. The BTO peak is of comparable sharpness and intensity as the TO phonon mode.

These 1D scans are representative for three out of five ULBF nanowires scanned in both polarization configurations (ULBF2, ULBF3 and ULBF5). The nanowire ULBF1 does not show the BTO peak at all, while ULBF4 exhibits a BTO peak as well as a BBTO feature. A spatial scan of ULBF4 is presented in figure 3.13. For ULBF4, the strict excitation polarization selection rule for the BTO peak is not valid, instead, BTO as well as BBTO peak appear in both excitation polarization configuration, as can be inferred from figures 3.13 and 3.14. A further difference between figures 3.12 and 3.13 is that in the case of ULBF4 the BTO line does appear in the middle of the wire, while in the case of ULBF2, as in all other ULBF nanowires examined, the BTO is only visible at one end of the nanowire.

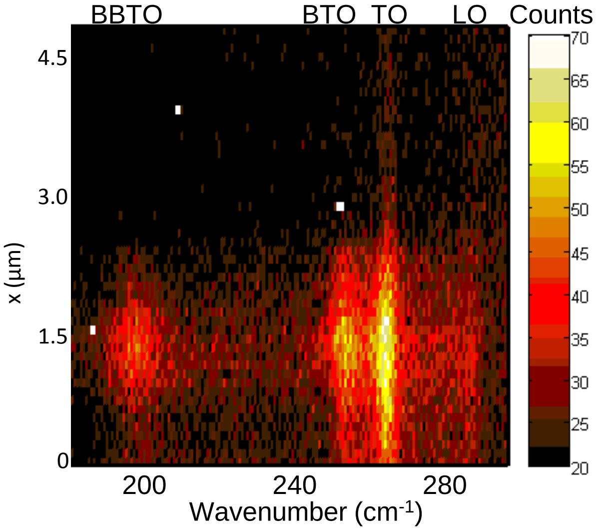

Figure 3.13: 1D scan along the single nanowire ULBF4 in polarization configuration B. Step width is 100 nm, excitation power 0.32 mW. Each trace is integrated for 30 s. The LO phonon mode is very weak. Besides the TO phonon mode and the BTO Raman feature which are also visible in other ULBF nanowires, an additional BBTO feature appears at the same spatial position as the BTO peak. This line is weaker in intensity and of broader spectral width than the other Raman features.

Similar to the power series performed on the nanowire bundles, ULBF4 was subject to higher laser excitation power prior to the recording of the scans shown.

Focus scan

To estimate the influence of the focus on the Raman signal of a single nanowire, a focus scan is done on ULBF4 in polarization configuration A (Figure 3.14). This viewgraph shows that the BBTO signal appears when all other Raman signals from the nanowire are also at their maximum intensity. The focus position has to be accurate to only a few microns, since the main Raman signals are visible over a range of more than 6 μm.

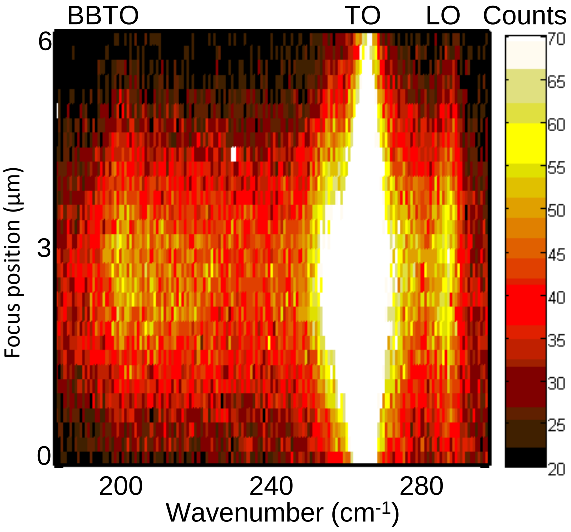

Figure 3.14: Scan of the focal distance for constant lateral excitation position in polarization configuration A. Scanning step width is 200 nm. Each trace is integrated for 30 s, power used is 0.32 mW. The amplitude of all signals is focus-dependent. The TO phonon mode remains visible all along the the scanning range. When LO and BBTO features become visible around 3 μm, the TO phonon mode broadens towards lower wavenumbers into the BTO spectral region.

Summary of scans of single nanowires

Even though the BTO peak in the single nanowires appears at a very similar spectral position as the BTO feature in the heated nanowire bundles and the single heat-treated nanowire ULBF4, it is believed to have a different physical origin for the following reasons:

- strong excitation polarization dependence;
- absence of accompanying BBTO peak;
- spatial localization at one end of the nanowires;

- sharper linewidth;
- no prior annealing necessary.

Instead of being As-related as the BTO/BBTO peak couple, the solitary BTO peak is therefore assumed to originate from the enhanced occurence of continuous wurtzite domains within the nanowire. The wavenumber of the BTO corresponds reasonably well to the expected position of the wurtzite Raman peak.

3.4.4 Enhanced Raman scattering from single nanowires

The observed scattering intensity of a single nanowire cannot be explained by good growth morphology alone, since the scattering intensity of the nanowires even exceeds that of bulk GaAs by about an order of magnitude, as will be shown in the following.

When comparing the normalized scattering intensity of figure 3.15 with figure 2.6, the bulk scattering intensity of the TO phonon mode per unit of time and mW is about a factor of 6 larger than the scattering intensity of the single HBF nanowire. However, a statement on the scattering intensity should not compare the absolute scattering intensity, but rather the scattering intensity per unit volume. In [20], the quantity of the Raman enhancement (RE) is defined as

$$RE \equiv [I_{nanowire}/V_{nanowire}]/[I_{bulk}/V_{bulk}], \tag{3.1}$$

with $I_{nanowire}$ denoting the measured Raman intensity for a single nanowire, I_{bulk} that for the bulk GaAs(111)B reference sample, and $V_{nanowire}$ and V_{bulk} denoting the volume of the single nanowire and the bulk probed, respectively.

A good first approximation to the scattering volume of the bulk material is a sphere with the diameter of the laser spot. Since the focal depth is larger than the diameter, this approximation is a lower bound to V_{bulk}. The illuminated nanowire volume is at maximum the laser spot diameter times the nanowire cross section. For the parameters used in the current experiments (d_{laser} = 640 nm, $\mathrm{d}_{nanowire}$ = 50 nm), and correcting for the different Raman scattering intensities from {110} and {111} surfaces, this leads to a Raman enhancement of RE $\approx$ 9.

When comparing this RE value with those obtained in reference [20], it is about a factor of 8 smaller than what is measured there for nanowires of a similar size and

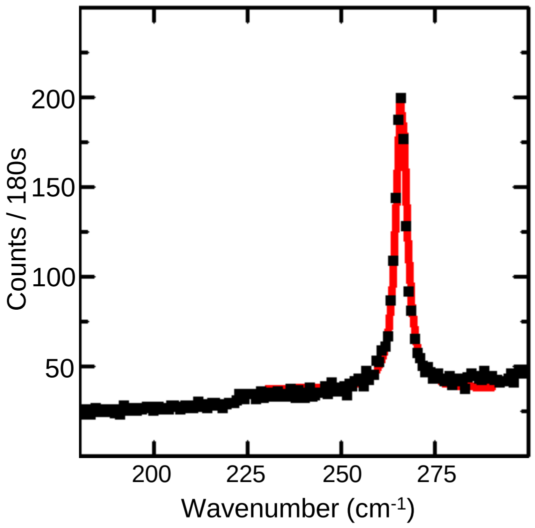

Figure 3.15: TO phonon mode measured on a single nanowire grown in HBF growth mode (HBF1). Five spectra taken at the same position are averaged. Integration time is 180 s, power used 0.35 mW. The red curve is a Lorentzian fit to the data which yields a FWHM of 3.5 cm^{-1}, which only slightly exceeds the width of the TO phonon mode measured for the bulk GaAs reference sample (3.3 cm^{-1}).

the same laser excitation energy. However, reference [20] is exclusively concerned with Si nanowires.

In literature, this enhancement effect is attributed to a dipole antenna-like resonant behavior involving incident electromagnetic radiation and the structural dielectric cross section. It is shown to depend on nanowire size as well as excitation and detection polarization [20, 21]. In our nanowires, the enhancement could also be due to a light trapping effect. The nanowires exhibit a faceted hexagonal structure which might trap the light, leading to multiple internal reflection. This would result in enhanced interaction probability of the photons with the crystal lattice and consequently to a Raman enhancement.

In order to be able to clearly distinguish between these mechanisms a systematic study on nanowires of different size and of different excitation conditions in terms of wavelength and excitation and detection polarization is necessary. Raman enhancement due to multiple scattering possibilities should essentially be independent of the size of the nanowires, the excitation and detection conditions or the wavelength of the radiation used. For enhancement due to electromagnetic resonances a strong dependence on these parameters is expected.

Another observation in this context is the lowering of the Raman intensity of the Si substrate in the vicinity of a GaAs nanowire by far more than can be explained by a geometrical shadowing of the Si substrate by the nanowire, shown in figure 3.16. The laser spot size is measured to be 640 nm. The diameter of the nanonowire is around 50 nm. Thus at most 1/10 of the laser spot is shadowed by the nanowire.

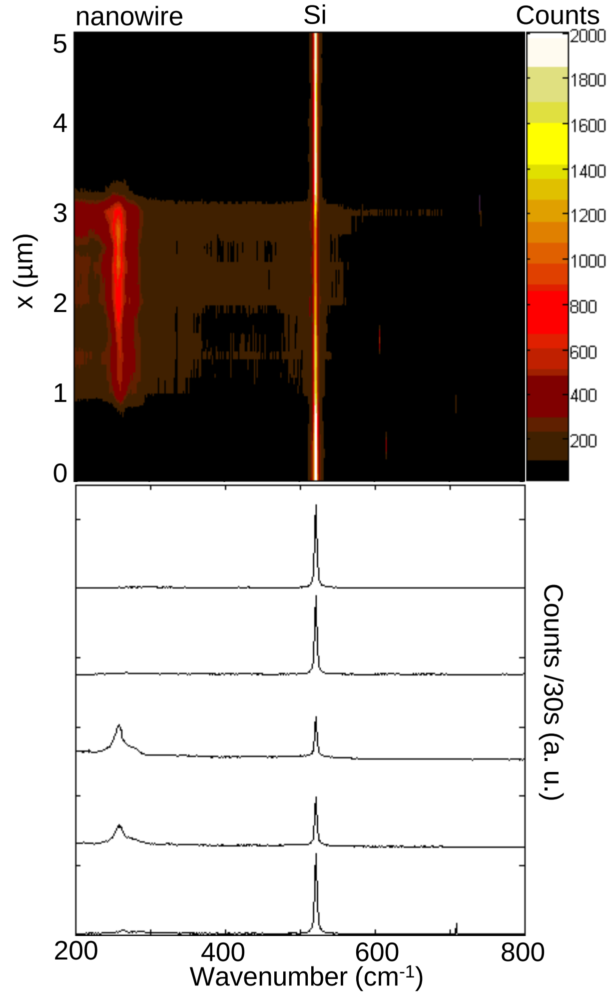

Figure 3.16: (a)1D mapping scan along the long direction of the single nanowire ULBF4, displayed in a wavenumber vs. position 2D color map. Integration time is 30 s per trace, power is 0.8 mW, step size 200 nm, polarization configuration A. (b) Waterfall plot showing one trace per micron of the mapping scan in (a). The lowering of the Si Raman signal as a response to the GaAs nanowire is clearly visible.

Part (a) of figure 3.16 shows the Raman intensity as a function of wavenumber and excitation position. The Raman signal of the single nanowire ULBF4 (at ≈ 270

cm^{-1}) is located at 1μm$\leq$x$\leq$3μm. At this position, the Raman signal of the Si substrate is reduced to less than half of its original intensity. Part (b) of figure 3.16 shows one trace per μm of the data shown in part (a) as a waterfall plot. The lowering of the Si signal as a result to the appearance of the GaAs signal is clearly visible in the second and third trace. The Si signal is not suppressed n by 10 % only, as would be expected from geometrical shadowing, but by more than 50%.
Such a behavior cannot be explained by multiple reflection in the nanowires, since this would only enlarge the nanowire Raman signal, but not lower the substrate signal by more than the geometric shadowing. Instead this observation points towards an electromagnetic origin of the Raman enhancement also in our nanowires.

3.5 Statistics of single GaAs nanowires

Linewidth

TEM measurements discussed in the previous section showed the high crystal quality for nanowires of all three growth modes. This also manifests itself in the narrow linewidth of the detected Raman signals. The narrowest linewidths observed for the TO and BTO phonon modes for nanowires grown in HBF, LBF or ULBF growth conditions are compared in figure 3.17. The FWHM of the GaAs reference sample is shown for comparison as first bar of the chart. A general trend of increasing linewidth with decreasing BEP is visible. Furthermore it is remarkable that in both nanowire growth modes where a BTO signal is visible, its linewidth is only slightly larger than that of the TO phonon mode.

Statistics on the TO peak position

Figure 3.18 shows the wavenumber difference of the TO phonon mode of all analyzed single nanowires with respect to the TO phonon mode of the GaAs (111)B reference sample. Five nanowires were measured per growth mode. The ULBF samples show the biggest standard deviation of the TO phonon mode (σ_{ULBF} = 1.4 cm^{-1}). The mean value of the ULBF TO peak of the single nanowires lies 2.5 cm^{-1} below the phonon mode of the GaAs reference sample. Comparing this value to the statistical uncertainty of the calibration measurement described in figure 3.5 of σ_{Ref} = 0.67

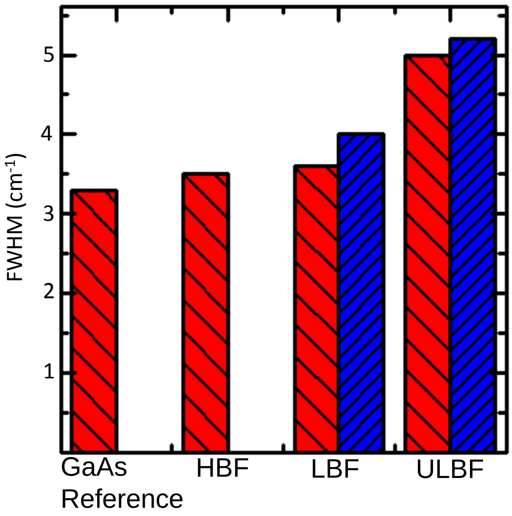

Figure 3.17: Bar chart representation of minimal FWHM for TO (red) and BTO (blue) phonon modes of nanowires of the three different growth modes. For comparison, the FWHM of the GaAs reference sample is also shown.

cm^{-1}, this shift corresponds to a lowering in wavenumber by 3.7 σ_{Ref}.

The mean value of the LBF TO phonon mode lies 1.3 cm^{-1} below the TO phonon mode of the GaAs reference sample. This corresponds to a lowering in wavenumber by 1.9 σ_{Ref}. The standard deviation calculated from the five LBF TO values is σ_{LBF} =0.7 cm^{-1}.

The mean value of the HBF TO phonon mode is almost equal to that of the LBF TO phonon mode (1.2 cm^{-1} below the TO phonon mode of the GaAs reference). The spread of the individual HBF TO phonon modes is only σ_{HBF} =0.3 cm^{-1}.

Since the shift to lower wavenumbers as compared to the GaAs reference is most prominent for ULBF nanowires that are known from TEM analysis to contain the most wurtzite parts, the shift probably originates from the influence that wurtzite bulk regions can assert on the zinc blende structure in the rest of the nanowire. Wurtzite and zinc blende have different lattice parameters, which leads to strain when both phases have an epitaxial relation.

When the single nanowire measurements are compared to the nanowire bundles, the observed shifts are found to be larger in the single nanowire case. This discrepancy is currently not understood.

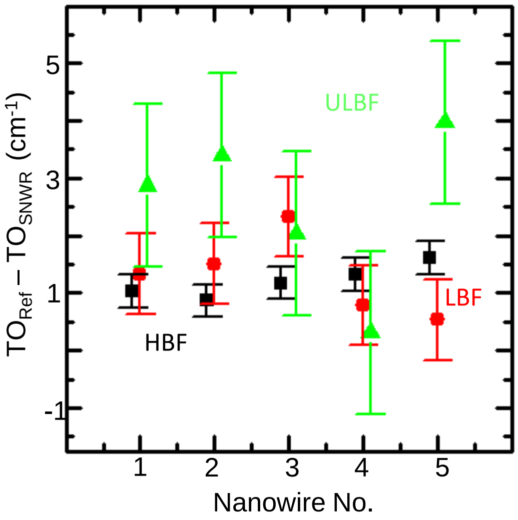

Figure 3.18: Statistic on the deviation of the TO peak position from the GaAs (111)B reference sample. Black squares represent HBF nanowires, red dots LBF nanowires and green triangles ULBF nanowires. The error bars are the standard deviation of the relative peak position in the respective growth mode. Powers used during the measurements are between 0.3 mW and 0.5 mW, a regime where heating effects are shown to not play a role (see figure 3.19).

Power dependence of a single ULBF nanowire

Since nanowires can be heated up easily due to their small size and poor thermal contact to a heat sink, a power series on a single nanowire is important to estimate which powers are still safe to use before heating-induced shifts will falsify the measurements. It is expected that the phonon modes will shift to lower wavenumbers with increased heating of the samples, as is the case in bulk material [17]. Expected shifts are in the order of up to 5 cm^{-1}. Figure 3.19 shows a power series of a single nanowire in polarization configuration B. Up to a power of 1 mW, no heat induced shift is detectable. When powers up to 4 mW are applied, both the TO (black) and the BTO (red) phonon modes shift linearly 1.5 cm^{-1} to lower wavenumbers. For powers higher than 4 mW, the BTO line is no longer clearly visible. After applying the maximal power of 8 mW, the power is reduced again to below 1 mW and the initial Raman shifts are regained (triangular markers in the figure). The lineshapes get slightly narrower (not shown in the graphs), indicating an annealing effect, similar to what is observed for nanowire bundles in figure 3.8.

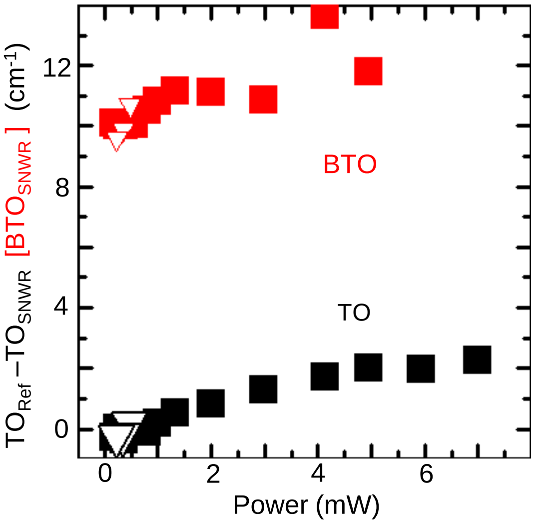

Figure 3.19: Power series of nanowire ULBF4 in polarization configuration B. Shown is the deviation of the TO phonon mode position (black symbols) and of the BTO peak position (red symbols) relative to the TO phonon mode of the GaAs reference. For powers below 1 mW, no heating effect is recognizable. When the power is increased, (square marks) both lines shift linearly downward in wavenumber in a similar way till about 2 mW. The BTO signal starts to vanish above 4 mW. For the TO phonon mode of the single nanowire, a saturation of the shift is reached at around 5 mW excitation power. When the power is reduced again to values below 1 mW, the initial Raman shifts are not only regained (triangular marks), but the modes in addition show a slight improvement in peak shape. Similar effects are also observed in ensemble measurements.

Homogeneity within a single nanowire

To gain further information about the origin of the presumably wurtzite induced shift of the zinc blende Raman signals, the evolution of the spectral position with spatial position on a single nanowire is monitored. Figure 3.20 shows the peak positions of TO and BTO phonon modes along the single nanowire ULBF2 as compared to the GaAs TO reference as a function of spatial position. It can be seen that the Raman shift of the TO phonon mode (black symbols) exhibits small variations in the order of $\approx 1\ \text{cm}^{-1}$ along the nanowire. The shift of the TO phonon mode appears larger in the region where the BTO signal (red symbols) is also visible at one end of the nanowire. Althoug at the limit of statistical significance, this finding further supports the ´proposition of the presence of wurtzite being at least partly responsible for the zinc blende TO phonon mode shift.

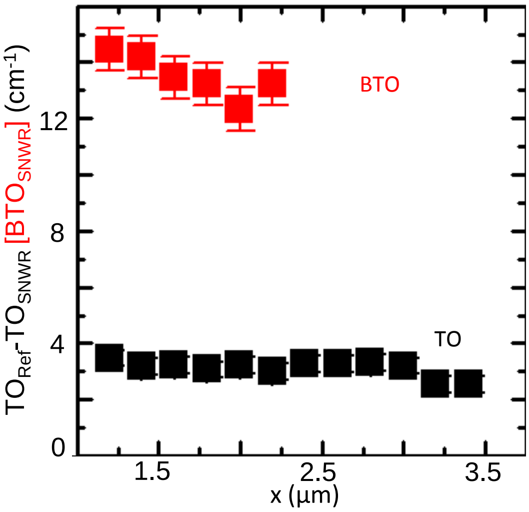

Figure 3.20: Scan along the single nanowire ULBF2 measured in polarization geometry B. Plotted is the difference in wavenumber of the TO phonon mode (black) and the BTO Raman feature (red) of the single nanowire and the TO phonon mode of the GaAs reference as a function of the distance along the wire. Step size is 200 nm, power is 0.32 mW.

Statistics on the spectral position of the BTO Raman feature

The BTO peak is of special interest, since it has no analog in bulk GaAs. It is only present in some nanowires. 4 out of the 5 ULBF nanowires, all of the LBF nanowires discussed here, but none of the HBF nanowires studied show this additional Raman feature. Unless the nanowire is heat treated, the peak appears exclusively at one end of the nanowires. Furthermore, it is only visible in polarization configuration B. In figure 3.21, the difference in wavenumber of the BTO and the TO phonon mode in each of the nanowires that showed a BTO signal is plotted as a function of the nanowire index. This graph illustrates that the spectral position of the BTO relative to the TO phonon mode is rather reproducible. The mean value of $TO_{SNWR} - BTO_{SNW}$ is 10.5 cm^{-1} for the LBF and 10.7 cm^{-1} for the ULBF single nanowires, respectively. The fluctuation in the BTO peak of the LBF nanowires is significantly larger than that of the ULBF nanowires ($\sigma_{LBF} = 0.75$ cm^{-1}, $\sigma_{ULBF} = 0.3$ cm^{-1}). This can also be understood with the help of the TEM results. Since the wurtzite regions found in ULBF nanowires are in general of larger extent, the peak position more likely resembles that of real bulk wurtzite. The LBF wurtzite regions might not always be large enough, giving rise to bigger fluctuations in the detected wavenumber position of the BTO peak.

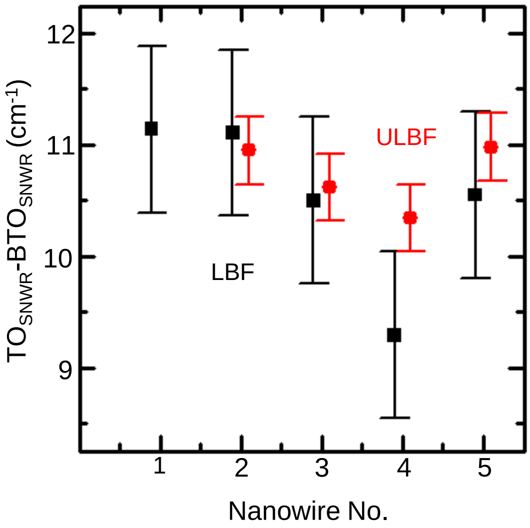

Figure 3.21: Statistics on the spectral position of the BTO Raman feature in single nanowires. Plotted is the BTO wavenumber shift relative to the TO phonon mode as a function of the nanowire index. The BTO peak is detected in 4 out of 5 nanowires grown in ULBF growth mode, in all LBF grown nanowires discussed here, but never in nanowires grown in HBF growth mode. Black squares represent LBF nanowires, red circles ULBF nanowires. The bars indicate the standard deviation, $\sigma_{LBF} = 0.75$ cm^{-1} and $\sigma_{ULBF} = 0.3$ cm^{-1}, respectively.

3.6 Summary and discussion

The correlation of growth parameters, TEM analysis and spatial resolved Raman measurements on single nanowires shows that by means of controlling the As_4 BEP in Ga assisted growth, nanowires with predefined amount of wurtzite structure can be reproducibly fabricated. The wurtzite as well as the zinc blende elements are shown to be of good crystal quality. In Raman measurements, this is reflected by a narrow FWHM of the phonon modes and intactness of selection rules over long parts of a single nanowire. The samples grown under medium arsenic pressure (LBF) show the strongest Raman signal.Although they exhibit the largest wurtzite domains, ULBF samples suffer from a larger amount of twin defects, which becomes evident in wider FWHM of the phonon modes, relaxation of selection rules and lower overall intensity.

When nanowire bundles grown in LBF or ULBF growth mode are deliberately heated by applying large laser power densities, they undergo a permanent structural change. In the Raman spectra this is seen as a general narrowing of peaks as well as the appearance of two new Raman features in the BTO and the BBTO region. These findings are explained in accordance with literature as an annealing effect of defects (lineshape narrowing) as well as As segregation at the surface of the nanowires (BTO and BBTO peak).

Spatially resolved single nanowire analysis allows to distinguish the Raman signal attributed to wurtzite from As related features. Main indications for a wurtzite origin are the narrow linewidth of the BTO signature, the absence of the second As feature in the BBTO region and the spatial localization to only those areas in the nanowires where extended wurtzite domains are identified from TEM analysis.

Furthermore, a shift to lower wavenumbers of the zinc blende TO phonon mode is observed in single nanowires, that increases with increasing wurtzite content. This finding is attributed to strain, which can be caused by the epitaxial relation of the two lattice configurations.

In addition to the intriguing interplay between wurtzite and zinc blende structure, the GaAs nanowires show other interesting features such as an enhancement of Raman efficiency by almost an order of magnitude as compared to bulk material. In accordance with literature this is attributed to antenna-like resonances of the nanowire with the electromagnetic radiation of the exciting laser field.

Of further interest is the ability to induce controlled structural change by annealing single nanowires or nanowire bundles.

The more detailed investigation of these phenomena can indeed be considered a promising field for further research.

Chapter 4

Raman spectroscopy of Si nanowires

This chapter reports on Plasma-Enhanced Chemical Vapor Deposition (PECVD) grown Si nanowires with Ga as a catalyst. The crystal lattice of the Ga catalyzed nanowires shows a large amount of twins and stacking faults along several crystallographic directions, which increases with decreasing growth temperature. While in TEM analysis the zinc blende structure is found to be the main crystallographic order all along the nanowires, in some regions nanocrystallites and nanotwinned arrays can be identified. These interesting features are probably related to the occurence of a peak at 495 cm^{-1} in the Raman spectrum.

4.1 Growth of Si nanowires

A well-established technique is the Vapor-Liquid-Solid growth mode (VLS), where size and position of the nanowires are controlled by the distribution of catalysts such as Au on the substrate surface [23]. A precursor gas (e.g. silane (SiH_4) in the case of Si nanowire growth) forms an eutectic liquid alloy at the catalyst surface. When a saturation concentration is reached, the excess silicon precipitates into a solid state silicon nanowire at the interface between the metal droplet and the substrate. The nanowire length can then be controlled by varying growth times, precursor gas pressure and/or growth temperatures. Since Au is the most efficient catalyst, very little results are currently available on other catalysts such as Ga [24]. To use Ga as a catalyst has the following advantages:

- Low melting point of Ga (30°C) which coincides with the eutectic temperature of the binary system with Si. This opens up the possibility of low-temperature growth leading to significant technological advantages.
- Low solubility of Ga in Si. The likelihood for incorporated defects with their degrading effects on optical and electronic quality of the nanowires is much lower than when Au is used as a catalyst.
- Low acceptor level of Ga only 27 meV above the valence band edge in Si. Even in case of incorporation, the carrier mobility in the nanowires would not be significantly reduced. Instead, this would only result in a slight down shift of the Fermi level towards the valence band.

The Si nanowires were synthesized by Plasma Enhanced Chemical Vapor Deposition (PECVD) in collaboration with P. Roca i Cabarrocas at the Laboratory of Interfaces and Thin Films, Ecole Polytechnique, Palaiseau, France by I. Zardo [25], who was also involved in the Raman analysis. Ga layers with a thickness of 2 nm or 5 nm, respectively, are predeposited on epiready (001) oriented GaAs wafers in a MBE system at the Walter Schottky Institute. Under UHV conditions, the sample is heated to the preset growth temperature. Prior to nanowire growth, the sample is annealed by a 5 min exposure to a hydrogen plasma to reduce the oxide on the surface of the Ga droplets, thus activating the catalyst function of Ga. While the hydrogen plasma is kept active to ensure that the surface of the gallium droplets does not re-oxidize, the precursor gas silane is introduced into the growth chamber to feed the nanowire growth. In the Raman analysis, Si nanowires grown at 500°C, 550°C and 600°C are examined. For the samples analyzed here growth time is always 45 min.

4.2 TEM analysis

Depending on the growth temperature, the nanowires are found to grow predominantly in [112] (T_{Growth} = 500 °C) or [111] (T_{Growth} = 600 °C) direction. For the intermediate growth temperature of T_{Growth} = 550 °C, a mixture of both growth directions is found.

The TEM analysis of the Ga catalyzed Si nanowires shows that these nanowires possess a rather irregular crystal structure. In general the irregularity increases with decreasing growth temperature.

These irregularity lead to several interesting features, two of which are briefly discussed in the following. A more complete discussion will be published in [26].

A large amount of twinning along several directions is observed, including twinning parallel to the growth axis. In this way, small domains called nanocrystals are defined that are bordered by twin planes running along different crystal directions. Such a region which is separated from the rest of the nanowire by twin planes is shown in figure 4.1.

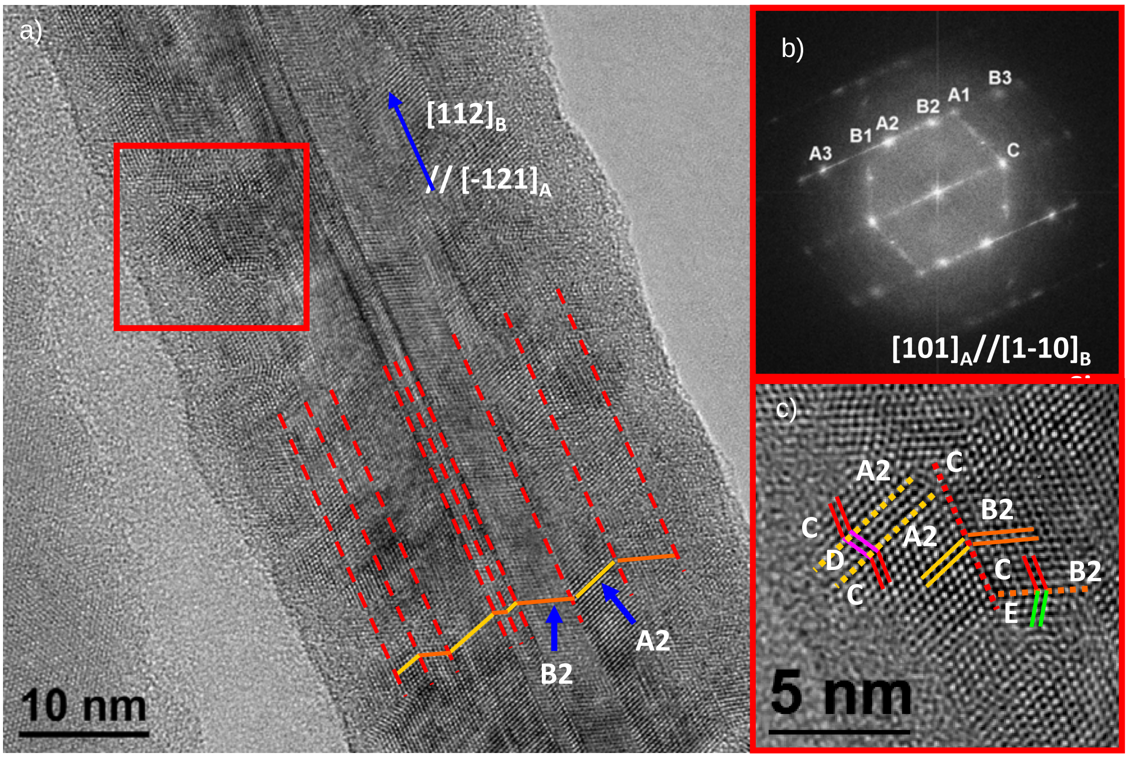

Figure 4.1: TEM image of a Ga catalyzed Si nanowire. In the overview section shown in part (a) of the figure, the general crystal quality of the nanowire is visible. Many twin defects are found, in particular a large amount of twin defects parallel to the growth direction (highlighted by red dashed lines). Twins in other direction are also observed (yellow and orange solid lines). (b) FFT spectrum of the TEM image. (c) HRTEM zoom-in into the red square shown in (a). Highlighted is the separation of small crystal segments from the crystal structure of the main nanowire by twins oriented in different crystal directions. This is believed to lead to a behavior of these nanowire areas that is similar to nanocrystals.

In some areas agglomerations of wurtzite double planes are found that are separated by periodic twins in a very regular manner. This phenomenon is called micro- or nanotwinning. If extended over a large enough area this might lead to a new superstructure within certain areas of the nanowires. An example of a nanotwinned area is shown in figure 4.2

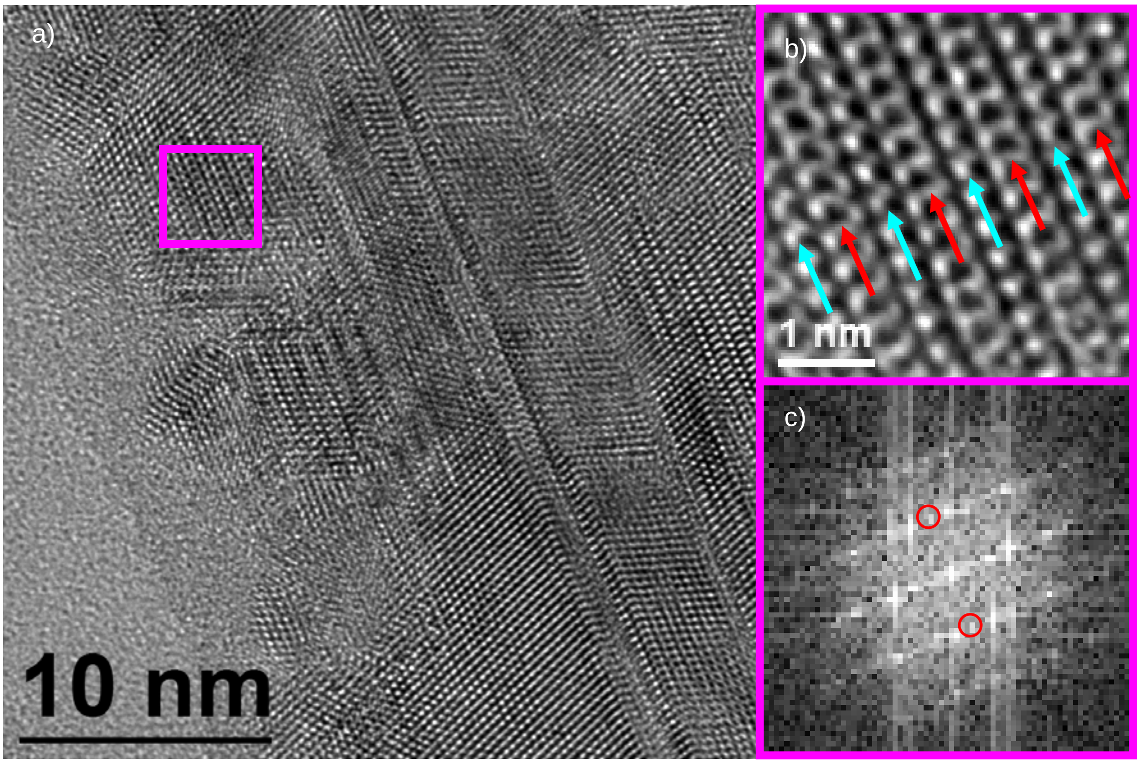

Figure 4.2: TEM image of a Ga catalyzed Si nanowire. In the overview section shown in part (a) of the figure, the general crystal quality of the nanowire is visible. Dark areas show areas of crystal orientation other than the main zinc blende structure. (b) Zoom-in on the region highlighted by the purple square. A regular pattern consisting of several repetitions of two wurtzite layers (red arrows) and one zinc blende layer (cyan arrows) becomes visible. This effect is called nanotwinng and is a common feature of in semiconductor nanowires. (c) FFT spectrum of a nanotwinned region.

4.3 Raman measurements

In the case of Si nanowires a transfer is not necessary for bundle measurements, as they are obtained on a GaAs substrate. The density of the nanowires is of the order of 50 nanowires/μm^2, which means that approximately 15 nanowires are illuminated simulataneously given a laser spot size of ≈ 640 nm.

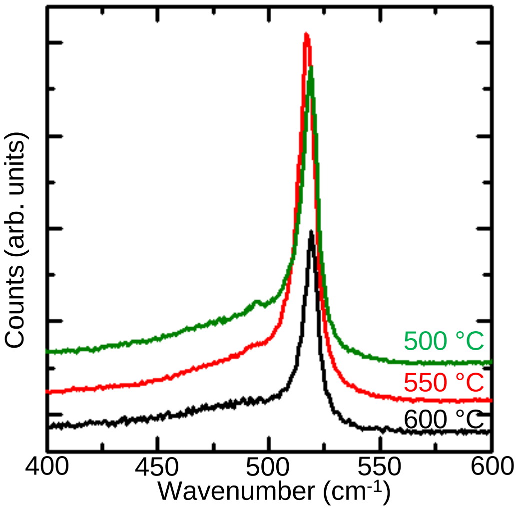

Figure 4.3: Waterfall representation of Raman spectra of Ga catalyzed Si nanowires grown at different growth temperatures. Excitation power is 0.5 mW. All three spectra show a center peak at 518 cm^{-1} with a FWHM of ≈ 8 cm^{-1}, as well as a pronounced tail to lower wavenumbers. With decreasing growth temperature, the intensity of the tail relative to the center peak increases. At the lowest growth temperature of 500°C, an additional feature at 495 cm^{-1} becomes clearly visible above the broad tail. Its onset can also be seen in the spectra of the nanowires grown at higher growth temperature. Figure adapted from [25].

In figure 4.3, typical Raman spectra are shown for all three growth temperatures in a waterfall representation. The center peak it located at 518 cm^{-1} with a FWHM of ≈ 8 cm^{-1}. This width is comparatively large and fits in well with the TEM analysis showing a large defect density for all growth temperatures. In addition to the large FWHM, three findings set the Raman spectra of the Si nanowires apart from that of bulk crystalline silicon:

- Shift of TO peak by ≈ 3 units in wavenumber to lower energy
- Pronounced tail to lower wavenumbers
- Additional weak feature at 495 cm^{-1}, feature strength dependent on growth temperature

4.4 Summary and Discussion

The Raman findings appear plausible with the TEM analysis in mind. The shift of the TO peak might be induced by confinement effects that are caused by nanocrystals in the sample [27]. The large amount of irregularity can be held responsible for the pronounced tail to lower wavenumbers, which in literature is attributed to the presence of amorphous material [28]. The additional weak feature at 495 cm^{-1} is in general believed to originate from a few monolayers of wurtzite that are for example present at twin boundaries [28]. The fact that this peak is best visible at the lowest growth temperature where the effect of nanotwinning is found to be most pronounced in the TEM study further supports this interpretation. A large and regular superlattice structure in major parts of the nanowire should lead to additional superlattice-induced Raman features similar to those described for GaAs/AlAs superlattices, for example in [15]. However such features are not observed in the spectra presented.

The growth study of Ga catalyzed Si nanowires is just at the beginning. However, the features established in the present work of nanotwinning and nanocrystal formation might be powerful tools for nanofabrication if their extent and structure can be well controlled.

Chapter 5

Optical properties of low-dimensional semiconductor heterostructures

In this chapter, first the theoretical basis of photoluminescence is briefly introduced, followed by a description of the experimental tools for spatially resolved photoluminescence measurements on semiconductor nanostructures.

5.1 Photoluminescence in semiconductors

This section gives a brief overview of the physical processes that lead to the photoluminescence (PL) response observed in the low-dimensional heterostructures analyzed in this thesis.

The following processes are involved in optical transitions of direct semiconductors:

- Absorption. Light quanta with energies higher than the band gap are absorbed and electrons are excited from the valence band into the conduction band. Simultaneously a hole state in the valence band is created.
- Relaxation. The electrons and holes relax to the band edges by scattering with phonons and other electrons.
- Coulomb-Interaction. Due to the opposite charge of electron and hole a bound state with energy slightly lower than the band gap can be created. This bound state is called an exciton.

- Recombination. The electron-hole pair recombines by sending out a photon. This process is called photoluminescence.

For the PL process, the transition probability $w(E)$ can be calculated with Fermi´s Golden rule to be

$$w(E) = \frac{2\pi}{\hbar} \left| M \right|^2 \rho_f(E), \tag{5.1}$$

with M being the transition matrix element (deduced from the hamiltonian of the interaction between the electric field and the semiconductor lattice) and ρ_f(E) the density of unoccupied final states at energy E.

If the carrier motion in a solid is limited to a layer of a thickness of the order of the carrier de Broglie wavelength, size quantization effects will occur. In semiconductor heterostructures such confinement effects can be introduced by employing materials with different band gaps, for example by embedding a GaAs layer in between two AlGaAs layers. In this way, electrons as well as holes are restricted in their motion in growth direction.

When the dimensionality of the semiconductor structure is reduced, the transition probabilities are altered, since the transition matrix element M as well as the density of states ρ_f(E) depend on the dimension and geometry of the probed semiconductor structure.

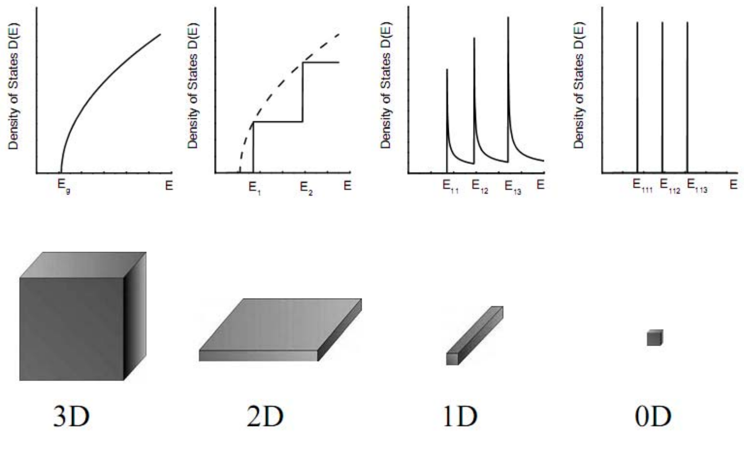

Figure 5.1: Density of states for structures of different dimensionality. Adapted from [4].

In figure 5.1 the density of states is schematically shown for 3D, 2D, 1D and 0D systems. While for 3D the density of states shows a $\sqrt{E}$ dependence, in the 2D case, every subband gives a constant contribution, which leads to a step-like distribution of the density of states. In the 1D case, singularities at the band edges become visible. The 0D state exhibits a delta-like density of states. The entire oscillator strength is concentrated in discrete energy levels. This property leads to the comparison of 0D states in semiconductors with atoms. Like in the atomic example, only quantized energies can be absorbed or emitted. This is why 0D states in semiconductors are also called Quantum Dots (QDs). Unlike their atomic counterparts, QDs are embedded in a 3D semiconductor matrix and are thus easier accessible to manipulation techniques. This makes them promising candidates for the realization of devices in the context of Quantum Information and Quantum Computation.

5.2 Confinement effects in Cleaved Edge Overgrowth structures

The low dimensional heterostructures examined in this thesis are produced by a growth technique called 2fold Cleaved Edge Overgrowth (CEO). In this technique, three perpendicular Quantum Wells (QWs) are grown. QWs themselves are 2D objects. At the intersection of two QWs, a 1D structure called a Quantum Wire (QWR) is created. Three crossing QWs define a 0D state, the QD. While the specific growth procedure is described in detail in the experimental section, here the physical origin for the formation of low dimensional states with this technique is sketched.

The confinement effect in the CEO structures is of quantum mechanical nature. The simplest example of quantum confinement is the particle in a potential well. As a result of the confinement, the energetic ground state of the particle is not the bottom of the well, but some energy E_0, whose difference to the bottom of the well depends on the well geometry.

In particular, the ground state energy is lowered when the potential well thickness is increased. In semiconductor physics, a similar behavior is observed for excitons in a QW. Figure 5.2 shows the lowering of PL energy as the well thickness is increased. The physical reason for this effect is the increase in space that the wave function

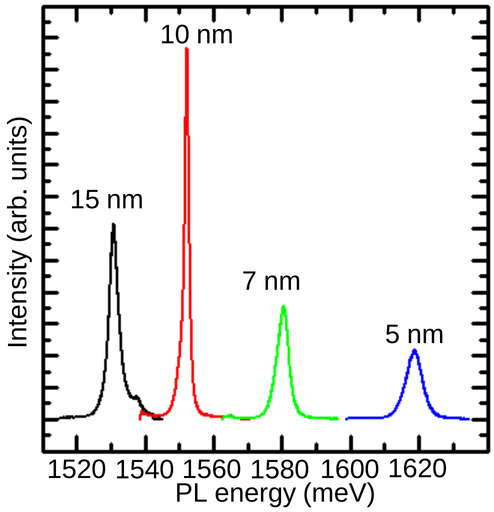

Figure 5.2: PL intensity of four different GaAs QWs embedded in an $Al_{0.3}Ga_{0.7}As$ matrix, plotted as a function of the PL energy. The QW thickness is indicated above each PL signal.

can occupy. In the limit of infinite extent of the QW, the confinement is reduced to zero, the luminescence is that of a bulk semiconductor. In the other extreme of the confining well being smaller than a certain threshold value, the bound state energy converges towards the energy of the barrier. In the CEO process, the wave function of the exciton formed by one electron and one hole can increase its volume by being located at the crossing of two QWs. Consequently its ground state energy is reduced and it will remain in this 1D lower-energy state. In the case of 2fold CEO, a further increase in volume is offered at the crossing of three QWRs. There, a 0D QD state is formed whose ground state energy is further lowered with respect to the QWR state.

In the case of 2fold CEO the exciton binding energy is of the same order of magnitude as the energetic lowering due to the geometric confinement effects described above. This makes numerical calculations of 2fold CEO confinement energies difficult, since standard approximation methods that either treat the exciton binding energy or the confinement as a small perturbation cannot be applied [34].

5.3 Micro-Photoluminescence spectroscopy techniques

For PL measurements on GaAs CEO QDs, the sample has to be kept close to liquid ^{4}He base temperature, since thermal excitation of the excitonic states of the quantum dots would obscure the quantum phenomena that this research is aimed at. At the same time, mechanical positioning accuracy and long-term stability better than 1 μm are required for spatially resolved measurements. This can be achieved by an evacuated sample stick equipped with low-temperature slip-stick piezo elements that is immersed in liquid He [40, 41]. Alternatively, the sample can be kept in a fixed continuous-flow cryostat, while the micro-positioning is done by moving the excitation and detection beam with respect to the sample. Both setups described in the following use the latter approach.

5.3.1 Raman detection unit

The Raman detection unit comprising the Dilor XY spectrometer and Wright CCD camera introduced in section 2.4 can also be used for the recording of PL signals. This is mainly of interest because of the good spectral resolution provided by the Dilor XY (see figure 2.7). However, the PL signals of the CEO 2D and 1D nanostructures are at the very end of the spectral range of this detection unit, thus suffering from substantially decreased quantum efficiency in that range (spectrometer gratings are blazed at 500 nm). QD signals that are further lowered in energy are even beyond the spectral range of the Dilor XY in the present grating configuration. Nevertheless the Raman detection unit is still useful for precharacterization of the CEO samples. In figure 5.3 the setup constructed in the scope of this thesis for scanning micro-Photoluminescence (μPL) experiments is sketched.

This design operates with the minimal amount of optical elements necessary. Between excitation outcoupling and detection incoupling, the light has to pass only two beamsplitters and one objective. In particular, no mirrors are necessary.

Apart from being confocal due to the use of single mode fibers in detection as well as illumination, this compact design has the further advantage that the excitation and detection paths are completely reversible, while the sample is in view of the

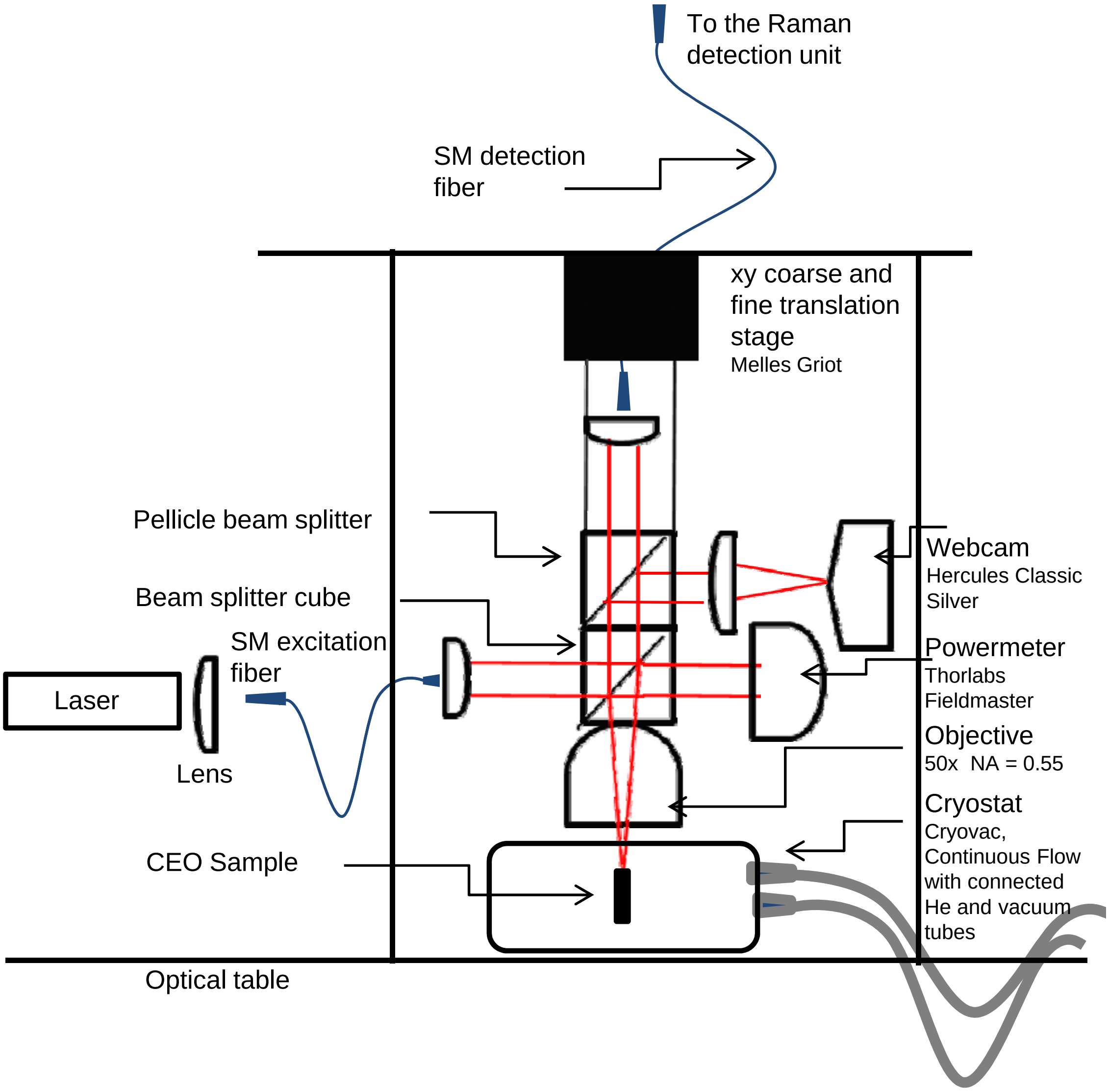

Figure 5.3: Overview of μPL setup with the Raman detection unit. Light emitted by the laser source (left) is coupled into a single mode fiber. The fiber guides the light to the movable illumination and collection unit (center). This unit comprises two beamsplitters, an objective, a power meter head, a Web cam and in- and outcoupling devices for single mode fibers. For xy mapping scans the unit is moved as a whole by the piezo-driven fine translation state (top). The sample is positioned in a He flow cryostat that is fixed on the optical table.

Web cam at all times. In this way it is possible to couple an alignment laser from the detection side into the illumination and collection unit. This ensures optimal alignment of the detection path for the wavelength of the expected PL signal.

Only in a confocal setup is the detection spot size equal to the excitation spot size. In all other configuration, the detection area size is larger than the excitation spot size. Therefore a confocal setup is of particular importance when the drift of carriers is an issue. This is the case for CEO samples and will be further discussed in chapter 6.

5.3.2 Near-IR detection unit

For recording PL $\gtrsim$ 800 nm, a micro-PL setup with a detection unit providing an approximately 100-fold increase in quantum efficiency for near-IR light was temporarily available during the last month of measurements for this thesis. A sketch of the setup beam line is shown in figure 5.4. Compared to the setup described in section 5.3.1 the excitation and detection unit is less compact. Only the objective is movable by the piezos, all other optical elements such as beamsplitters, translation mirrors and fiber couplers are fixed on the optical table, as is the cryostat. This keeps the setup more flexible for different kinds of applications than the compact μPL scanning unit presented in section 5.3.1. However, it is also harder to align since the possibility of reversing excitation and detection path is not readily given and two additional translation mirrors have to be used. This setup also offers the possibility for time-resolved measurements. To that end, PL is excited by a pulsed diode laser and detected with a silicon avalanche diode. With the exception of the field-effect structure, all graphs discussed in chapter 6 were recorded at this setup, since only this detection unit could detect in the wavelength range of the 2fold CEO QD PL signal.

The key parameters of the setup are an excitation spot diameter of about 1.4 μm, spectral resolution of 180 μeV (using a grating with 1200 grooves/mm) and temporal resolution of $\approx$ 100 ps.

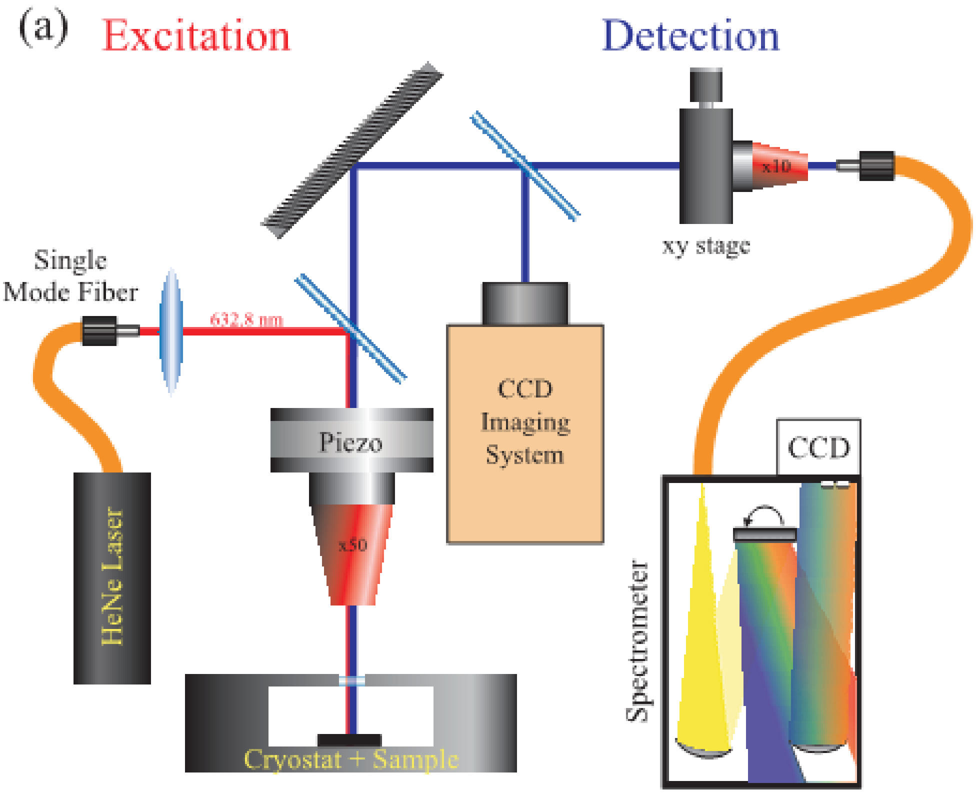

Figure 5.4: μPL setup with near-IR detection unit. Excitation light is shown in red, detection light in blue. A HeNe or an alternative laser source is coupled into a single mode fiber (left). The decoupling of the excitation and detection path is achieved using a pellicle beam splitter. The microscope objective is mounted on an xyz piezo (center). On the detection side, the light is deflected by a mirror and can either be directed by a flipper mirror to a CCD observation camera or through a multi mode fiber to the detection unit (Spectrometer Triax 550 and Si CCD: Jobin Yvon). Adapted from [42].

Chapter 6

Cleaved Edge Overgrowth nanostructures

The subject of this chapter is the fabrication of low-dimensional nanostructures grown by the Cleaved Edge Overgrowth (CEO) technique and their characterization by spatially resolved optical spectroscopy. At the intersection of two perpendicular Quantum Wells (QWs), a Quantum Wire (QWR) is formed. Three crossing QWRs define a Quantum Dot (QD). This technique provides precise control over size, shape and location of low-dimensional nanostructures so far unique in the quantum dot community, thus making it particularly interesting for fundamental studies on single and coupled QDs [29]. Based on the pioneering work of G. Schedelbeck on this subject 10 years ago at the Walter Schottky Institute [30], the fabrication procedure is adapted to exploit technological advances in semiconductor fabrication. As a result deeper confinement energies and good reproducibility of quantum dot emission energies are attained. Multi-exciton occupation is explored in power-dependent measurements. For further characterization, the dynamics of CEO nanostructures are investigated using time-resolved techniques. Finally the possibility to electrically tune the CEO QD structures is examined.

6.1 Fabrication of quantum dots by Cleaved Edge Overgrowth

The growth on cleaved crystal facets is based on the property of AlGaAs/GaAs crystals to easily cleave perpendicular to the [110] growth direction atomically smooth over macroscopic distances. It was first realized by L. Pfeiffer and coworkers in 1990 [31]. CEO allows the fabrication of one- and zero-dimensional structures with MBE precision. The procedure is schematically illustrated in figure 6.1. In the first growth step in [001] direction a multilayer structure is grown on a 2-inch substrate wafer. To prepare the next growth steps in the [110] and $[\bar{1}10]$ growth directions, the wafer is cut into 7 x 7 mm^2 pieces. These pieces are each scribed by a micro scriber once for each cleavage process to set predetermined breaking points for the forthcoming cleaves. Then they are mounted vertically in special MBE holders such that the mechanical cleavage bar inside the MBE system can touch the sample ends and cause them to cleave atomically smooth starting at the predetermined breaking points. Immediately after the cleave, the surface is overgrown with a multilayer structure. To prepare for the next CEO step, the samples are taken out of the MBE chamber and turned by hand by 90°. The cleavage and overgrowth procedure is repeated once more. The final twofold overgrown samples have a dimension of 3.3 x 3.3 x 0.15 mm^3 with the CEO QD being located within a few hundred nanometers of the surface of the overgrown corner. The detailed layer structures for QDs and coupled QD structures examined in this thesis are described in the following sections.

A difficult aspect of this technique lies in the perfect cleavage of the samples. For this, the samples have to be as thin as possible to facilitate the in-situ cleavage. On the other hand, they still have to be handled by the experimentalist. Until very recently, the only available technique for achieving thin samples was to mechano-chemically thin each substrate wafer after the first growth step from 350 μm initial thickness down to 80-120 μm. This process is described in detail in [32]. The thinning process can have the side effect that strain is introduced into the material [33]. Furthermore, the surface thickness varies by about 10 to 20% across the wafer surface. Mechanical strain as well as varying surface thickness influence the reproducibility of the growth process.

Therefore, a new method is introduced in the scope of this thesis. Since the semicon-

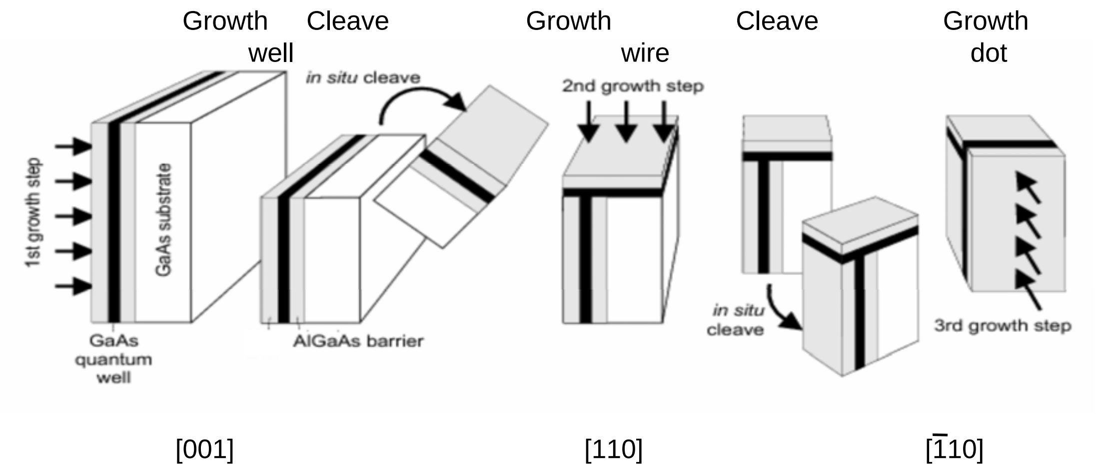

Figure 6.1: Schematic of the 2fold CEO process to grow atomically tailored QDs. In each growth step the dimensionality of the resulting structure is reduced due to quantum mechanical confinement effects.

ductor industry today is able to provide significantly thinner substrates than 350 μm, the substrate growth is now performed on an already 150 μm thin substrate (AXT Semiconductors). This thickness proved to be well-cleavable and well-manageable at the same time. However, depending on their substrate holder mechanism, not all MBE machines in the Walter Schottky Institute can grow on thin substrates. Therefore, the first growth step for the samples described in the following chapter is performed in a MBE machine different from that employed for the CEO steps. Apart from the actual growing, the remaining handling steps for the preparation of CEO samples are therefore reduced to the micro scribing and cutting process to facilitate the cleave (see also [30]). A substantial improvement is the uniform thickness of the substrate.

6.2 Micro-Photoluminescence spectroscopy

The definition of CEO quantum dots at the crossing of three quantum wells implies, that the position of the low-dimensional CEO structures on the overgrown corner is precisely known. Together with the spectral information, the spatial distribution of the photoluminescence response is therefore an important guideline to the interpretation of the photoluminescence response of the sample. After an introduction to the sample structure, characterization by 1D and 2D micro-Photoluminescence (μPL) mapping scans is shown in subsection 6.2.2. The specific PL lines in the measured spectra are attributed to 2D-QW, 1D-QWR or 0D-QD structures that are generated in the 2fold CEO growth process. Power dependent measurements can give further hints to the origin of specific lines. They are discussed in subsection 6.2.3. Finally the possibility to electrically tune the CEO QD structures is examined in subsection 6.3. The experimental results of μPL measurements on CEO nanostructures are reviewed and discussed in subsection 6.4.

6.2.1 Introduction to the sample structure

Six different samples that are fabricated according to an identical growth protocol are analyzed by 2D mapping scans. According to the name of the MBE CEO holder used during the second and third growth step they are referred to as Ta3b, Ta3c Ta3d, Ta6a, Ta6b, and Ta6c.
A sketch of the sample structure is shown in figure 6.2.

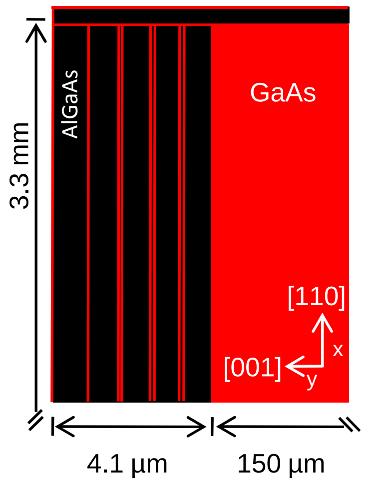

Figure 6.2: Sketch of 2fold CEO sample structure as seen after the second cleavage, but before the third growth step. GaAs is depicted in red, AlGaAs is shown in black. The QW pattern of single and double QWs in [001] growth direction is visible, as well as the crossing of the [001] and [110] QWs.

The [001] growth consists of three double quantum well structures and one single quantum well, each 7 nm wide. The double quantum wells are separated by 60 nm, 30 nm and 15 nm wide $Al_{0.3}Ga_{0.7}As$ barriers, respectively. Each quantum well structure is framed by 30 nm wide $Al_{0.3}Ga_{0.7}As$ barriers. A superlattice structure (8nm $Al_{0.3}Ga_{0.7}As$, 2nm GaAs) of 700 nm width is introduced in between the framing $Al_{0.3}Ga_{0.7}As$ barriers. The growth is terminated by a 10 nm thick GaAs capping layer. The total overgrown $Al_{0.3}Ga_{0.7}As$/GaAs structure in [001] direction is 4.1 μm thick.

In the second growth step in [110] direction, the structure is overgrown with 7nm GaAs immediately after an in situ cleavage process exposes an atomically smooth and clean surface. The QW growth is followed by 30 nm $Al_{0.3}Ga_{0.7}As$ and a 300 nm $Al_{0.3}Ga_{0.7}As$/GaAs superlattice. The growth is capped by 10 nm GaAs.

The third growth procedure in [$\bar{1}$10] direction likewise consists of an in situ cleave, a 7 nm GaAs quantum well, a 30 nm $Al_{0.3}Ga_{0.7}As$ framing barrier and a 10 nm GaAs capping layer.

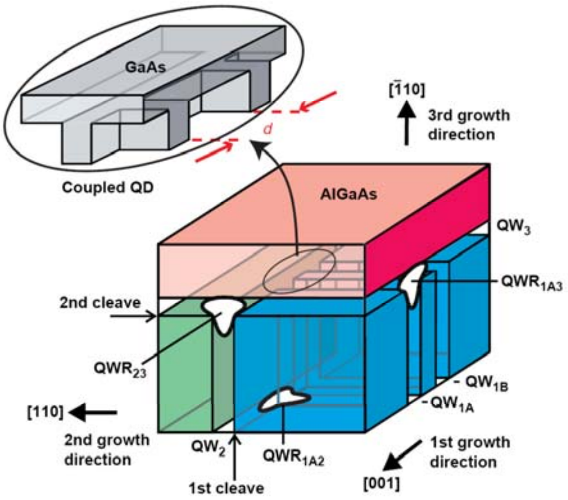

Figure 6.3: Sketch of a 2fold CEO QD pair and the underlying QWRs and QWs. Material deposited in the first growth step is shaded in blue, material deposited in the second growth step is shaded in green and material deposited in the third growth step is shaded in red. The CEO-related nanostructures are identified by a nomenclature following the growth steps they are created in, for example QWR_{23} specifies the QWR that is created by the crossing of a QW in the second and a QW in the third growth direction. This nomenclature will be followed throughout this chapter. The inset shows the geometry of a QD pair, whose [001] QWs are grown a distance d apart. Adapted from [29].

In sketch 6.3, the structure of a 2fold CEO QD pair is visualized. All the low-dimensional nanostructures that are created on the way are also indicated. The nomenclature follows the growth procedure, for example, QWR_{23} specifies the QWR that is created by the crossing of a QW in the second and a QW in the third growth direction.

In the present sample design, QWs leading to three QD pairs and one single QD are grown, see figure 6.2. This design aims at exploring the coupling mechanism of quantum dots by varying their different internal coupling strength through change of distance in [001] growth direction. It closely follows a design first realized by G. Schedelbeck [29]. By scanning along the [001] growth direction from vacuum to the sample bulk, the laser spot subsequently illuminates first the single quantum dot structure, then the closest spaced pair (inter-dot distance: 15 nm), the medium spaced pair (inter-dot distance: 30 nm) and finally the 60 nm spaced pair. Since the superlattice structure in between the pairs is 700 nm wide, it should be possible to distinguish the individual pairs with the given laser spot size of 1.4 μm. This illumination geometry requires vertical mounting of the sample, so that either the [110] or the [$\bar{1}$10] growth direction are facing the laser excitation.

As an overview, figure 6.4 shows a typical PL spectrum of a sample with the above described structure. The spectrum is recorded at the overgrown corner. On the basis of the later described mapping scans, the PL features are attributed to (from high to low energy): QW_2 and QW_3 (grey), QW_1 (violet), QWR_{12}, QWR_{13} and QWR_{23} (red), QWR_{loc} i.e. localized states in the QWRs (green), QD ground state (blue). The QD ground state is singled out by its narrow linewidth.

The localization energy of the CEO QD $E_{loc,QD}$ is defined as [36]

$$E_{loc,QD} = E_{QWR} - E_{QD}, \tag{6.1}$$

with E_{QWR} being the ground state energy of the QWR and E_{QD} the ground state energy of the QD. In the spectrum shown in figure 6.4, the localization energy of the 2fold CEO QD is found to be $E_{loc,QD} \approx 1562$ meV - 1541 meV = 21 meV.

In the following, 2D scans on three samples are discussed in detail. Ta3d is illuminated from the [110] growth direction, while the two other samples discussed, Ta3b and Ta3c, are both illuminated from the [$\bar{1}$10] growth direction.

If not stated otherwise, the PL is excited by a HeNe laser ($\lambda_{ex} = 633$ nm, continuous wave). The measurements are performed in a helium flow cryostat at temperatures

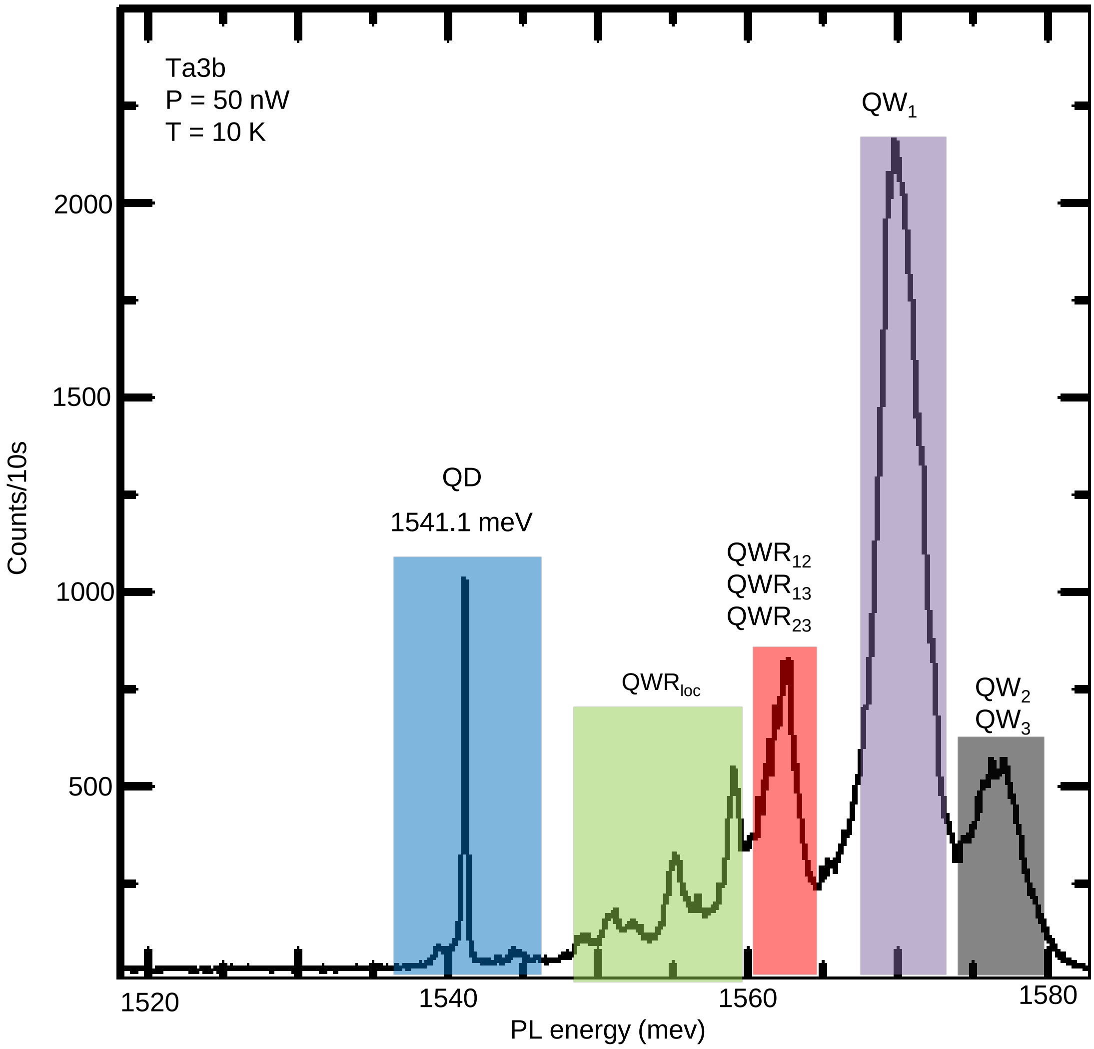

Figure 6.4: Overview spectrum of PL recorded at the overgrown corner of a CEO sample. As marked in the figure, the PL features are attributed to (from high to low energy): QW_2 and QW_3; QW_1; QWR_{12}, QWR_{13} and QWR_{23}; QWR_{loc}; QD ground state. The QD ground state is singled out by its narrow linewidth.

of ≈ 10 K.

6.2.2 2D and 1D mapping scans

Ta3b: 2D scan at low excitation power, illuminated from the $[\bar{1}10]$ growth direction

Figure 6.5 shows a 2D mapping scan of the overgrown corner of sample Ta3b. The sample is illuminated from the third growth direction with an excitation power of 50 nW. To illustrate the spatial mapping, three exemplary 2D color maps are shown in the top row, where lighter colors indicate higher values of the logarithm of the integrated PL intensity.

Graph (a) shows the spatial extent of the luminescence of the QD ground state shown in figure 6.4. The interval the PL intensity is integrated over ranges from 1541.0 to 1541.2 meV. The quantum dot luminescence is shown to be limited to a 2 x 2 μm^2 area.

Graph (b) shows the spatial extent of the luminescence in the interval from 1554.9 to 1555.1 meV. While being maximal at the sample corner, luminescence in that energy interval is also visible in other areas of the sample. This is the expected spatial distribution for QWR-related luminescence: at the sample corner, all three QWRs are illuminated at the same time, therefore the PL signal related QWRs should be most intense. Along the edges of the overgrown corner, only QWR$_{12}$ (along the [001] edge) or QWR$_{13}$ (along the [110] edge) are illuminated, therefore the signal is less intense, but still visible. However, the possibility that these states are 1D QWR states is ruled out by power dependent measurements as well as lifetime measurements presented in later subsections. Furthermore, as is shown in the spectra discussed below, the peak structure in this energy interval is very irregular and differs strongly from position to position. Therefore, this luminescence is most likely due to localized states within all three types of QWRs. These states form due to monolayer fluctuation within one of the QWs constituting the QWRs. The fluctuations are of the order of 1 to 100 nm in height and lead to randomly distributed areas of zero-dimensional confinement along the QWRs. They are investigated in greater detail in [37]. It is also possible, that some of the PL resonances observed in the interval attributed to QWR$_{loc}$ originate from charged or excited states of the

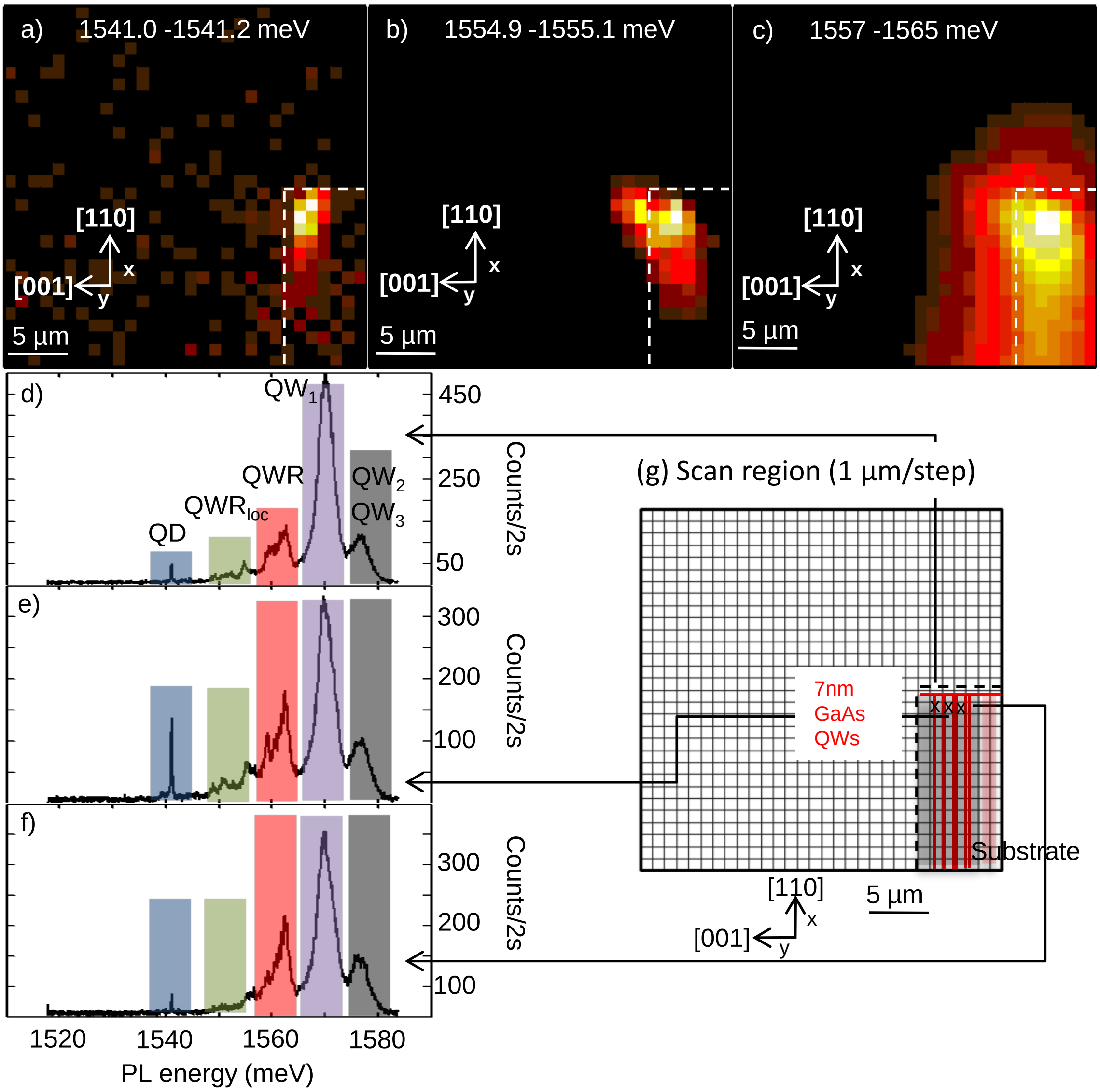

Figure 6.5: Top row (graphs (a) to (c)): 2D μPL mapping scan of the corner of the CEO sample Ta3d, mounted with the $[\bar{1}10]$ growth direction facing the laser excitation. Color-coded is the logarithm of the integrated PL intensity in the interval given at the top of each graph. The step size in each direction is 1 μm. Dashed white lines indicate the overgrown sample corner. Left side (graphs (d) to (f)): PL intensity versus PL energy representation of μPL spectra taken during the 2D mapping scan at specific locations indicated in the overview of the scan region (g). Colored bars mark spectral regions belonging to specific CEO related nanostructures (discussed in the text). Right side (g): Overview of scan region. The approximate position of the QWs as viewed from the third growth direction is indicated by red lines. Dashed lines mark the sample corner. The scale is identical to the mapping scans (a) to (c).

2fold CEO QD. However, from the present status of available experimental data it is not possible to clearly separate such a contribution from the randomly localized states within the QWRs, which have very similar properties. Vice versa, even if the CEO QD was contributing to some of the resonances in the interval QWR_{loc}, the main contribution certainly comes from localized states within the QWRs. The designation of the luminescence in this interval as QWR_{loc} therefore seems the most consistent description possible and will be followed throughout this chapter.

Graph (c) shows the luminescence in the energy interval from 1557 to 1565 meV. This luminescence is attributed to shallow QWR bound states and QWR luminescence of all three QWR types (QWR_{12},QWR_{13} and QWR_{23}). The maximum of the integrated PL intensity is located at the top of the sample edge, coinciding with the position of maximal intensity of the deeper localized QWR states shown in graph (b). Contrary to graphs (a) and (b), the QWR luminescence is visible everywhere where the sample is structured by QWs. In the region towards the GaAs bulk (right hand side of scan region) where no QWRs are located, the intensity of the luminescence can be seen to decrease.

The three spectra (d) to (f) are recorded at 1 μm displacement along the top edge of the sample (precise positions marked in the overview of the scan region (g)).

The intensity of the QD signal (blue shaded interval) is tripled by stepping 1 μm from (d) to (e). After stepping 1 μm further to spectrum (f), the QD luminescence is again reduced to approximately the initial intensity it has in graph (d). This hints at the good localization of the QD luminescence. A better estimate of the extent of this luminescence can be deduced from the analysis of a 1D scan performed with finer step width (200 nm) discussed further below.

The luminescence of the QWRs and the localized QWR states QWR_{loc} (red and green shaded intervals) is neither homogeneous in the three spectra, nor does it show any systematic decrease or increase with position as does the QD signal. This underpins the interpretation that the multitude of sharp peaks that are occasionally visible in this interval originate from localized QWR states. Due to their origin at random monolayer fluctuation, their position as well as their localization energy with respect to the QWRs are not predetermined.

Ta3d: 2D scan at high excitation power, illuminated from the [110] growth direction

Figure 6.6 has the same layout as figure 6.5. Excitation power is 1 μW, illumination direction is the second growth direction.

Graph (a) shows the color coded logarithm of integrated PL intensity over the interval from 1541.3 to 1541.5 meV. The maximal intensity is located at the sample corner and extends about 5 μm in both x- and y-direction. This shows that the spatial resolution is only about half as good as in the low-power scan performed on Ta3b. This difference is attributed to the difference in excitation power.

Graph (b) shows the color-coded integrated PL intensity as a function of x- and y-position on the sample in the spectral region between 1579 and 1586 meV. Here, the maximal integrated intensity is located above the sample corner. This is interpreted as luminescence from QW$_3$, which is visible to the side of the sample if the laser beam is not aligned perfectly straight. The weaker but continuous signal along the [$\bar{1}$10] edge of the sample can be interpreted as originating from QW$_2$, which covers the entire sample surface, but is only luminescing in the region where it is sandwiched between two AlGaAs barriers.

The luminescing area of QW$_2$ is larger than expected from geometric considerations alone. From the 4.1 μm of overgrown AlGaAs/GaAs layers and taking the laser spot diameter of 1.4 μm into account, the width of the luminescing stripe should be at most 6 μm. However, graph (b) shows luminescence along a stripe that is more than 8 μm wide. Due to the setup not being wave-optically confocal (use of multi-mode detection, see chapter 5) the detection spot is larger than the excitation spot. It can therefore be inferred that the electrons and holes generated in the semiconductor can drift several μm in order to recombine in energetically more favorable structures such as energetically lower quantum wells, wires or dots.

Graph (c) shows the integrated intensity recorded during the 2D mapping scan in the spectral region from 1517 to 1525 meV. As expected, the illuminated area is almost complementary to the region of quantum well luminescence shown in graph (b).

In graphs (d) to (e) spectra taken from different excitation positions are shown. The exact positions are indicated in the overview over the scan region (g).

Spectrum (d) is recorded at the overgrown corner. It shows the same PL features

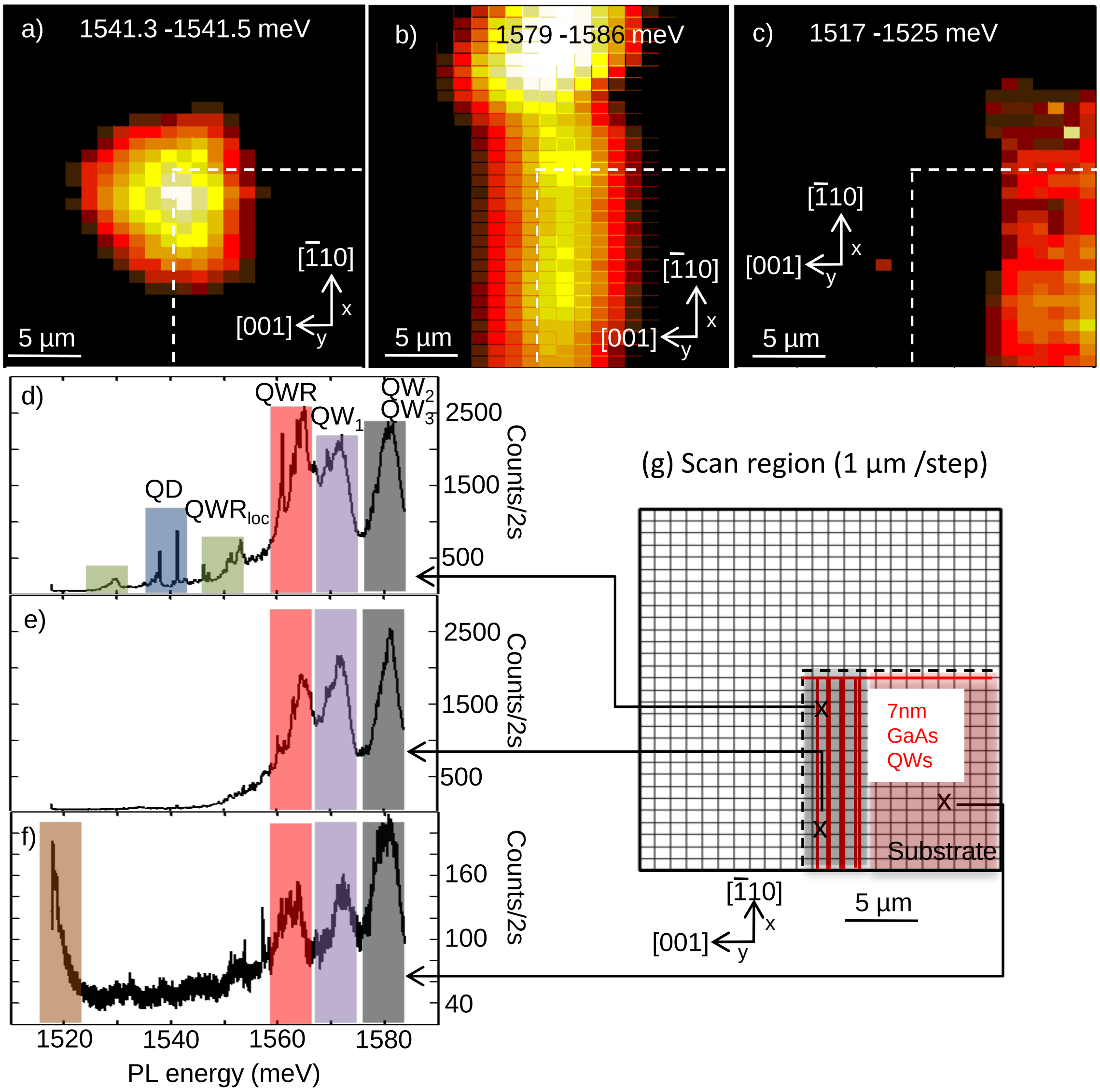

Figure 6.6: Top row (graphs (a) to (c)): 2D μPL mapping scan of the corner of the CEO sample Ta3d, mounted with the [110] growth direction facing the laser excitation. Color-coded is the logarithm of the integrated PL intensity in the interval given at the top of each graph. The step size in each direction is 1 μm. Dashed white lines indicate the overgrown sample corner. Left side (graphs (d) to (f)): PL intensity versus PL energy representation of μPL spectra taken during the 2D mapping scan at specific locations indicated in the overview of the scan region (g). Colored bars mark spectral regions belonging to specific CEO related nanostructures (discussed in the text). Right side (g): Overview of scan region. The approximate position of the QWs as viewed from the second growth direction is indicated by red lines. Dashed lines mark the sample corner. The scale is identical to the mapping scans (a) to (c).

that are introduced in figure 6.4. The main difference is the presence of two sharp lines in the QD ground state energy region. In addition a broad and weak feature energetically below the quantum dot region, is observed (lower green shaded area). Its origin cannot be clearly identified. Since this feature is not observed in the low-power scan on Ta3b, its origin is assumed to be related to the high excitation power used in the present scan.

In spectrum (e) the QD ground state luminescence has completely disappeared, since the excitation spot has moved away from the corner along the $[\bar{1}10]$ edge. As the excitation is still on the QW region, QW and QWR features are visible.

Spectrum (f) shows the high-energy tail of the luminescence of GaAs bulk material. The free exciton of GaAs at 4.2K is located at 1517 meV, which is also the starting point of the current scan. Even though the QWRs and QWs are no longer directly illuminated by the excitation spot, they are still visible. Compared to spectrum (e) however, their intensity is reduced by an order of magnitude. This rest of CEO-related luminescence is attributed to excitonic drift from the excitation region in the AlGaAs bulk material towards the regions of lower energy. Since the detection spot is considerably larger than the excitation spot, this luminescence is still detected.

Ta3c: 2D scan at low excitation power, illuminated from the $[\bar{1}10]$ growth direction

The third sample showing sharp resonances at the overgrown corner is Ta3c. As in figure 6.5, an excitation power of 50 nW is used for the 2D mapping scan. Graph (a) of figure 6.7 shows an overview spectrum of the luminescence at the overgrown corner.

In graph (b) a 2D color map shows the spatial distribution of the logarithm of the PL intensity integrated over the interval from 1538.4 to 1538.6 meV. From the spatial localization as well as from the lineshape and resonance energy, this luminescence is attributed to a CEO quantum dot.

In graph (b) a 2D color map shows the spatial distribution of the logarithm of the PL intensity integrated over the interval from 1554.4 to 1555.5 meV. According to its spatial distribution, the luminescence in this interval most likely originates from localized states within the QWRs.

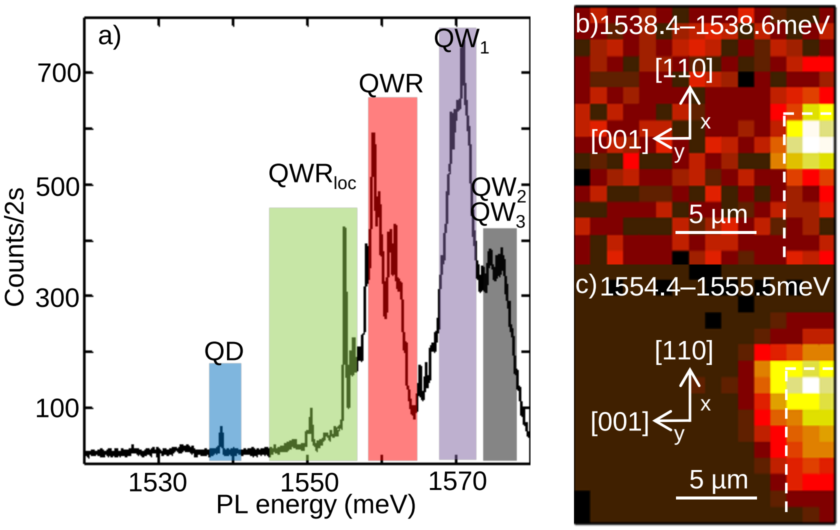

Figure 6.7: (a) PL spectrum of Ta3c recorded at the overgrown corner. All characteristic CEO features observed in the two other samples discussed previously are again visible and highlighted in the spectrum by color bars. (b) 2D plot of color-coded logarithm of the integrated PL intensity in the energy range from 1538.4 meV to 1538.6 meV. Luminescence in this spectral region is localized at the overgrown corner and therefore attributed to a 2fold CEO QD ground state. (c) 2D plot of color-coded logarithm of the integrated PL intensity in the energy range from 1554.5 to 1555.5 meV. Luminescence in this interval is maximal at the corner but extends also along the [110] and [001] directions. As in the previous 2D scans, this characteristic spatial distribution is assigned to localized states within the QWRs. Excitation power is 50 nW, integration time 2s per step.

Ta6: No quantum dot features

None of the samples grown on MBE holder Ta6 during the second and third growth steps show any QD lines. This implies that the growth conditions for successful CEO quantum dot fabrication are very sensitive, since the nominal growth parameters for the growth with Ta3 and Ta6 are identical. The reasons for successful growth or failure are not precisely clear. Only a narrow temperature window in the second and third growth step leads to successful growth, since growth on surfaces of the {110} family is generally much more critical than the standard {001} growth [30]. Differences in the heat capacities of the individual holders as well as inaccuracies in the growth temperature measurements might already be sufficient that two growth steps with nominally identical parameters do not lead to comparable results. Furthermore the cleavage process is an additional uncertainty in the growth procedure. While only samples whose two cleavage steps show no roughness under an optical microscope are processed further, surface roughness that would be fatal for good overgrowth can well be on a smaller length scale than is accessible by this technique.

Linescans on Ta3b along [001] growth direction at low and high excitation power

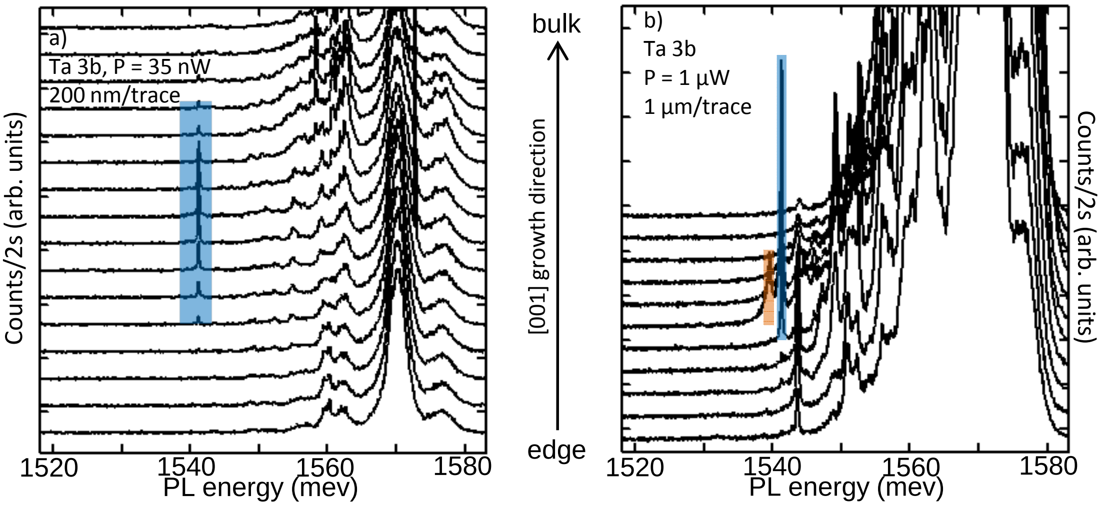

Figure 6.8: (a) Waterfall representation of a linescan along the [001] growth direction at the overgrown corner at low excitation power (35 nW) . The step size is 200 nm per trace. The extent of the QD luminescence (shaded in blue) can be estimated to be in the order of the laser excitation spot diameter, therefore ruling out the possibility that the luminescence originates from several QD pairs. (b) Waterfall representation of a linescan along the [001] growth direction at the overgrown corner at high excitation power (1 μW). For clarity, only one trace per μm is shown. The QD ground state is again shaded in blue. In the middle of the scanning region shown, it is accompanied by a sharp peak $\approx$ 2 meV lower in energy (shaded in orange). Its assignment as the biexciton of the QD ground state is discussed in further detail in the power series in the following subsection.

Graph (a) of figure 6.8 shows a waterfall plot of a linescan at low excitation power (35 nW). Scan direction is in [001] growth direction from vacuum to sample bulk, step size is 200 nm. The QD signal is well visible in 8 traces along the [001] edge. This is in accordance with the good spatial localization of the QD signal on the corner observed in the 2D scan of Ta3b in figure 6.5. The reduced step width of the linescan allows the extent of the luminescence to be determined to 1.6 μm. Since this corresponds to approximately the excitation spot size of the setup it can be concluded that only one single or double QD structure is luminescing in the whole sample. Otherwise the luminescence should be spread out at least 2.2 μm (given by the sum of the excitation spot size of 1.4 μm and the spacing between adjacent QD pairs of 800 nm).

In graph (b) the spectra are recorded at high power (1 μW). For clarity, only one trace every μm is shown. The QD ground state at 1541.1 meV is highlighted in blue and still sticks out as the sharpest and most intense line in the lower energy region. In one trace it is accompanied by a sharp feature $\approx$ 2 meV lower in energy (highlighted in orange). This feature is attributed to be the biexcitonic state of the CEO QD. This assumption is verified in the following subsection by a detailed power series.

Summary on mapping scans

With 1D and 2D mapping scans, PL signals form 2fold CEO nanostructures can be assigned to QWs, QWRs, QWR$_{loc}$ and QDs.

The justification for the assignment of QD lines can be summarized as follows:

- Sharpness of the emission. The FWHM of the emission is found to be limited by the resolution of the detection equipment used (around 180 μeV).
- Spatial localization. The signals appear exclusively at the crossing of three QWs at the overgrown corner of the sample.
- Spectral location. The sharp PL emission is lowered with respect to the QWRs by a localization energy of $\approx$ 21 meV.
- Reproducibility. All three working samples show QD emission lines that can be assigned to two distinct QD energies which are each reproduced in two different samples within a few hundred μeV (see table 6.1).
- Characteristic power dependence. As shown in subsection 6.2.3, the sharp PL signals in the blue-shaded region all exhibit a linear power dependence at low excitation powers, saturation behavior and subsequent decline at higher excitation powers, which is consistent with the interpretation of these lines as coming from zero-dimensional states.

Table 6.1 summarizes the QD energies detected in the three samples analyzed. The repetition of two distinct QD energies within an interval of only ± 200 μeV in different samples is remarkable.

Ta3b	Ta3c	Ta3d
-	1538.5	1538.1
1541.1	-	1541.4

Table 6.1: QD ground state energies in meV, detected in the three working samples Ta3b, Ta3c and Ta3d

Reproducibility of exactly planned QD energy configurations together with atomically precise positioning is the prime motivation for the CEO technique. The ≈ 3 meV between the two distinct QD energy intervals are in the order of magnitude that would be expected for a monolayer fluctuation in one of the three QWs involved. However, the number of examined samples is too small to allow statistically relevant statements. In addition, the multitude of (001) QWs grown introduces a further uncertainty into the measurement. It remains unclear which of the QD pairs are actually luminescing in a given sample.

The localization energy of the QDs $E_{loc,QD}$ is about 21 meV in all samples, which is far more than was observed previously in the only report on successful 2fold CEO in literature [30]. Since the fabrication process used in the present samples differs significantly from the fabrication process used in [30], also leading to different QW energies, the discrepancy is understandable, but in that magnitude still unexpected. The measured localization energy is also larger than expected from numerical calculations [36]. It should be pointed out that an accurate theoretical estimation on the 2fold CEO QD ground state energy is considered to be difficult since confinement energy and coulomb binding energy of the excitons are of the same order of magnitude, making the usual approximations inadequate (see also chapter 5).

Samples grown on identical substrate and under nominally identical growth conditions, but on a different MBE holder show no QD luminescence, emphasizing the fragility of the growth procedure on the cleaved facet.

6.2.3 Power dependence

The power dependence of low dimensional CEO features is discussed at the example of Ta3b.

The linescans in figure 6.8 already give a good overview of the general behavior of the CEO related PL features at low and at high excitation power. Still, a closer-stepped power series is needed to further clarify the presumed origin of some of the resonances, in particular the supposed biexciton signal visible in graph (b) of figure 6.8.

The first experimental evidence for biexcitons in single QDs is described in [38]. In this paper the experimental signature of a two photon absorption process is found to coincide with a characteristic quadratic power dependence of the biexciton line. The quadratic power dependence is therefore used to demonstrate the biexcitonic origin of a specific resonance.

This behavior can be understood by statistical considerations. When higher excitation powers are employed, the probability of multiple excitonic occupation is increased. The probability P(μ) to create a configuration with μ excitons in a QD is given by a Poisson distribution [39]

$$P(\mu) = \frac{N^{\mu} exp(-N)}{\mu!} \tag{6.2}$$

where N is the average exciton number in the QD and corresponds to the excitation power in a PL experiment. Power dependent experiments are therefore mandatory to study multi-excitonic states of QDs.

As can be inferred from equation 6.2 a linear behavior with power is expected for the excitonic ground state, which should saturate and subsequently decline with higher powers. A linear behavior with power is also expected for charged single excitons as well as localized states within the QWRs. For the biexcitonic state, which describes the occupation of the s-shell by two excitons, a quadratic power dependence is expected, with a later onset and saturation behavior as compared to the excitonic ground state. In addition, power dependent measurements help to separate zero-dimensional states from QW and QWR features, since in these higher dimensional nanostructures, no saturation behavior is expected, as they exhibit a continuous density of states.

In figure 6.9 a power series on Ta3b at the overgrown corner is presented. Explored is the power range from 1 nW to 5 μW in 12 steps. In each step, the power is approximately doubled. Graphs (a) to (c) show waterfall representations of the normalized PL intensity as a function of PL energy for the different excitation powers investigated. In graph (a) the interval from 1535 to 1545 meV is shown. The QD ground state, labeled X, it is accompanied by a line at 1539.3 meV, labeled 2X, which quickly gains in intensity relative to the X-line as the power is increased. For the two highest powers measured, both lines are no longer clearly distinguishable from the increased background. Graph (b) shows the spectral range from 1540 meV to 1565 meV. In the center of this interval, localized states of the QWRs are found, which are also discussed in the 2D scans. They are a multitude of broad features with occasional sharp peaks. Graph (c) shows the spectral range from 1550 meV to 1580 meV. The spectral positions of QWR and QW are indicated. This graph shows the non-saturating behavior of the QW and QWR states in contrast to the QD and QWR_{loc} signals.

Graph (d) shows the integrated PL intensity for all groups of lines that are introduced in graphs (a) to (c) in double logarithmic representation. Symbols are measured data, lines are linear fits to the data points. As expected, the QW (blue triangles) and QWR (brown diamonds) intensities increase linearly with excitation power. The linear fits in the double logarithmic representation yield slopes of 1.15 for the QWR and 1.09 for the QW, respectively. Both lines do not saturate in the power range applied. The integrated PL intensity of the 2fold CEO QD ground state, represented by red circles, also increases linearly with power up to 50 nW. The linear fit yields a slope of 1.09. From 100 nW onwards, the QD intensity saturates and starts to decrease, when the excitation power is increased above 300 nW. This behavior further supports the interpretation of the sharp features at low energies in the CEO PL spectra as QD ground states. A behavior similar to the QD line is shown by the localized states within the QWR_{loc}. This group of lines is represented by green triangles in graph (d). Their integrated PL intensity also increases linearly with a slope of 1.18 till 50 nW, then they show a saturation behavior. Above 800 nW, their integrated PL intensity decreases. This power dependent behavior, in particular the saturation together with the sharp and inhomogeneous PL signal clearly shows that these features are not a 1D continuum of states but must originate from

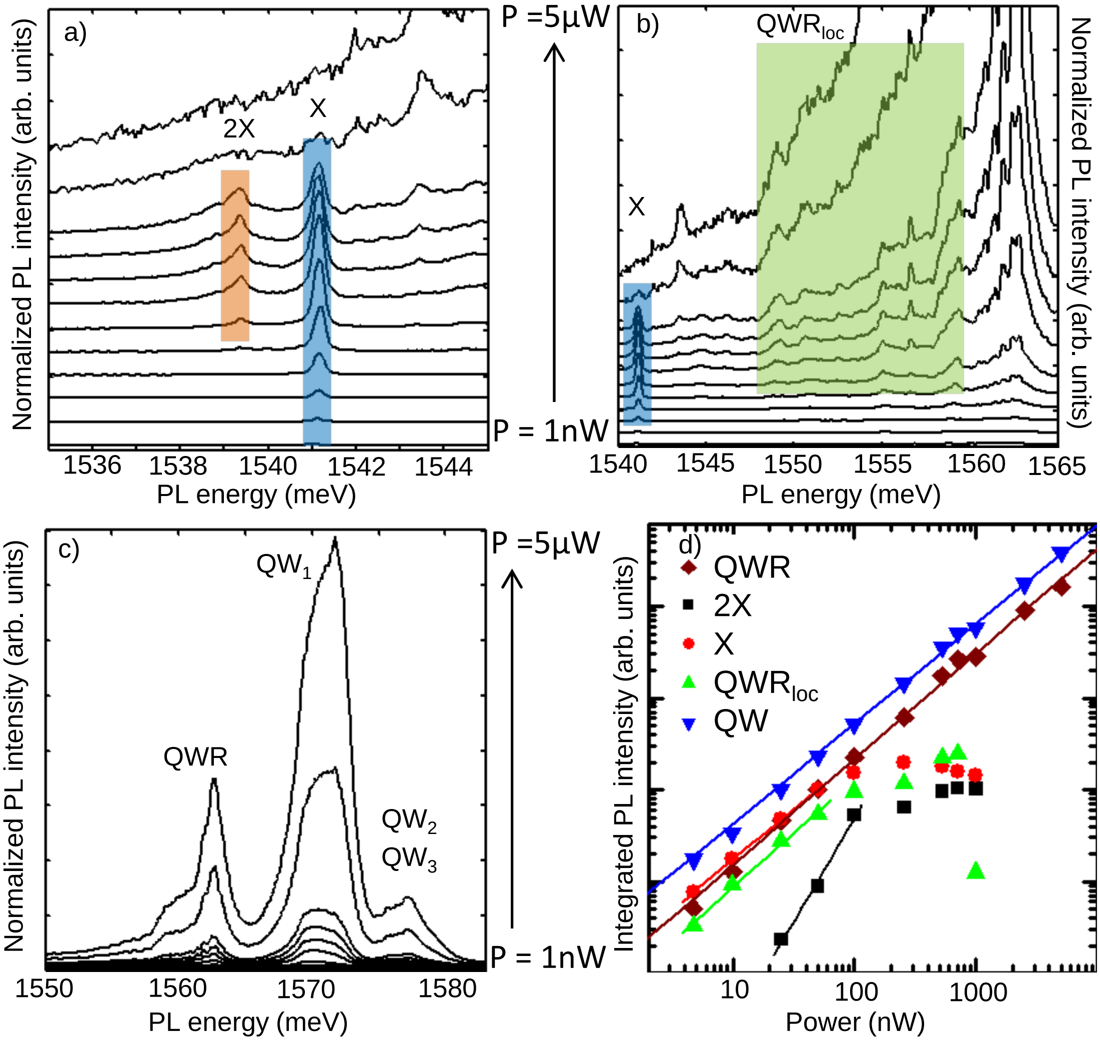

Figure 6.9: Power series on Ta3b at the overgrown corner. The power is varied in 12 steps from 1 nW to 5 μW, each time, the power is approximately doubled. Graphs (a) to (c) show waterfall representations of the normalized PL intensity as a function of PL energy for the different powers investigated. In graph (a) the PL energy range from 1535 to 1545 meV is shown and presumed X and 2X lines are indicated. Graph (b) shows the spectral range from 1540 meV to 1565 meV. The features interpreted as localized states within the QWRs are marked as QWR$_{loc}$. Graph (c) shows the spectral range from 1550 meV to 1580 meV. The spectral positions of QWRs and QWs are pointed out. Graph (d) shown the integrated PL intensity for all groups of lines that are introduced in graphs (a) to (c) in double logarithmic representation. Symbols are measured data, lines are linear fits to the data points. X and 2X features can be clearly identified from their specific slopes and saturation behavior. QWR and QW PL intensities also show the expected linear and non-saturating power-dependence. The localized QWR states QWR$_{loc}$ show a similar power dependence as the excitonic ground state.

zero-dimensional states. The interval these states are observed in is about 15 meV wide. This wide spread suggests that probably different kinds of localized QWR features exist. This might comprise excitonic, biexcitonic and charged states.

The peak at 1539.3 meV, represented by black squares in graph (d) is the only feature showing a stronger than linear power dependence at low powers. It becomes visible above 20 nW excitation power and saturates above 200 nW. The fit to the data points at low powers yields a slope of 2.26. For the following reasons, this peak is attributed to be the biexciton of the QD line at 1541.1 meV:

- quadratic power dependence for low excitation powers;
- appearance as well as saturation are shifted to higher excitation powers as compared to the QD ground state;
- spectral position approximately 2 meV below the QD ground state energy.

6.2.4 Pulsed excitation

For pulsed excitation a pulsed laser diode with $\lambda_{ex} = 654$ nm is used (Picoquant Laser Diode with 50 ps pulse length and 40 MHz repetition rate). The spectra obtained from a pulsed excitation are different from those obtained with a continuous excitation. Figure 6.10 shows a 1D scan along the (001) direction from vacuum to bulk of sample Ta3d. The excitation power used is 2.2 μW, each trace represents a step of 2 μm along the [001] edge. QW and QWR features are on spectrally identical positions as in cw excitation. Localized QWR states are visible around 1550 meV. However, QD ground state luminescence cannot be detected.

Figure 6.11 shows three lifetime measurements performed on structures visible under pulsed excitation with $\lambda_{ex} = 654$ nm. For detection, a fast silicon avalanche photo diode is used that provides a temporal resolution of $\approx$ 100 ps after data deconvolution [45]. The most prominent feature at low energy, the peak at 1552.7 meV which is also visible in the waterfall plot in figure 6.10, exhibits a lifetime of 1.36 ns. An energetically slightly lower feature, also discernible in figure 6.10, has a lifetime of 0.88 ns. This further underpins that these features are indeed localized states within the QWRs and not 1D QWRs themselves, since 1D states are expected to have shorter lifetimes. For the (110) QW, a lifetime of 180 ps is determined.

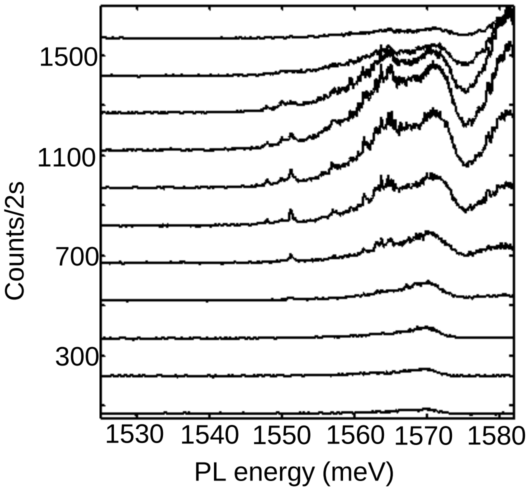

Figure 6.10: Waterfall representation of a 1D linescan along the [001] edge from vacuum to bulk of Ta3d. One trace is shown per 2 microns step width. Excitation power is 2.2 μW. No 2fold CEO QD signals are observed . The spectrally lowest lines are around 1552 meV, visible approximately 8μm along the [001] edge.

6.3 Cleaved Edge Overgrowth field-effect structures

For more sophisticated experiments, a tuning parameter to change the QD properties during experiment is mandatory. A controllable electric field is a standard technique used by many groups today to tune the emission characteristics of self-assembled QDs during experiment [39, 40, 41] via the Quantum Confined Stark Effect (QCSE). In general, an n+ doped back contact and a metal top gate sandwich an intrinsic semiconductor region including a layer of self-assembled QDs. In this way, fields can be applied along the confining direction of the QDs.

The subject of this section is to investigate how these concepts can be applied in the context of 2fold CEO QDs. The section is organized as follows: First the physical effects of electric fields on QWs are introduced. Then the possibility of applying electric fields in the special geometry of 2fold CEO QDs is discussed with the help of simulations. In the experimental part, a simple test structure is presented, followed by characterization measurements. As an outlook, the possibilities of electric field manipulation of 2fold CEO QDs are reassessed.

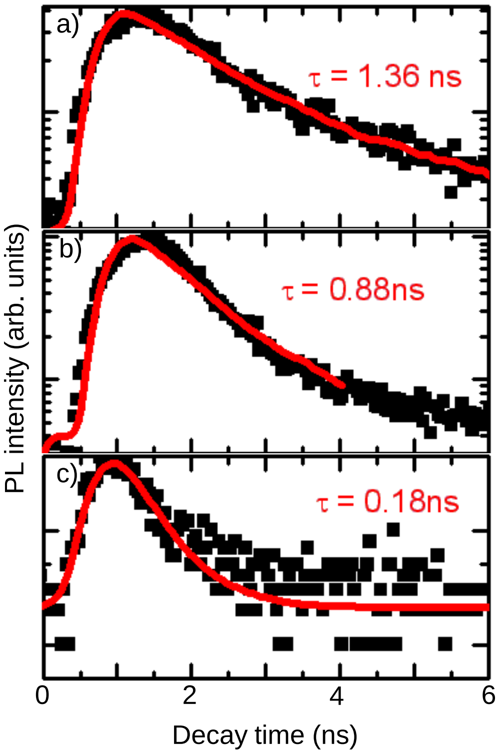

Figure 6.11: Time-resolved data for ((a) and (b)) localized states within the QWRs at 1552.7 meV and 1549.6 meV and (c) the (110) QW (measurement taken at 1579.4 meV). The data points are plotted as black squares, the red curves represent single exponential fits after deconvolution with the instrument response function of the laser.

6.3.1 Quantum Confined Stark Effect in QWs

In a QW, an electric field along the confinement direction shifts the electrons and holes to opposite interfaces. This induced dipole moment results in a redshift of the exciton recombination energy, independent of the sign of the electric field. This effect is called the Quantum Confined Stark Effect (QCSE). Since the exciton has no permanent dipole moment, the red shift depends quadratically on the electric field. The field is first inducing a dipole moment, whose magnitude is proportional to the field strength, then the dipole interaction with the field is again linearly dependent on field strength [35]. An electric field perpendicular to the confinement direction of a QW leads to ionization of the excitons [47].

6.3.2 Electric fields at the crossing of three quantum wells close to two surfaces

Two main aspects have to be considered when the QCSE is to be employed to tune 2fold CEO QDs.

Firstly, a 2fold CEO QD is composed of three perpendicular QWs. Any field applied parallel to the confining direction of one QW will lead to ionization in the other two QWs. A typical field strength where ionization occurs is 10 kV/cm [47]. Care has to be taken to remain well below this value in all spatial directions while manipulating the CEO sample.

Secondly, the 2fold CEO QDs are close to two surfaces.

In figure 6.12 (a), a sketch of a CEO overgrown corner embedded in a field-effect structure is shown. The structure is designed analog to devices used for self-assembled QDs. The growth of this simple field-effect device starts with an n-doped buffer layer of GaAs on an n+ GaAs substrate and is followed by a n-i-p sandwich structure with one 7 nm GaAs quantum well in the middle of a 1μm thick intrinsic AlGaAs layer. Analogous to the samples described earlier in this section, in the second growth step in [110] direction, the structure is overgrown with 7 nm GaAs immediately after an in situ cleavage process. The QW growth is followed by 30 nm $Al_{0.3}Ga_{0.7}As$ and a 300 nm $Al_{0.3}Ga_{0.7}As$/GaAs superlattice. The third growth procedure in [$\bar{1}$10] direction likewise consists of a in situ cleave, a 7 nm GaAs quantum well and a 30 nm $Al_{0.3}Ga_{0.7}As$ framing barrier. All growth steps are terminated by a 10 nm GaAs capping layer. In contrast to the other samples discussed in the previous section, apart from being electrically active, this sample contains just one QD, since in each growth step only one GaAs QW is grown.

In figure 6.12 (b), the influence of the proximity of the surface on the electric field configuration at the site of the QD is illustrated. It shows a 2D simulation with the Poisson solver Femlab that visualizes the electric field at the overgrown corner of the structure shown in (a). It becomes clear that at the position of the quantum well crossing the field is almost equally strong in both spatial directions considered. By applying a compensating voltage in one direction alone, this field cannot be compensated.

This simulation already suggests that with the design presented in figure 6.12 (a) the problem of the ionization of QWs due to built-in fields cannot be solved. However, before suggesting more refined solutions, a test structure as proposed is realized in order to study the particular field configuration of the CEO overgrown corner not only in theory, but also in experiment.

Figure 6.13 shows a typical current-voltage characteristic of the n-i-p structure at room-temperature. It shows rectifying behavior, which is further improved when the sample is cooled down for PL-measurements. In forward direction, the onset for conduction is around 0.6 V. The contact area used in the CEO samples is 3.3 mm^2, which explains the comparatively large leakage currents. Assuming a Schottky barrier of 0.6 V, the static electric field in [001] direction can be approximated by [40]:

$$E = \frac{V_g - 0.6V}{d}, \tag{6.3}$$

with d being the thickness of the intrinsic layer and V_g the gate voltage.

As a first test of the functionality of the field effect structure, the QCSE in the (001) QW should be observable. Likewise, the [001] directed electric field should suppress the PL signal of the QWs of the other two growth directions.

Figure 6.14 shows a voltage scan performed at a fixed spatial position at the overgrown corner of the field-effect CEO sample. Graph (a) shows a waterfall representation of the data, graph (b) a color plot of the applied gate voltage versus PL energy with the PL intensity in color code. The step size in voltage is 0.1 V.

The spectra show only one PL signature. In accordance with the QCSE, the energy

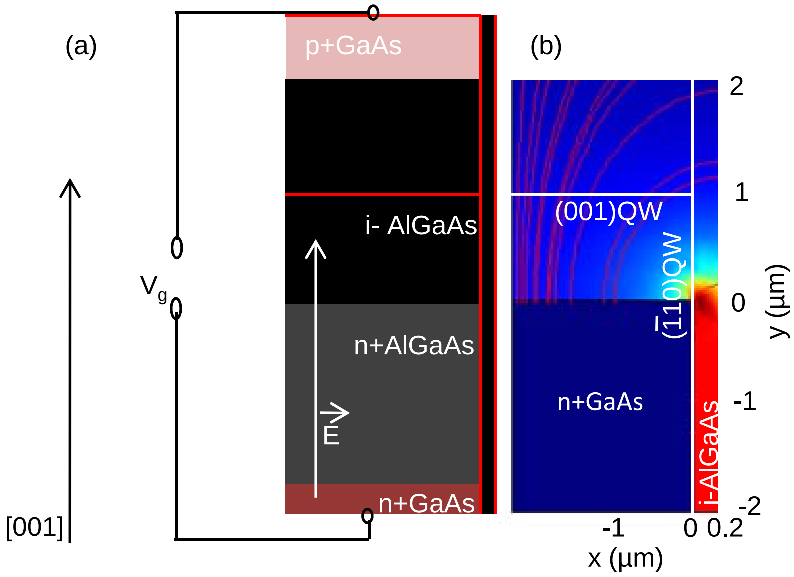

Figure 6.12: (a) Schematic of a CEO sample embedded in a field-effect structure. The [001] growth consists of an n+GaAs layer on top of an n+GaAs substrate wafer (dark red shaded region), followed by 900 nm of n+doped AlGaAs/GaAs superlattices (grey shaded region). The single 7 nm GaAs quantum well (thin red line) is located in a 1000 nm thick intrinsic region of AlGaAs/GaAs superlattices (black shaded region). The structure is terminated by 900 nm of p-doped GaAs (pink shaded region). When a voltage is applied between n- and p-contact, the electric field in [001] growth direction can be tuned. (b) Femlab-simulation of a to-scale 2D model of a CEO edge, when an n+ back contact is used. Color coded is the absolute value of the amplitude of the electric field. The surfaces to the left and to the top are set at the potential of +0.6V with respect to the n+ back contact of the sample. This is approximately the case for GaAs surface states as well as for the p-doped top gate. The white lines mark the (001) and (1-10) QWs, respectively. At the crossing point of the quantum wells, the electric field visualized by red lines does not point straight in (001) direction as is the case in the interior of the sample but is tilted by approximately 45°.

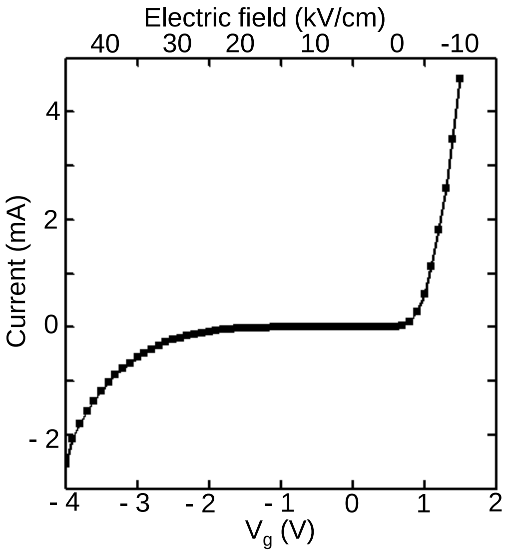

Figure 6.13: Current-voltage characteristic of a CEO field-effect structure at room temperature.

of the PL signature redshifts for any voltage that does not correspond to flat-band conditions $V_g = +0.6$ V of the n-i-p-diode. This together with the energetic position of 1574 meV leads to the conclusion that this PL signature originates from the (001) QW.

Interestingly, the PL signal is suppressed at flat-band conditions. In conventional quantum well field-effect structures with no proximity to surfaces, the PL intensity of the quantum wells is strongest at flat-band-conditions [46]. No signatures of the quantum wells grown in [110] and [$\bar{1}$10] direction are visible.

These observations are consistent with the simulations presented in part (b) of figure 6.12. The built-in field in [001] direction is not the only built-in field present at the CEO sample edge. The suppression of the (001) QW luminescence at flat-band-conditions in [001] direction hints at field components perpendicular to the confinement direction of the quantum well. The fact that the PL suppression is reduced with applied gate voltage might be caused partly by a compensating effect on the other built-in field by applying an external field in [001] direction, partly by increased exciton transfer from the other two QWs into the (001) well. Since the suppression is dependent on the sign of the applied gate voltage, the former effect is probably the dominant one.

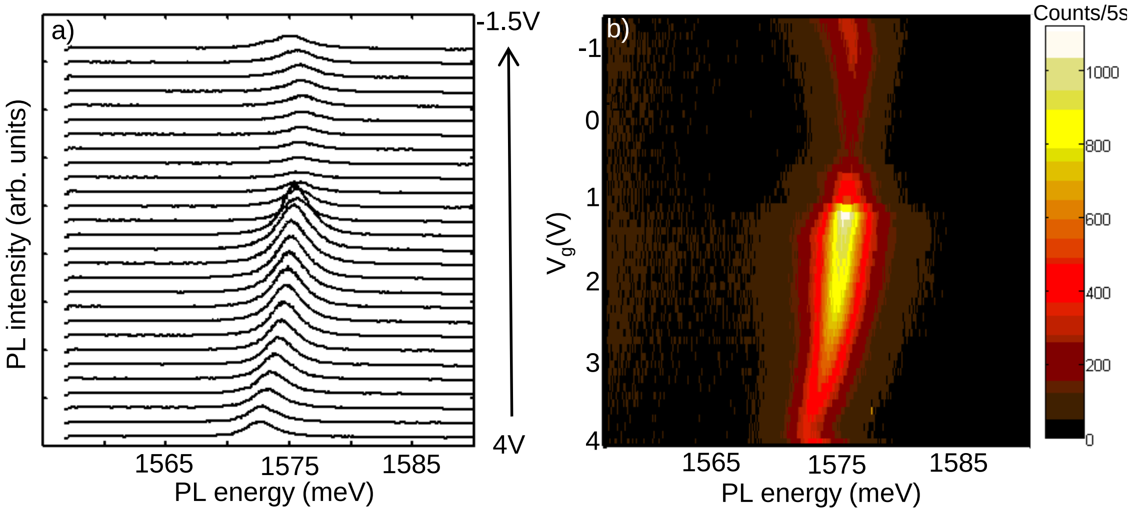

Figure 6.14: Voltage scan in steps of 0.1 V on a p-i-n CEO sample at a fixed spatial position at the overgrown corner. Excitation power is 1 μW, excitation wavelength 790 nm (tunable TiSa laser). (a) Waterfall representation with only every second trace shown for clarity. One PL signal is visible over the whole scanning region. Due to its energetic position and its strong response to the field it is attributed to the single (001) QW. The QW shows a stark shift with the maximum of the PL energy being located around the flat-band conditions of +0.6 V. At the same time, this is the minimum of the PL intensity. For more negative as well as for more positive voltages, the PL intensity increases, while the PL energy shifts continuously to lower energies. The maximal value of the PL energy is observed for a gate voltage of +0.6 V. No signatures of the quantum wells grown in [110] and [$\bar{1}$10] direction are visible. This is attributed to the permanent built-in field in these two growth directions which cannot be compensated by the gate voltage. (b) Color plot representation of the same data.

6.3.3 Summary and Outlook

In order to achieve tunability of 2fold CEO QDs with electric fields, the problem of uncontrollable stray fields due to surface proximity has to be solved. This can be done in two ways. One solution is to increase the layer thickness in the second and third growth steps. Then the strength of the stray fields might be reduced below the ionizing field strength of a few keV/cm. Another solution is illustrated in figure 6.15. By equipping the 2fold CEO structure with a total of three top gates (one at the end of each growth step) a 3D field compensation should in principle be possible. To fabricate gates in [110] and [$\bar{1}$10] growth direction, lithography on the two 150 μm thin cleavage planes is necessary. Alternatively all three growth steps could be terminated by a p-doped top gate. This would be much easier to realize, but might lead to leakage currents in the device.

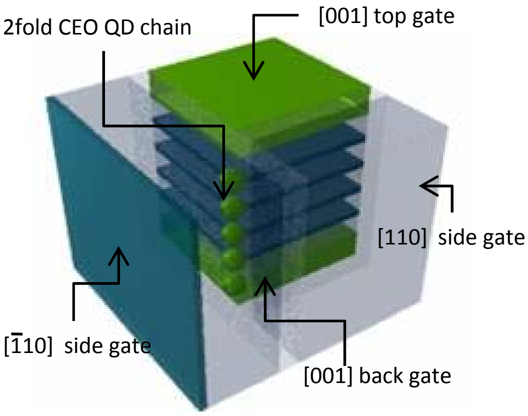

Figure 6.15: Proposal of a CEO-based field-effect structure with three gates. Modified from [48].

A device with such a high level of control could even be used to address individual CEO QDs by a proper interplay of all three gate voltages. Furthermore, it could be employed to measure the transport properties through a chain of 2fold CEO QDs. Considering the complexity of the fabrication process a realization of this device appears to be a larger scale project.

6.4 Summary

CEO nanostructures are identified and studied by 1D and 2D μPL mapping scans and by time-resolved and power-dependent measurements. Distinct excitonic ground states of 2fold CEO QDs with large localization energies are achieved. The deeper localization reached as compared to the only other report on 2fold CEO QDs in literature [29] is attributed to a new strain-free fabrication process and changed QW thickness in [001] growth.

In order to achieve controlled manipulation of 2fold CEO QDs the concept of a CEO structure with three top gates and one back gate is presented. Due to the complexity of this device, a simpler test structure is realized. Measurements on this test structure confirm the necessity to either grow significantly thicker overgrowth layers or to provide separate top gates in all three spatial direction to controllably manipulate 2fold CEO QDs with an external electric field.

Chapter 7

Outlook

The Raman measurements presented in the first part of this thesis are just the starting point of a larger scale project, which aims at thoroughly investigating the structural as well as the electronic properties of semiconductor nanowires with Raman spectroscopy.

Key finding so far is the identification of a Raman signature of wurtzite in single as well as in bundle GaAs nanowires grown under specific growth conditions. Of further interest is the observation of a Raman enhancement effect that might be due to dipole antenna-like resonances of the nanowires with the radiation field of the laser. A promising possibility for further structural improvement is our ability to alter the structural properties during experiment by laser-induced heating.

An immediately planned next step in the Raman nanowire project is to not only control excitation, but also detection polarization. This will allow a clearer assignment of Raman resonances on the basis of selection rules. Furthermore, it gives access to valuable information on the antenna-like resonances in single nanowires.

A very interesting but yet unresolved question is how the band structure behaves in the nanowires composed of alternating zinc blende and wurtzite domains. PL measurements on GaAs nanowires show characteristic transition energies that approximately match the recombination energy of an electron confined in a wurtzite section with a hole confined in a zinc blende region [12]. These questions could be further explored with resonant Raman spectroscopy.

For the Si nanowires, ongoing Raman analysis will be very useful in helping to improve the growth morphology of the new growth process studied. In addition, the annealing procedure that was shown to improve the structural quality of the GaAs nanowires could also be applied to the Si nanowires.

The main result of the second part of the thesis is the fabrication and optical characterization of 2fold CEO QDs whose excitonic ground states exhibit unexpectedly large but reproducible localization energies. By introducing thin wafer growth, the complexity of the CEO fabrication procedure could be significantly reduced in the scope of this thesis. Further simplifications are necessary to make the CEO technique competitive compared to pure self-assembly techniques. Another step in this direction could be the development of an MBE cleavage system which can perform the two CEO steps simultaneously.
Future investigations of CEO nanostructures will concentrate on in-situ tunability of individual structures. We find that the proximity of the 2fold CEO QDs to two surfaces requires an elaborate gating design for field-effect structures. A solution is to equip the 2fold CEO structure with a total of three top gates, one at the end of each growth step. These multi-gated devices could also be used to study transport properties through a chain of precisely engineered QDs.

Bibliography

[1] R. Loudon, *Theory of the first-order Raman effect in crystals*, Proc. Roy. Soc. A**275**, 218 (1963).

[2] R. M. Martin, *Theory of the One-Phonon Resonance Raman Effect*, Phys. Rev. B**4**, 3676 (1971).

[3] R. Loudon *The Raman effect in Crystals*, Advan. Phys. **13**, 423 (1964)

[4] D. Bougeard and G. Abstreiter, *Festkörperspektroskopie*, Vorlesungsskript, Walter Schottky Institut (2008).

[5] C. Colombo, D. Spirkoska, M. Frimmer, G. Abstreiter, and A. Fontcuberta i Morral, *Ga-assisted catalyst-free growth mechanism of GaAs nanowires by molecular beam epitaxy*, Phys. Rev. B**77**, 155326 (2008).

[6] A. Fontcuberta i Morral, C. Colombo, G. Abstreiter, J. Arbiol, and J. R. Morante, *Nucleation mechanism of gallium-assisted molecular beam epitaxy growth of gallium arsenide nanowires*, Appl. Phys. Lett. **92**, 063112 (2008).

[7] S. C. Lee, L. R. Dawson, and S. R. J. Brueck, *GaAs on Si(111)-crystal shape and strain relaxation in nanoscale patterned growth*, Appl. Phys. Lett. **87**, 023101 (2005).

[8] M. Moewe, L. Chuang, S. Crankshaw, C. Chase, and C. Chang-Hasnain, *Atomically sharp catalyst-free wurtzite GaAs/AlGaAs nanoneedles grown on silicon*, Appl. Phys. Lett. **93**, 023116 (2008).

[9] F. Jabeen, V. Grillo, S. Rubini, and F. Martelli, *Self-catalyzed growth of GaAs nanowires on cleaved Si by molecular beam epitaxy*, Nanotechnology **19**, 275711 (2008).

[10] A. Fontcuberta i Morral, D. Spirkoska, J. Arbiol, M. Heigoldt, J. R. Morante, and G. Abstreiter, *Prismatic Quantum Heterostructures Synthesized on Molecular-Beam-Epitaxy GaAs Nanowires*, small **7**, 899 (2008).

[11] F. Glas, J. Harmand, and G. Patriarche, *Why does wurtzite form in nanowires of III-V zinc blende semiconductors*, Phys. Rev. Lett. **99**, 146101.1 (2007).

[12] M. Heigoldt, *Optical Properties of GaAs Nanowire Related Heterostructures*, Diploma thesis, Walter Schottky Institut (2008).

[13] H. Harima, *Properties of GaN and related compounds studied by means of Ramans scattering*, J. Phys. Condens. Matter **14**, R967 (2002).

[14] P. Giannozzi, S. de Gironcoli, P. Pavone, and S. Baroni, *Ab initio calculation of phonon dispersions in semiconductors*, Phys. Rev. B**43**, 7231 (1991).

[15] Rainer Hessmer, *Ramanstreuung an optischen Phononen in GaAs/AlGaAs -Übergittern*, Diplomarbeit, Walter Schottky Institut (1991).

[16] J. Johansson, L. S. Karlsson, C. P. T. Scensson, T. Martensson, B. A. Wacaser, K. Deppert, L. Samuelson, and W. Seifert, *Structural properties of* {111}*B-oriented III-V nanowires*, nature materials **5**, 574 (2006).

[17] J. Jimenez, E. Martin, and A. Torres, *Temperature dependence of the Raman spectrum of* $Al_xGa_{1-x}As$ *ternary alloys*, Phys. Rev. B**58**, 10463 (1998).

[18] P. S. Pizani and C. E. M. Campos, *Strain effects on As and Sb segregates immersed in annealed GaAs and GaSb by Raman spectroscopy*, J. Appl. Phys. **89**, 3631 (2001).

[19] R. L. Farrow, R. K Chang, and S. Mroczkowski, *Detection of excess crystalline As and Sb in III-V oxide interfaces by Raman scattering*, Appl. Phys. Lett. **31**, 768 (1977).

[20] L. Cao, B. Nabet, and J. E. Spanier, *Enhanced Raman Scattering from Individual Semiconductor Nanocones and Nanowires*, Phys. Rev. Lett. **96**, 157402 (2006).

[21] G. Chen, H. Wu, Q. Lu, H. R. Gutierrez, Q. Xiong, M. E. Pellen, J. S. Petko, D. H. Werner, and P. C. Eklund, *Optical Antenna Effect in Semiconducting Nanowires*, Nano Lett. **8**, 1341 (2008).

[22] D. Spirkoska, G. Abstreiter, and A. Fontcuberta i Morral. *Size and environment dependence of surface phonon modes of gallium arsenide nanowires as measured by Raman spectroscopy*, Nanotechnology **19**, 435704 (2008).

[23] A. Fontcuberta i Morral, J. Arbiol, J. D. Prades, A. Cirera, and J. R. Morante, *Synthesis of Silicon Nanowires with Wurtzite Crystalline Structure by Using Standard Chemical Vapor Deposition*, Adv. Mater. **19**, 1347 (2007).

[24] S. Sharma and M. K. Sunkara, *Direct synthesis of single-crystalline silicon nanowires using molten gallium and silane plasma*, Nanotechnology **15**, 130 (2004).

[25] I. Zardo, L. Yu, S. Conesa-Boj, S. Estradé, P. J. Alet, J. Rossler, M. Frimmer, P. Roca i Cabarrocas, F. Peiró, J. Arbiol, J. R. Morante, and A. Fontcuberta i Morral, *Gallium assisted Plasma Enhanced Chemical Vapor Deposition of silicon nanowires*, submitted to J. Appl. Phys.

[26] S. Conesa-Boj et al., *TEM analysis of Si nanowires*, to be published.

[27] H. Richter, Z. P. Wang, and L. Ley, *The one phonon Raman spectrum in microcrystalline silicon*, Solid State Commun. **39**, 625 (1981).

[28] T. Antesberger, C. Jaeger, M. Scholz, and M. Stutzmann, *Structural and electronic properties of ultrathin polycrystalline Si layers on glass prepared by aluminum-induced layer exchange*, Appl. Phys. Lett. **91**, 201909 (2007).

[29] G. Schedelbeck, W. Wegscheider, M. Bichler, and G. Abstreiter, *Coupled Quantum dots fabricated by twofold cleaved edge overgrowth: from artificial atoms to molecules*, Science **279**, 1792 (1997).

[30] G. Schedelbeck, *Optische Eigenschaften von Halbleiternanostrukturen hergestellt durch Überwachsen von Spaltflächen*, PhD thesis, Walter Schottky Institut (1998).

[31] L. Pfeiffer, K. W. West, H. L. Stormer, J. P. Eisenstein, K. W. Baldwin, D. Gershoni, and J. Spector, *Formation of a high quality two-dimensional electron gas on cleaved GaAs*, Appl. Phys. Lett. **56**, 1697 (1990).

[32] E. Uccelli, *Guided self-assembly of InAs quantum dot arrays on (110) surfaces*, PhD thesis, Walter Schottky Institut (2008).

[33] T. Baumbach, P. Mikulik, D. Korytar, P. Pernot, D. Lübbert, L. Helfen, M. Herms, and C. Landsberger, *Advanced X-ray Imaging Techniques for Semiconductor Wafer Characterization*, IEEE (2002).

[34] D. Bimberg, M. Grundmann, and N. N. Ledentsov, *Quantum Dot Heterostructures*, John Wiley & Sons (1999).

[35] M. Grundmann *The Physics of Semiconductors*, Springer, Heidelberg (2006).

[36] M. Grundmann, and D. Bimberg, *Formation of quantum dots in twofold cleaved edge overgrowth*, Phys. Rev. B**55**, 4054 (1997).

[37] J. Hasen, L. N. Pfeiffer, A. Pinczuk, S. He, K. W. West, and B. S. Dennis, *Metamorphosis of a quantum wire into quantum dots*, nature **390**, 54 (1997).

[38] K. Brunner, G. Abstreiter, G. Böhm, G. Tränkle, and G. Weimann, *Sharp-Line Photoluminescence and Two-Photon Absorption of Zero-Dimensional Biexcitons in a GaAs/AlGaAs Structure*, Phys. Rev. Lett. **73**, 1138 (1994).

[39] F. Findeis, *Optical spectroscopy on Single Self-assembled Quantum Dots*, PhD thesis, Walter Schottky Institut (2001).

[40] H. Krenner, *Coherent quantum coupling of excitons in single quantum dots and quantum dot molecules*, PhD thesis, Walter Schottky Institut (2005).

[41] M. Kroner, *Resonant photon-exciton interaction in semiconductor quantum dots*, PhD thesis, Ludwig-Maximilians-Universität München (2008).

[42] F. Hofbauer, *Characterization of Photonic Crystal Microcavities using scanning μ-Luminescence spectroscopy*, Diploma thesis, Walter Schottky Institut (2004).

[43] F. Findeis, A. Zrenner, G. Böhm, and G. Abstreiter, *Optical spectroscopy on a single InGaAs/GaAs quantum dot in the few-exciton limit*, Solid State Commun. **114**, 227 (2000).

[44] J. J. Finley, P. W. Fry, A. D. Ashmore, A. Lemaitre, A. I. Tartakovski, R. Oulton, D. J. Mowbray, M. S. Skolnick, M. Hopkinson, P. D. Buckle, and P. A. Maksym, *Observation of multicharged excitons and biexcitons in a single InGaAs quantum dot*, Phys. Rev. B**63**, 161305 (2001).

[45] M. Kaniber, A. Laucht, A. Neumann, J. M. Villas-Boas, M. Bichler, M.-C. Amann, and J. J. Finley, *Investigation of the nonresonant dot-cavity coupling in two-dimensional photonic crystal nanocavities*, Phys. Rev. B**77** 161303(R) (2008).

[46] E. E. Mendez, G. Bastard, L. L. Chang, and L. Esaki, *Effect of an electric field on the luminescence of GaAs quantum wells*, Phys. Rev. B**26**, 7101 (1982).

[47] A. B. Miller, D. S. Chemla, T. C. Damen, A. C. Gossard, W. Wiegmann, T. H. Wood, and C. A. Burrus, *Electric field dependence of optical absorption near the band gap of quantum-well structures*, Phys. Rev. B**32**, 1043 (1985).

[48] M. Grayson, WSI homepage (2008).

List of publications

C. Rossler, K. D. Hof, S. Manus, S. Ludwig, J. P. Kotthaus, J. Simon, A. Holleitner, D. Schuh, and W. Wegscheider, *Optically induced transport properties of freely suspended semiconductor submicron channels*, Appl. Phys. Lett. **93**, 071107 (2008).

I. Zardo, L. Yu, S. Conesa-Boj, S. Estradé, P. J. Alet, J. Rossler, M. Frimmer, P. Roca i Cabarrocas, F. Peiró, J. Arbiol, J. R. Morante, and A. Fontcuberta i Morral *Gallium assisted Plasma Enhanced Chemical Vapor Deposition of silicon nanowires*, submitted to J. Appl. Phys.

A. Fontcuberta et al. *Bandgap engineering of wurtzite/zinc blende GaAs nanowires*, to be submitted.

I. Zardo et al., *Indium assisted Plasma Enhanced Chemical Vapor Deposition of silicon nanowires*, in preparation.

J. Rossler et al., *Raman spectroscopy studies of wurtzite/zinc blende GaAs nanowires*, in preparation.

Dank

An dieser Stelle möchte ich allen danken, die in den vergangenen Jahren direkt oder indirekt zum Gelingen dieser Arbeit beigetragen haben. Ganz besonders danke ich

Prof. Dr. Gerhard Abstreiter für die Möglichkeit, an einem lebhaften Forschungsinstitut meine Doktorarbeit durchzuführen. Dabei war es für das Gelingen dieser Arbeit ganz wesentlich, dass er seine Erfahrung nicht nur zu wissenschaftspolitischen Zwecken, sondern immer noch auch dafür einsetzt, in schwierigen Situationen gute Richtungen vorzugeben;

Prof. Jonathan Finley für die Aufnahme in seine Untergruppe und das Vermitteln seiner Begeisterung für optische Spektroskopie;

Dr. Anna Fontcuberta i Morral die mich im Austausch gegen das Zusammenstellen eines neuen Raman-Aufbaus an ihrer aktuellen Forschung zu Halbleiternanodrähten teilhaben ließ. Darüberhinaus danke ich ihr für ihre Unterstützung bei der zügigen Fertigstellung dieser Arbeit. Ohne ihren Blick für das Wesentliche und die enge Betreuung trotz örtlicher Distanz wäre das nicht möglich gewesen;

Ilaria Zardo für die gute Zusammenarbeit beim Raman-Nanodrähteprojekt: Zum einen für Ihre Mitarbeit beim Aufbauen des neuen ortsaufgelösten Ramanmessplatzes - wegen des teilweise großen Zeitdruckes war das nicht immer einfach - zum anderen für ihre mit Sorgfalt durchgeführten Raman-Messungen an Si und LBF-GaAs Nanodrähten.

Dance Spirkoska für all ihre Vorarbeit zum Wachstum und zur Charakterisierung der GaAs Nanodrähte und für ihre ständige Hilfsbereitschaft bei allen Fragen rund um dieses Projekt.

den Diplomanden und Doktoranden der Spektroskopiegruppe für viele Diskussionen über messtechnische und physikalische Fragestellungen; insbesondere **Michael Kaniber** und **Arne Laucht** für die Messzeit an dem von ihnen betreuten Nahinfrarot μPL System;

Hubert Riedl für stete Unterstützung bei der Wiederinstandsetzung der alten Geräte in N107S und beim Entwickeln neuer mechano-optischer Konzepte. Nicht zuletzt deswegen war die Laborarbeit für mich immer motivierend;

Max Bichler für das akkurate MBE-Wachstum der Cleaved Edge Overgrowth Quantenpunktproben. Seine exakte Buchführung machte es möglich, auch nach 10 Jahren noch die Wachstumsbedingungen der Vorgängerproben nachzuvollziehen. Danke auch für die geduldige Unterstützung bei den für mich am Anfang schwierigen Schritten der Probenpräparation;

Gert Böhm für das erfolgreiche Wagnis des Wachstums auf dünnen Substratwafern;

Stefan Birner und Jose Villas-Boas für die Unterstützung bei zahlreichen Simulationen zu gekoppelten Cleaved Edge Overgrowth Quantenpunkten, sowie für das Herausarbeiten der theoretischen Probleme bei der Berechnung meiner Stukturen;

Hans Hübl, Olli Dier, Dominik Heiss, Vase Jovanov, Sebastian Strobel, Dr. Dominique Bougeard und Prof. Martin Brandt, die mir bei Fragen zum Wachstum, zu elektrischen Kontakten, zu optischen Komponenten, zur Gerätesteuerung, beim Aufdampfen oder bei speziellen Problemen der Ramanspektroskopie viel geholfen haben und so dazu beitrugen, dass ich grundlegende Experimentierkenntnisse entwickeln und weiterentwickeln konnte;

Ying Xiang, Lucia Steinke, Nebile Isik und Emanuele Uccelli für die kollegiale Gesellschaft im Büro;

meinem Mann **Clemens**, der nicht nur als Forscher immer die richtigen Fragen stellt.